

EFFECTS OF EDDY CURRENTS ON THE TRANSPORT AND FATE OF OIL
SPILLS IN THE STRAIT OF ISTANBUL AND THE GOLDEN HORN

by

Mohammadsadegh Aslani

B.S., Civil Engineering, University of Mohaghegh Ardabili, 2011

Submitted to the Institute for Graduate Studies in
Science and Engineering in partial fulfillment of
the requirements for the degree of
Master of Science

Graduate Program in Civil Engineering
Boğaziçi University

2016

ACKNOWLEDGEMENTS

Firstly, I would like to express my sincere gratitude to my advisor Dr. Emre Otay who provided me the opportunity to step into this field. His immense knowledge, instruction and motivations regarding my academic affairs always have been a great support during my master studies. I am gratefully indebted to his patience, kind personality and his trust me by providing research experiences next to my academic life which all will be a splendid pattern in my future.

My sincere thanks also go to Dr. Emin Özsoy and Dr. Hüsne Altıok for their instructive contributions to move forward this thesis during hardships moments. Meanwhile, I also would like to acknowledge Dr. Nadim Copty and Dr. Osman Börekçi who always have been helpful to provide me with invaluable comments and encouragements during lectures and my graduate study.

I would like to express my great profound to my parents and little sister who have always supported me spiritually with their passionate encouragements, especially my father who always has been a mountain of patience and motivating me for proceeding while encountering difficulties in my life. I also thank my fellows at university and friends who always been modest to be available for sharing their favors, laughs and every moment, specially Hamed Shafiei who has been as a brother to me during last 10 years and Andrea Mueller as an older sister.

Finally, I must state my enormous acknowledgments to my wife, Fereshteh, who has been beside to me from the very beginning of my studies, for her unfailing supports and motivating reasons to keep me going on and stand firmly while facing problems.

ABSTRACT

EFFECTS OF EDDY CURRENTS ON THE TRANSPORT AND FATE OF OIL SPILLS IN THE STRAIT OF ISTANBUL AND THE GOLDEN HORN

Strait of Istanbul is a long narrow channel with high potential of maritime accidents due heavy traffic. The Golden Horn estuary is located at the southern part of the strait can be contaminated in the case of main strait accidents. The long-lasting oil spills in the closed and calm circulating currents increase the environmental impacts. In order to model the fate of oil spill events at Golden Horn, the complex hydrodynamics of strait domain is numerically modeled by Environmental Fluid Dynamic Code (EPA). Simulation attains comprehensive information of oil spills in accordance to short term hydrodynamic conditions such as two-layer flow, lower layer and upper layer blockage conditions. The measured ADCP and CTD data are used as the boundary condition and validating data in the model. The historical ship accident scenarios are used to simulate the transport of oil spill in the main strait and Golden Horn. The model results present the comprehensive time-varying concentration of contamination for the different hydrodynamic structures of the strait of Istanbul and Golden Horn junction. Hence, according to hydrodynamic parameters preliminary or instantaneous actions can be managed in the case of accident maritime accident to reduce the environmental impacts at the strait.

TABLE OF CONTENTS

ACKNOWLEDGEMENTS	iv
ABSTRACT	v
LIST OF FIGURES	ix
LIST OF TABLES	xv
LIST OF SYMBOLS	xvii
LIST OF ACRONYMS/ABBREVIATIONS	xx
1. INTRODUCTION	1
1.1. Problem Definition and Objectives	1
1.2. Site Description	4
2. LITERATURE REVIEW	6
2.1. Past Measurement Used in the Present Study	6
2.2. Oil Contamination in the Strait of Istanbul and the Golden Horn	8
2.2.1. Maritime Traffic Risk in the Strait of Istanbul.	9
2.2.2. Past Oil Spills in the Strait of Istanbul.	10
2.3. Definitions	11
2.3.1. Practical Salinity Scale (PSS)	11
2.3.2. Hydraulic Controls	14
3. FIELD MEASUREMENTS	15
3.1. Position	16
3.2. Water Velocity	16
3.3. Salinity and Temperature	18
3.4. Water Level	19
4. HYDRODYNAMIC MODELING	21
4.1. Hydrodynamics	21
4.1.1. Governing Equations	21
4.1.2. Turbulence Modeling	24
4.1.2.1. Turbulence modeling in horizontal plane	24
4.1.2.2. Turbulence modeling in vertical direction	25
4.2. Bathymetric Gridding	27

4.3.	Boundary Conditions	30
4.4.	Model Input Parameters	32
4.4.1.	Initial Condition	32
4.4.2.	Timing	32
4.4.3.	Hydrodynamic Parameters	33
5.	HYDRODYNAMIC MODEL RESULTS	35
5.1.	Boundary Input Profiles	38
5.1.1.	Two-layer Flow Scenario, Test Run A	38
5.1.2.	ULB Scenario, Test Run B	40
5.1.3.	LLB Scenario, Test Run C	41
5.2.	Validation of Model Results with Measurement (Test Runs A,B,C)	43
5.2.1.	Water Level Difference	44
5.2.2.	Vertical Profiles of Salinity, Temperature, and Velocity at Multiple Cross-sections Along the Strait	48
5.3.	Presentation of Model Results	52
5.3.1.	Vertical Distribution of Salinity, Temperature, Density and Velocity Along the Thalweg	52
5.3.2.	Horizontal Distribution of Surface Velocities Along the Strait of Istanbul	56
5.4.	Hydrodynamics of the Junction of Golden Horn	59
5.4.1.	Horizontal Velocity Distribution of Surface, Interface and Bottom Layers at Junction of Golden Horn	59
5.4.2.	Flow Dynamics of the Junction of Golden Horn	63
6.	CONTAMINATION TRANSPORT MODELING AND RESULTS	68
6.1.	Contaminant Transport Theory	68
6.1.1.	Governing Equation	68
6.1.2.	Initial Condition and Transient Forcing	69
6.2.	Oil Spill Scenarios	69
6.3.	Results	70
6.3.1.	Oil Spill Scenario (I)	73
6.3.2.	Oil Spill Scenario (II)	76

6.3.3. Oil Spill Scenario (III)	77
6.3.4. Oil Spill Scenario (IV)	78
6.3.5. Oil Spill Scenario (V)	80
7. CONCLUSION	82
REFERENCES	85
APPENDIX A: MODEL DESCRIPTION TABLE	89
APPENDIX B: FIGURES OF TEST RUN BU	91
APPENDIX C: FIGURES AND TABLES OF TEST RUN A,B,C	94
C.1. Stations	94
C.2. Comparison Plots	97
C.3. Salinity, Temperature and Density Plots	100
C.4. Velocity Plots	104
C.5. Bed Shear Stress Plots	106
C.6. Densimetric Froude Number	107
APPENDIX D: OIL SPILL PLOTS	108
D.1. Plots of Scenario(I), Test Runs A,D,E,N,Q and Z	108
D.2. Plots of Scenario(II), Test Runs C, R and K	114
D.3. Plots of Scenario(IV), Test Runs B and M	117
D.4. Plots of Scenario(V), Test Runs	119

LIST OF FIGURES

Figure 1.1.	Grid map and cell distribution of the SOI domain.	3
Figure 1.2.	Location map of the Strait of Istanbul and Golden Horn estuary.	5
Figure 2.1.	Risk map for the SOI (collision and ramming).	10
Figure 2.2.	Gotia accident concentration map.	11
Figure 2.3.	Sketch of the SOI internal hydraulics.	14
Figure 3.1.	BU ADCP measurement.	16
Figure 3.2.	Measured flow profile at the North boundary used as input value for Test Run BU.	17
Figure 3.3.	Measured salinity and temperature profiles at the North boundary used as input value for Test Run BU.	17
Figure 3.4.	Measured salinity and temperature profiles at the South boundary used as input value for Test Run BU.	18
Figure 3.5.	Location map of CTD stations for BU measurement.	19
Figure 3.6.	Location of stations for water level measurement.	20
Figure 4.1.	The stretched vertical coordinate system.	22
Figure 4.2.	SOI and GH bathymetric grid.	29

Figure 4.3.	Layer-wise longitudinal-section of thalweg line.	30
Figure 4.4.	Cross-section of the North and South boundaries.	31
Figure 5.1.	Known flow scenarios of the SOI	38
Figure 5.2.	Measured flow profile at the North boundary used as input value for Test Run A.	39
Figure 5.3.	Measured salinity and temperature profiles at the North boundary used as input value for Test Run A.	39
Figure 5.4.	Measured salinity and temperature profiles at the South boundary used as input value for Test Run A.	40
Figure 5.5.	Measured flow profile at the North boundary used as input value for Test Run B.	40
Figure 5.6.	Measured salinity and temperature profiles at the North boundary used as input value for Test Run B.	41
Figure 5.7.	Measured salinity and temperature profiles at the South boundary used as input value for Test Run B.	41
Figure 5.8.	Measured flow profile at the North boundary used as input value for Test Run C.	42
Figure 5.9.	Measured salinity and temperature profiles at the North boundary used as input value for Test Run C.	42

Figure 5.10. Measured salinity and temperature profiles at the South boundary used as input value for Test Run C.	43
Figure 5.11. 3D salinity distribution along the SOI for Test Run C.	44
Figure 5.12. Water level difference distribution along the SOI, Test Runs A,B,C.	45
Figure 5.13. Correlation plot between WLD versus upper and lower layers flows.	46
Figure 5.14. Net flow and WLD correlation plot.	47
Figure 5.15. WLD correlation plot.	48
Figure 5.16. Comparison plots for model versus measured data, Test Run A. . .	49
Figure 5.17. Comparison plots for model versus measured data, Test Run B. . .	50
Figure 5.18. Comparison plots for model versus measured data, Test Run C. . .	52
Figure 5.19. Thalweg line longitudinal-section profiles for Test Run A.	53
Figure 5.20. Thalweg line longitudinal-section velocity profiles for Test Run A.	54
Figure 5.21. Surface water velocity plots for Test Run A.	57
Figure 5.22. Surface water velocity plots for Test Run B.	58
Figure 5.23. Surface water velocity plots for Test Run C.	58
Figure 5.24. Layer-wise velocity vectors at junction of GH for Test Run A. . . .	59

Figure 5.25.	Layer-wise velocity vectors at junction of GH for Test Run B. . . .	60
Figure 5.26.	Layer-wise velocity vectors at junction of GH for Test Run C. . . .	62
Figure 5.27.	Sketch of cross-section used for calculation of the Reynolds No. . . .	63
Figure 5.28.	Surface water Reynolds number versus Q_{Net} plot.	66
Figure 5.29.	Surface water Reynolds number versus WLD plot	67
Figure 6.1.	Accident location map of used oil spill scenarios.	70
Figure 6.2.	Fate of SL.1 accident on Scenario(I), Test Run A.	73
Figure 6.3.	Particles location of SL.1 accident on Scenario(I), Test Run A. . . .	74
Figure 6.4.	Oil concentration of SL.1 accident on Scenario(I), Test Run A. . . .	75
Figure 6.5.	Particle Routes of SL.1 accident on Scenario(II).	76
Figure 6.6.	Particle Routes of Scenario(III).	77
Figure 6.7.	Fate of SL.3 accident on Scenario(IV), Test Run B.	78
Figure 6.8.	Fate of SL.3 accident on Scenario(IV), Test Run M.	79
Figure 6.9.	Fate of SL.1 accident on Scenario(V), Test Run H.	80
Figure B.1.	Thalweg line longitudinal-section profiles for Test Run BU.	91
Figure B.2.	Thalweg line longitudinal-section velocity profiles for Test Run BU. . . .	92

Figure B.3.	Surface water velocity plots for Test Run BU.	93
Figure C.1.	Station locations for model validating test runs.	96
Figure C.2.	Additional comparison plots for Test Run A.	97
Figure C.3.	Additional comparison plots for Test Run B.	98
Figure C.4.	Additional comparison plots for Test Run C.	99
Figure C.5.	Thalweg line longitudinal-section profiles for Test Run C.	101
Figure C.6.	North cross-sectional salinity and temperature profiles, Test Run C.	101
Figure C.7.	Thalweg line longitudinal-section profiles for Test Run B.	103
Figure C.8.	North cross-sectional salinity and temperature profiles, Test Run B.	103
Figure C.9.	Thalweg line longitudinal-section velocity profiles for Test Run C.	104
Figure C.10.	Thalweg line longitudinal-section velocity profiles for Test Run B.	105
Figure C.11.	Bed shear stress distribution over the domain.	106
Figure C.12.	Densimetric Froude number distribution over the domain.	107
Figure D.1.	Fate of SL.2 accident on Scenario(i), Test Run A.	108
Figure D.2.	Particles location of SL.2 accident on Scenario(I), Test Run A . . .	109
Figure D.3.	Concentration of SL.2 accident on Scenario(I), Test Run A.	110

Figure D.4.	Concentration of SL.1 accident on Scenario(I), Test Run D.	111
Figure D.5.	Concentration of SL.1 accident on Scenario(I), Test Run E.	111
Figure D.6.	Concentration of SL.1 accident on Scenario(I), Test Run N.	112
Figure D.7.	Concentration of SL.1 accident on Scenario(I), Test Run Q.	112
Figure D.8.	Concentration of SL.1 accident on Scenario(I), Test Run Z.	113
Figure D.9.	Concentration of SL.1 accident on Scenario(II), Test Run C.	114
Figure D.10.	Particles location of SL.1 accident on Scenario(II), Test Run K.	114
Figure D.11.	Concentration of SL.1 accident on Scenario(II), Test Run K.	115
Figure D.12.	Concentration of SL.2 accident on Scenario(II), Test Run K.	115
Figure D.13.	Concentration of SL.1 accident on Scenario(II), Test Run R.	116
Figure D.14.	Particles location of SL.3 accident on Scenario(V), Test Run M.	117
Figure D.15.	Concentration of SL.3 accident on Scenario(IV), Test Run M.	118
Figure D.16.	Particles location of SL.1 accident on Scenario(V), Test Run H.	119
Figure D.17.	Concentration of SL.1 accident on Scenario(V), Test Run H.	119
Figure D.18.	Fate of SL.2 and SL.3 accident on Scenario(V), Test Run H.	120
Figure D.19.	Concentration of SL.2 accident on Scenario(V), Test Run H.	120

LIST OF TABLES

Table 2.1.	Data source description.	8
Table 3.1.	BU CTD Stations Coordinate	18
Table 4.1.	Turbulence Closure modeling constants.	27
Table 4.2.	Timing table.	33
Table 4.3.	Turbulence eddy viscosity and molecular diffusivity coefficients. . .	34
Table 5.1.	Test runs description table.	37
Table 5.2.	Description of water level differences (WLD).	45
Table 5.3.	Hydrodynamic properties of the SOI and Golden Horn junction. . .	64
Table 6.1.	Table of oil spill scenarios.	71
Table 6.2.	Description table of oil spill.	72
Table 7.1.	Hydrodynamic properties of the SOI and Golden Horn junction. . .	84
Table A.1.	Hydrodynamic modeling description table for the SOI and GH. . .	90
Table C.1.	CTD stations UTM coordinate for Test Run A.	94
Table C.2.	CTD stations UTM coordinate for Test Run B.	94

Table C.3. CTD stations UTM coordinate for Test Run C. 95

LIST OF SYMBOLS

A_H	Horizontal turbulence eddy viscosity, m^2/s
A_q	TKE vertical turbulence eddy viscosity, m^2/s
A_V	Vertical turbulence eddy viscosity, m^2/s
c	Concentration, kg/m^3
C	Conductivity
C_s	Smagorinsky dimensionless coefficient
D_H	Horizontal molecular diffusivity, m^2/s
D_V	Vertical molecular diffusivity, m^2/s
$e_i, i = 1, \dots, 5$	Turbulence closure empirical coefficients
$E_i, i = 1, 2$	TLS empirical coefficients
f	Coriolis force, N
g	Gravity, $9.81m^2/s$
$G_i, i = A, D$	Stability function analogous to Ri
h^*	Bottom elevation
K_r	Reaction coefficient
P	Pressure, N/m^2
$\frac{q^2}{2}$	Turbulence kinetic Energy
Q_c	Sink-source term for contaminant transport equation of TKE
Q_L	Lower layer flow rate
Q_ℓ	Sink-source term for transport equation of TLS equation
Q_q	Sink-source term for transport equation of TKE equation
Q_S	Salinity sink-source term
Q_T	Temperature sink-source term
Q_u	Momentum sink-source term in x-direction
Q_U	Upper layer flow rate
Q_v	Momentum sink-source term in y-direction
r_t	Temperature coefficient of the standard seawater
R	Conductivity ratio

R_T	Ratio of the sample conductivity at temperature T
Ri	Richardson number
S_{Ab}	Absolute Salinity
S_{ij}	Deformation
S_A	Stability function of vertical turbulence eddy viscosity, m^2/s
S_D	Stability function of vertical molecular diffusivity, m^2/s
S_q	Stability function of TKE vertical turbulence eddy viscosity, m^2/s
$SL.1$	Spillage Location at mid-strait for Gotia accident
$SL.2$	Spillage Location at junction of GH for Gotia accident
$SL.3$	Spillage Location at southern entrance for Independenta accident
t	Time, <i>sec</i>
T	Temperature, °C
T_{69}	International practical temperature scale (1968), °C
u	Water velocity in x-direction, m/s
v	Water velocity in y-direction, m/s
\vec{V}	Velocity vector
w	Water velocity in z-direction, m/s
\tilde{W}	Wall proximity function
z	Sigma coordinate system elevation
z^*	Elevation
Δh	Water level difference between North and South ends
$\Delta i, i = x, y, z$	Cell size in i -direction
ζ	Free surface elevation
ρ	Density, kg/m^3
η	Surface water elevation
κ	Von Karman's coefficient
ℓ	Length scale
μ	Dynamic viscosity, $N.s/m^2$
ν	Kinematic viscosity, m^2/s

LIST OF ACRONYMS/ABBREVIATIONS

2D	Two Dimensional
3D	Three Dimensional
ADCP	Acoustic Doppler Current Profiler
BC	Boundary condition
BU	Boğaziçi University Coastal Engineering Lab.
CCW	Counter-clock-wise
CORS	Continues Operating Reference Stations
CTD	Conductivity Temperature Depth
CW	Clock-wise
FDM	Finite Difference Method
GPS	Global Positioning System
IC	Initial Condition
IM-IMSM	Istanbul University, Inst. of Marine Sci. and Management
LLB	Lower Layer Blockage
LPT	Lagrangian Particle Tracking
ppt	Parts Per Thousand
PSS 1978	Practical Salinity Scale 1978
psu	Practical Salinity Unit
RTK	Real Time Kinematic
S.W.	Sea Water
SE	South East
SW	South West
TKE	Turbulence Kinetic Energy
TLS	Turbulence Length Scale
TSS	Turkish Strait System
Two-L	Two Layer Flow
ULB	Upper Layer Blockage
UTM	Universal Transverse Mercator Coordinate System

1. INTRODUCTION

The Strait of Istanbul (SOI) plays, economically and ecologically, a crucial role as a corridor between the Black Sea and the southern seas [1]. The long and narrow geometry with dangerous maneuvers and turbulent eddy currents create risks for ships and the environment especially due to the transport of oil and other contaminants. Temporal and spatial variations in water levels and baroclinic flow conditions of adjacent seas make the currents even more complex.

Just before the southern boundary to the Marmara Sea, the channel branches into a busy estuary, the Golden Horn (GH) estuary located at the crossing of marine traffic and Istanbul's city center. The 3D hydrodynamics of the junction area are numerically modeled for water flow, temperature, salinity and the transport of contaminants in the SOI and the GH. The flow structure of GH is governed by the stratified two-layer flow of the Strait of Istanbul [2]; therefore, whole the domain consisting of SOI and GH is modeled to achieve comprehensive understanding about the strait hydrodynamics.

As mostly the density of oil is less than saline sea water, the contamination will be concentrated on the surface layer. The model results may help to mitigate the risk of oil spill accidents and the fate of contamination on the domain. In this study, the 3D hydrodynamic model introduces in detailed information about the hydrodynamics and oil spill scenarios of GH and SOI.

1.1. Problem Definition and Objectives

The barotropic gradient between the Black Sea and the Marmara Sea induces the flow regime to have the tendency of being flushed towards the southern boundary of SOI. On the contrary, the baroclinic gradient, which allocates the higher saline water in the southern boundary, creates northward flow regime in SOI. As the Black Sea water is fresher than high saline Marmara Sea water, the upper and lower layers are mostly configured southwards and northwards, respectively, unless the blockage events

occurred.

An interface layer is generated at the boundary where two different density waters meet each other. The turbulence and molecular mixing occur in this layer in which modeling of the location and properties of this interface provide a better understanding of SOI hydrodynamic and then in GH.

The body hydrodynamic affects the surface currents which are most critical variable in the occurrence of ship accidents and oil spill release in SOI. Moreover, the spilled oil at main strait can stir towards the GH which is a closed circulation estuary. The transported contamination to this estuary can last for long periods; therefore, in the case of ship collisions, the environmental and economic impacts of this event will be catastrophic.

The analyzed information based on quickly measurable flow parameters such as water level differences and properties of eddy currents can predict the behavior of surface current at the junction of GH and SOI. Under circumstances of any maritime accidents, the emergency response equipment can be established appropriately according to the properties of the oil spill and hydrodynamic conditions to reduce the environmental impacts.

The aim of the present research is to numerically model the stratified flow of the SOI including GH estuary with the 3D EFDC_Explorer program [3]. Then to simulate the fate of oil spill contamination in GH by the prediction of eddy formations induced by different hydrodynamic conditions. This study concentrates on short term events to cover specific hydrodynamic conditions in the case of ship accidents in different locations along the strait. Hence, the oil spill behavior on the SOI and GH can be managed according to the corresponding flow conditions as quick as possible.

The 62.1 km^2 of SOI and GH is covered by $(\Delta_x, \Delta_y) = (50\text{-}200\text{m}, 75\text{-}200\text{m})$ cells to have at least 10 cells in narrowest geometries in Golden Horn and SOI as shown in Figure 1.1.

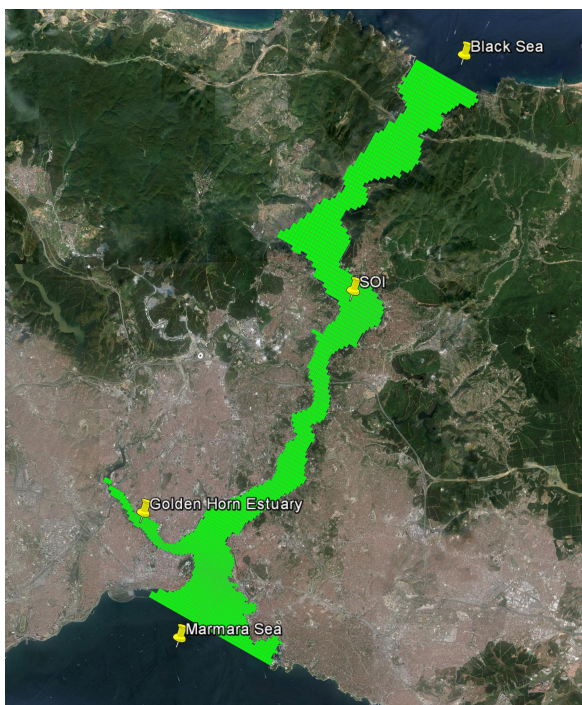


Figure 1.1. Grid map and cell distribution of the SOI domain.

ADCP and CTD measurements survey subjected to this study are conducted for the measuring water velocity, temperature, salinity and water levels at the northern and southern boundaries of the SOI. To cover all possible flow conditions of SOI hydrodynamics such as two-layer flow and upper and lower layer blockages scenarios, field data collected by Özsoy et al. [4, 5], Altıok et al. [6] and unpublished data from Istanbul University, Institute of Marine Science and Management (IU-IMSM, 2009) during different weather and flow conditions are used to validate the model results.

These data were utilized in EFDC Model as boundary conditions, to calibrate model turbulence parameters, velocity distribution over horizontal and vertical planes, stratification profiles, the interface layer and etc.

The salinity, temperature, velocity and water level differences between two ends of SOI are the model validating parameters by comparing to the collected measurement. Furthermore, complex phenomena including turbulent eddy formation, upper and lower

layer blockages [7] are realistically captured by the model and verified against with data.

After finalizing the hydrodynamic test runs, the spillage scenarios based on ship traffic and accident records are used to simulate the transport and fate of oil around the junction of the SOI and the Golden Horn.

The analysis plots are provided to have the quick and overall understanding of the instant flow condition and oil spill behavior without in-depth and time-consuming measurement over the strait.

1.2. Site Description

The SOI as a narrow and long strait which connects the Black Sea in the northern boundary to the Marmara Sea at the southern boundary. The strait has approximately 30 *km* length and 700 *m* at the narrowest width between Bebek coast in European and Kandili coast in Anadolu sides. The irregularly distributed geometry and bathymetry make the strait specific in the case of research. At the southern part of SOI, GH estuary is connected to the main strait which is a closed estuary with no much circulation. The Golden Horn is an estuary with the average width of 293 *m* to 685 *m* having 40 *m* maximum depth at the entrance under the Galata Bridge.

According to the seasonal changes and the governing flow condition of SOI, the GH hydrodynamic structure can follow the stratification of the main strait. Similar to the SOI, the deeper salinity value of GH reaches to 38.5 *psu* while the surface water from creeks makes the salinity of surface layer fresher, with 10 *psu* salinity, than the Black Sea surface the water of the main strait [8]. The very low seasonal inflow quantity of Alibey and Kağıthane creeks are 3.1E-6 m^3/s and 3.4E-6 m^3/s [2] which are negligible in comparison to SOI flow magnitudes having approximate annual average rate of 19,000 m^3/s and 9,500 m^3/s upper layer inflow and lower layer outflow from northern boundary, respectively [9].

The dominant wind is northerly winds blowing from May to October which allocated 60% in comparison to SW and SE winter season winds with 20% frequency [10]. The long-lasting winds fluctuate the water levels at both entrances which configure the barotropic structure of stratified SOI.

The huge maritime traffic load, flow layer complexity, topographical difficulties, surface eddies in the bays and human error factors make the strait potential to the occurrence of ship accidents which induce oil spills to be spread through the SOI and GH. The slicks are long-lasting due to lack of circulation inside of the GH which is economically and environmentally important estuary.

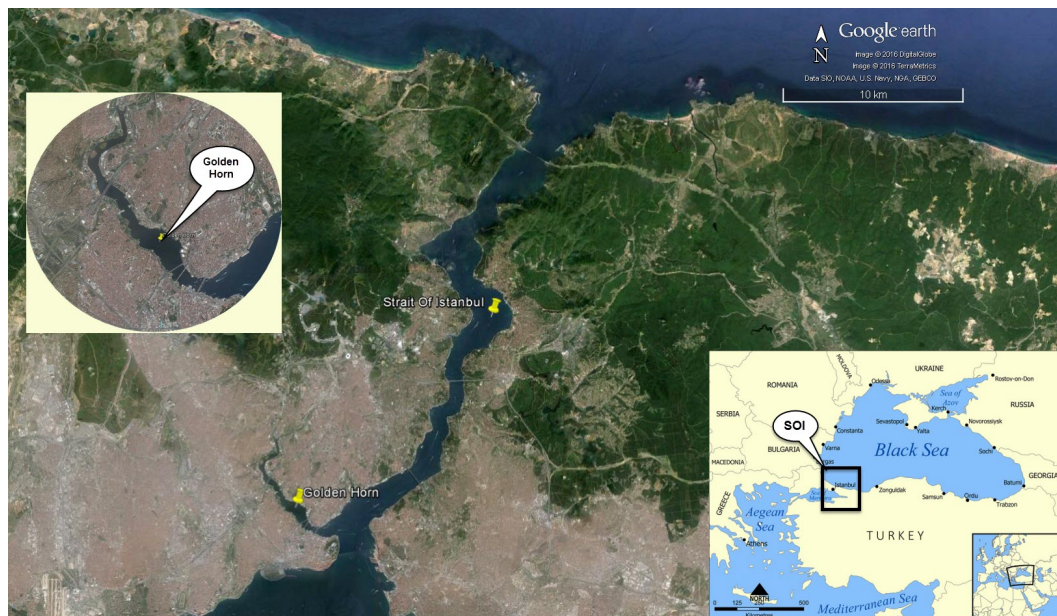


Figure 1.2. Location map of the Strait of Istanbul and Golden Horn estuary.

2. LITERATURE REVIEW

Möller [11] introduced initial measurement of the upper and lower layers flow rate of the stratified Strait of Istanbul. Oğuz et al. [7] stated information regarding the blockage events. Özsoy et al. [4] studied the mixing layer and flow transport between two northern and southern seas through SOI by measurement conducted during 1991-1995 [4]. The latest CTD and ADCP measurement by Altıok et al. [6] and unpublished data from IU-IMSM (2009) provided a comprehensive measurement of the blockage events and Two-layer flow of SOI.

Andersen et al. [12] suggest that the water level at SOI responds to flow structure in the domain according to a linear statistical approach relationship between WLD and upper and lower layers flow rate was studied for 1994-1995 years. Maderich and Konstantinov [13] presented a simplified quasi-steady two-layer model by applying of internal composite Froude number to the measured flow quantities Möller [11] and Özsoy et al. [4]. The model did not take account the salinity and temperature parameters while the stratification and interface layer play a crucial role in defining the flow and mixing structures.

Due to the highly risk of maritime traffic through the strait, Tan and Otay [1] introduced statistical model regarding the risk area for the ship accidents. A simpler depth averaged 2D model by Otay et al. [14] showed that the Golden Horn suffers from a lack of water circulation and long-lasting oil pollution in case of oil spill occurrences [14]. There is lack of studies regarding oil spillage scenarios over the 3D flow modeling by using hydrodynamic and advection-diffusion transport equation so far which is the aim of this study.

2.1. Past Measurement Used in the Present Study

The digitized version of SOI bathymetry by Department of Turkish Navigation, Hydrography and Oceanography (1992) is applied to this study. The thalweg line

surrounding bathymetry is modified to fine bathymetric data in order to achieve more realistic grid.

Altıok et al. [6] introduced the two upper and lower layer blockages, and a two-layer flow scenario measurements. These data will be used for implementation of named regular flow scenarios in this study. Measured CTD data at northern and southern boundaries, and inside the domain provided in detailed information for salinity and temperature profiles in the existence of aforementioned flow conditions. Furthermore, ADCP data are recorded station-wise inside the domain and cross-sectionally at the surrounding of the northern boundary. By these ADCP data, the inflow and outflow rates at boundaries are calculated to be assigned as northern flow boundary input values. In addition, the station-wise inside of the domain velocity records provide the comparison velocity profiles between model and reality.

This data source contains a complete set of demanding EFDC BC parameters such as CTD and the corresponding ADCP measurements. Hence, in order to model the hydrodynamics of SOI for short term periods, this source is used to validate the SOI test runs of this EFDC model for upper layer blockage(ULB), lower layer blockage (LLB) and two-layer flow conditions.

In addition to calibration measurement data sets described in previous paragraphs, some other flow rate measurement data by Özsoy et al. [4, 5], modeled data sets by Sözer [15] and Sannino et al. [16] are used as north flow BC values to provide comprehensive information regarding the behavior of the SOI in the response to many arbitrary flow scenarios.

The water level measurements from Altıok et al. [6], Harita Genel Komutanlığı (HGK, 2016) and modeled values by Bosphorus-ROMS and Bosphorus-TSS models [15,16] provided comparison data with the present model.

In total, the information of used measured or computed CTD/ADCP and water level data in this study are shown in Table 2.1.

Table 2.1. Data source description. (M/ :Measurment by.; C/: Computed by; BU: Otay et al. [14]; IU: IU-IMSM (2009); A: Altıok et al. [6]; Oa: Özsoy et al. [4]; Ob: Özsoy et al. [5]; TSS: Sannino et al. [16]; ROMS:Sözer [15]).

Test Case	Date	Velocity		Salinity & Temperature		Δh $h_{North}-h_{South}$
		<i>North Boudnary</i>	<i>South Boundary</i>	<i>North Boudnary</i>	<i>South Boudnary</i>	
BU	23-Jun-15	M/BU	M/BU	M/BU	M/BU	M/BU
A	17-Feb-09	M/IU	M/A	M/A	M/A	HGK
B	22-Oct-03	M/A	M/A	M/A	M/A	-
C	28-Feb-03	M/A	M/A	M/A	M/A	M/A
D	-	M/Ob	M/Ob	-	-	-
E	-	M/Ob	M/Ob	-	-	-
H	-	M/Ob	M/Ob	-	-	-
K	18-May-92	M/Oa	M/Oa	-	-	-
L	15-May-92	M/Oa	M/Oa	-	-	-
M	02-Sep-92	M/Oa	M/Oa	-	-	-
N	02-Oct-91	M/Oa	M/Oa	-	-	-
P	14-May-92	M/Oa	M/Oa	-	-	-
Q	-	M/Ob	M/Ob	-	-	-
R	-	M/Ob	M/Ob	-	-	-
Z	-	M/Ob	M/Ob	-	-	-
O	generic	C/TSS C/ROMS	C/TSS C/ROMS	C/TSS C/ROMS	C/TSS C/ROMS	C/TSS C/ROMS
U	generic	C/TSS C/ROMS	C/TSS C/ROMS	C/TSS C/ROMS	C/TSS C/ROMS	C/TSS C/ROMS
V	generic	C/TSS	C/TSS	C/TSS	C/TSS	C/TSS
W	generic	C/TSS C/ROMS	C/TSS C/ROMS	C/TSS C/ROMS	C/TSS C/ROMS	C/TSS C/ROMS
X	generic	C/TSS C/ROMS	C/TSS C/ROMS	C/TSS C/ROMS	C/TSS C/ROMS	C/TSS C/ROMS
W	generic	C/TSS C/ROMS	C/TSS C/ROMS	C/TSS C/ROMS	C/TSS C/ROMS	C/TSS C/ROMS

2.2. Oil Contamination in the Strait of Istanbul and the Golden Horn

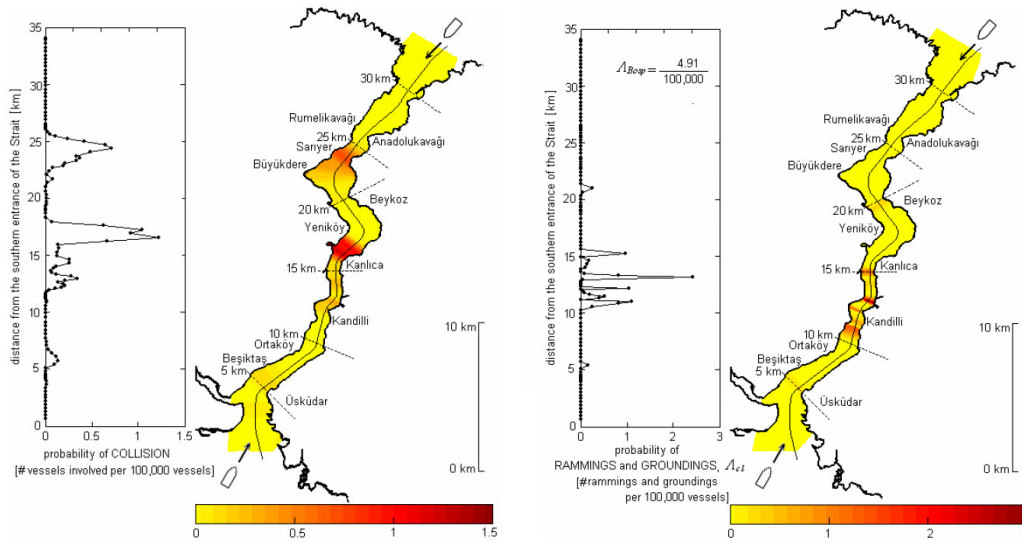
The oil spill is a well-known catastrophic event which has become the important study in the case of reducing the negative effects on human life. By analyzing the interaction of oil spill and hydrodynamic conditions of the domain, the constructive information will be extracted. These information can distinguish the fate of oil spill

under hydrodynamical circumstances which can favor reacting against the spillage as an emergency response plan. The Strait of Istanbul has a complicated and risky geometry which always has been a hazardous strait in the case of an oil spill due to highly marine traffic [1]. SOI is the connecting waterway between the Black Sea and the Marmara Sea which divided Istanbul metropolitan into two sides. Therefore, the highly local maritime traffic and important Cargo ships which carrying petrol or other merchandises increase the disastrous occurrence of the oil spill in the strait.

This study focuses on the oil spill and contamination status of Golden Horn estuary as closed and calm circulation estuary located in the south-eastern part of the SOI. According to the 2D hydrodynamic and oil spill modeling, the GH suffers from pollution by the main strait oil spill accidents due to long lasting oil slicks due to lack of circulation [14]. As the oil density normally is less than sea water surface, and upper layer flow has tangible effects on the direction contaminations towards the GH. Therefore the aim is to model oil spill effects in GH based on the modeled hydrodynamic conditions discussed in Chapter 5.

2.2.1. Maritime Traffic Risk in the Strait of Istanbul.

Daily, 135 vessels travel through the strait which 10% are allocated to hazardous cargos. The geometry of SOI induces vessels to redirect more than 10 times to travel the strait. Additionally, the complicated flow layer structure and variation of current properties such as velocity and directions by the creation of eddy currents encounters the navigation system with the strait a potential accidents events. Figure 2.1 shows the risk zones for the vessel accident through the Strait of the Istanbul [17] which states that the constraints in geometry such as sudden changes and narrow widths increase the accident probability.



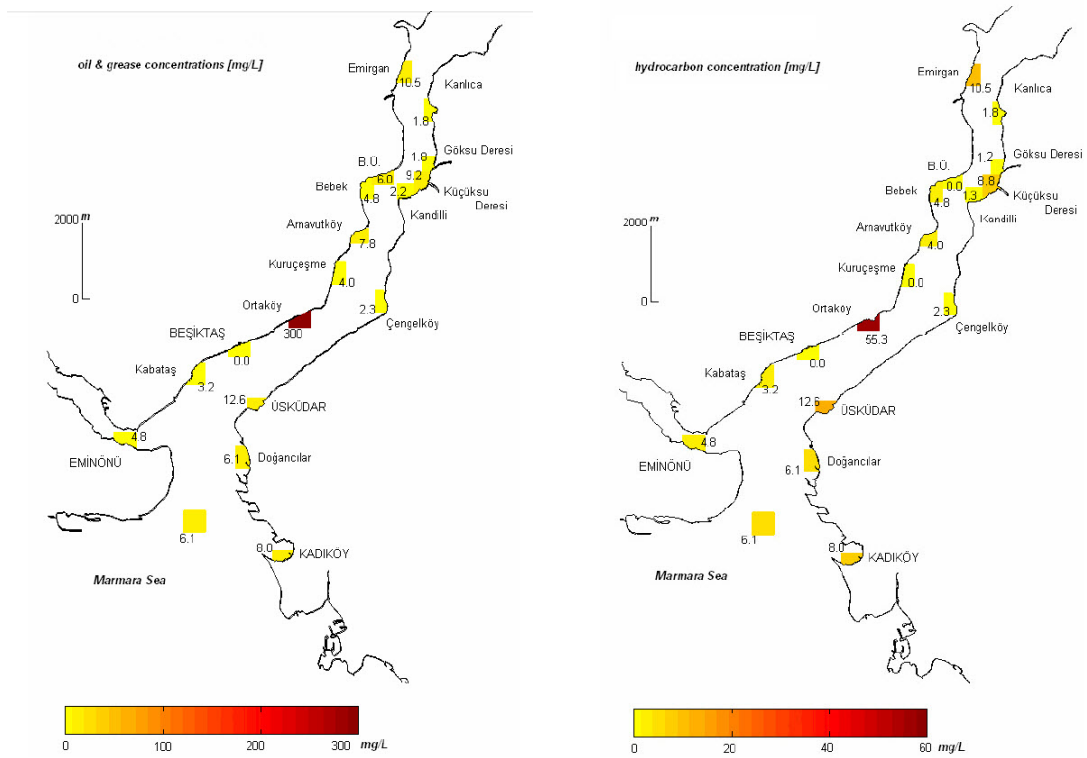
(a) Collision probability.

(b) Ramming probability.

Figure 2.1. Risk map for the SOI (per 100,000 vessels) by Otay and Özkan [18].

2.2.2. Past Oil Spills in the Strait of Istanbul.

According to the Histogram of accidents between 1964 to 2002, as the extreme case of accidents, Independenta heavy oil tanker, contained 94,000 tons, had a collision at the southern boundary of SOI which spilled 64,000 tones and the rest of oil burnt [19]. The accident of Nassia ship occurred at the northern boundary of SOI spilled approximately 13,500 tons of crude oil which led the oil slicks spread through the strait due to the southward upper layer flow. At the middle part of SOI as the riskiest area, the Gotia accident spillage was estimated 18,000 tons which flushed southward by surface current around six hours. According to Figure 2.2, despite this quick travel of oil due to northerly wind, the trapped slicks were found weeks at bays after the accident [20] which specifies the contamination of Golden Horn due to this accidents.



(a) Oil and Grease concentration (mg/L).

(b) Hydrocarbons concentration (mg/L).

Figure 2.2. Concentration map for Gotia ship accident contamination according to sampling in 18 points by Otay and Yenigün [20].

2.3. Definitions

2.3.1. Practical Salinity Scale (PSS)

As a simple definition, salinity is a dimensionless quantity of dissolved salt in grams in one kilogram of seawater presented by Practical Salinity unit (*psu*) or parts per thousand (*ppt*). Due for the small quantity of variability, salinity shall be measured accurately [21]. The Absolute salinity, S_{Ab} , cannot be defined directly; therefore, Practical Salinity Scale 1978 (PSS 1978) is presented as an accurate definition based on the electrical conductivity of seawater at the temperature of 15°C [22] as follow,

$$\begin{aligned}
S &= a_0 + a_1 R_T^{0.5} + a_2 R_T + a_3 R_T^{1.5} + a_4 R_T^2 + a_5 R_T^{2.5} \\
&+ \frac{(T - 15)}{1 + k(T - 1)} \times (b_0 + b_1 R_T^{0.5} + b_2 R_T + b_3 R_T^{1.5} + b_4 R_T^2 + b_5 R_T^{2.5}) \quad (2.1)
\end{aligned}$$

where $k = 0.0162$ and

$$\left\{ \begin{array}{l}
a_0 = +0.0080 \\
a_1 = -0.1692 \\
a_2 = +25.3851 \\
a_3 = +14.0941 \\
a_4 = -7.0261 \\
a_5 = +2.7081 \\
\hline
\sum a_i = 35.0000
\end{array} \right.$$

$$\left\{ \begin{array}{l}
b_0 = +0.0005 \\
b_1 = -0.0056 \\
b_2 = -0.0066 \\
b_3 = -0.0375 \\
b_4 = +0.0636 \\
b_5 = -0.0144 \\
\hline
\sum b_i = 0.0000
\end{array} \right.$$

In order to calculate R_T

$$R = \frac{C(S, T_{68}, p)}{C(S, 15_{68}, p)} \quad (2.2a)$$

$$R_T = \frac{R}{r_T R_p} \quad (2.2b)$$

$$R_p = (1 + \alpha) \quad (2.2c)$$

where, α is an experimental coefficient and r_T are,

$$\alpha = \frac{A_1p + A_2p^2 + A_3p^3}{1 + B_1T + B_2T^2 + B_3R + B_4TR} \quad (2.3)$$

where

$$\left\{ \begin{array}{l} A_1 = +2.070 \times 10^{-5} \\ A_2 = -6.370 \times 10^{-10} \\ A_3 = +3.989 \times 10^{-15} \\ B_1 = +3.426 \times 10^{-2} \\ B_2 = +4.464 \times 10^{-4} \\ B_3 = +4.215 \times 10^{-1} \\ B_4 = -3.107 \times 10^{-3} \end{array} \right.$$

and

$$r_T = c_0 + c_1T + c_2T^2 + c_3T^3 + c_4T^4 \quad (2.4)$$

$$\left\{ \begin{array}{l} c_0 = +6.766097 \times 10^{-1} \\ c_1 = +2.00564 \times 10^{-2} \\ c_2 = +1.104259 \times 10^{-4} \\ c_3 = -6.9698 \times 10^{-7} \\ c_4 = +1.0031 \times 10^{-9} \end{array} \right.$$

Note. This method is valid for salinity and temperature ranges of 2 *psu* to 42 *psu* and -2°C to 35°C, respectively.

2.3.2. Hydraulic Controls

The internal hydraulics by two sills and a contraction in the narrowest width of SOI control several features of the strait flow such as interface layer properties, free surface elevation and etc. The southern sill located at 28 *m* depth in front of Beşiktaş coast and northern sill with 59 *m* depth which lies about 3 *km* far from the northern boundary of SOI [7]. The composite (or Densimetric) Froude number, G^2 , can describe the internal hydraulics criticality of flow system [23],

$$G^2 = F_1^2 + F_2^2 \quad (2.5)$$

$$F_i^2 = \frac{u_i^2}{g'H_i} \quad (i = 1, 2)$$

$$g' = g \frac{\rho_1 - \rho_2}{\rho_1}$$

Where the g' is reduced gravity. According to Figure 2.3, the internal hydraulics are categorized as subcritical ($G^2 < 1$), supercritical ($G^2 > 1$) and critical $G^2 = 1$. In this study's model, the northern sill is outside of domain grid while as the model receives realistic flow, salinity and temperature boundary conditions, the effect of sill is considered in these parameters value.

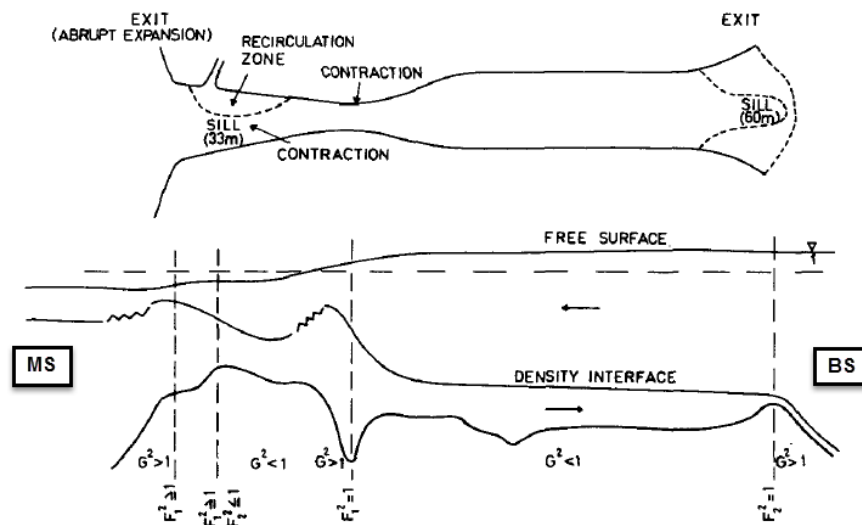


Figure 2.3. Sketch of the SOI internal hydraulics by Oğuz et al. [7].

3. FIELD MEASUREMENTS

In order to achieve short term understanding of hydrodynamics of SOI and GH, it is demanding to model this domain for duration scale of days (e.g. five days). To meet this aim, the initial and boundary conditions shall be defined realistically. The CTD device which is used for conductivity, temperature and depth measurements, and Acoustic Doppler Current Profiler (ADCP) device for current velocity are needed to profile exact salinity, temperature, water velocity over the depth at boundary lines.

Two types of measurement are needed for this model. First, the measurement located adjacent to boundary condition lines and, second, the points inside the domain as comparison points especially the ones settled in specific geometrical conditions. According to section 4.3, the North boundary is a flow boundary which represents the velocity profiles over the cross-sectional area.

In the North boundary between Anadolu Kavagi and Rumeli Feneri coasts, the continuous cross-sectional ADCP measurement is used for this boundary to carry the real flow loads in vertical layers. The CTD measurement in deepest point over the boundary line is appropriate to be set as stratification boundary. In the south boundary of SOI domain, the head boundary needs only salinity and temperature profiles to structure the baroclinic gradient (Section 4.3).

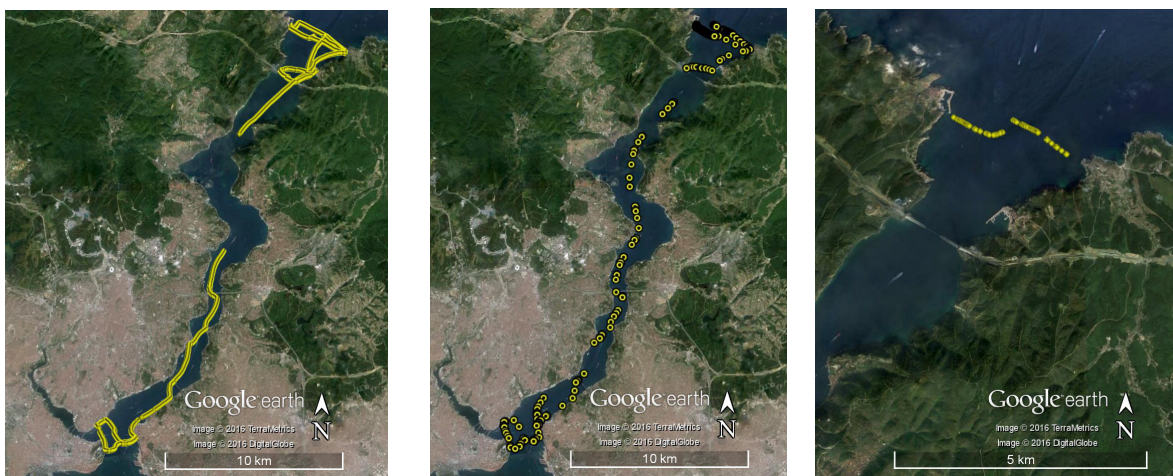
If the SOI hydrodynamic is being studied, the complicated flow scenarios, such as upper and lower layer blockages and two-layer opposite direction flow, should be modeled to attain a comprehensive understanding. A CTD and ADCP survey, targeted to this thesis, is conducted for the model on 23/June/2015 by Boğaziçi University Coastal Engineering Lab (Test Run BU). The survey started from the North boundary of SOI stretched over the SOI domain, ended at the South boundary. 13 number of CTD measurements covered the important locations over the strait. In parallel, the continuous ADCP on northern and southern, in addition to the whole survey moving path, covered the boundary cross-sectional velocity profiles (Table 3.1).

3.1. Position

The CORS survey is positioned by Real-Time Kinematic (RTK) GPS device to track the N&E coordinates of the survey route. The Figure 3.1(a) shows the recorded boat moving route. The survey started at North boundary by setting of station coordinates ($41.206461^{\circ}\text{N}$, $29.130824^{\circ}\text{E}$) and covered the along strait route towards the southern boundary of strait whereas some part of the route is off-recorded.

3.2. Water Velocity

The ADCP device recorded flow data through the moving path from North boundary towards southern boundary according to Figure 3.1(a). Noted that, the stormy northerly wind condition failed the ADCP device to record proper information throughout the survey. In total, 24,000 ADCP points recorded in which around 400 points are survived in whole the domain by data postprocessing, Figure 3.1(b); Almost 60 points are tested in North boundary to be set as BC value, Figure 3.1(c). The geometry of this survey is shown in Figure 3.1.



(a) ADCP route.

(b) Survived ADCP points.

(c) Survived ADCP points at North boundary.

Figure 3.1. BU ADCP measurement.

Measured conductivity and temperature values are converted to Practical Salinity Scale (Section 2.3.1) in 13 stations to feed the North and South BC's and comparison stations data (Table 3.1). In parallel, ADCP data recorded vertical cross-sectional velocity fields during measurement.

According to estimation of these data, $Q_U = 21,000 \text{ m}^3/s$ and $Q_L = -7,000 \text{ m}^3/s$ (Southward is +), salinity and temperature distribution at North and South boundaries are extracted as Figures 3.2, 3.3 and 3.4.

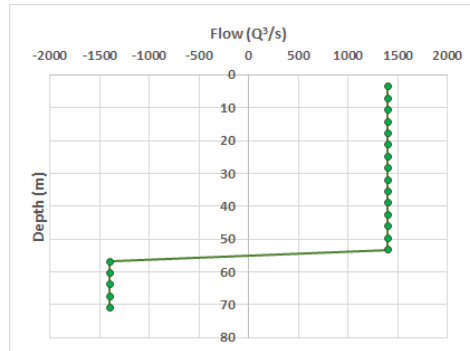


Figure 3.2. Measured flow profile at the North boundary used as input value for Test Run BU.

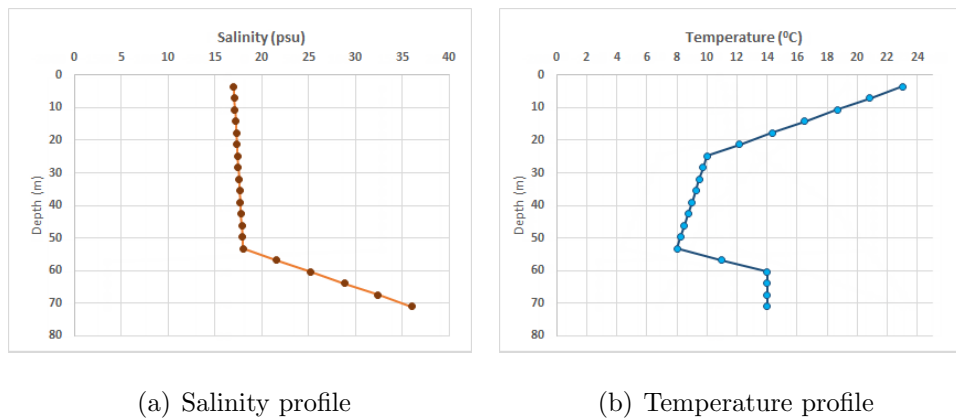


Figure 3.3. Measured salinity and temperature profiles at the North boundary used as input value for Test Run BU.

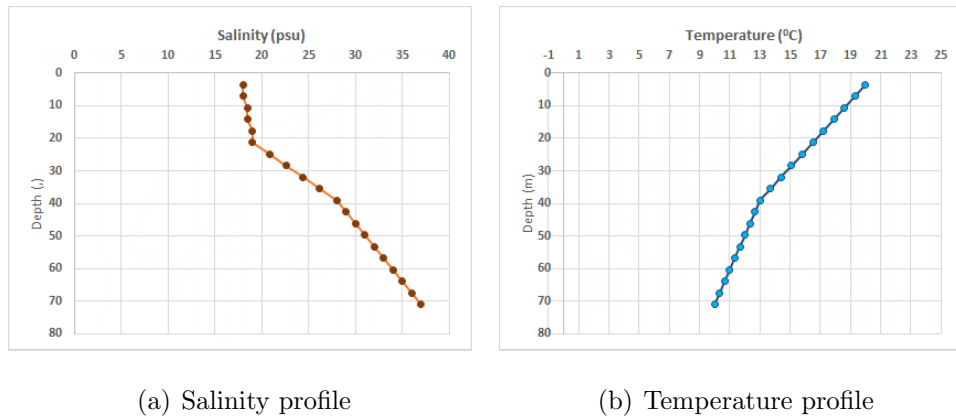


Figure 3.4. Measured salinity and temperature profiles at the South boundary used as input value for Test Run BU.

3.3. Salinity and Temperature

CTD is measured in 13 points including one, six and six at the south, north and inside of the domain, respectively. The CTD measurement UTM coordination and ADCP recorded route are shown in Table 3.1 and Figure 3.5.

Table 3.1. BU CTD measurement coordinates.

Station No	Latitude	Longitude
254	41.22439667	29.13755001
255	41.21942343	29.14585201
256	41.21617054	29.15064266
257	41.23046193	29.11806492
258	41.22815792	29.11491623
259	41.22365967	29.12959203
260	41.21573022	29.15112891
261	41.20294664	29.11168775
262	41.09515933	29.05816710
263	41.04576679	29.03218838
264	41.01519634	28.99540595
265	41.02501418	28.98271413
266	41.02211578	28.99432113

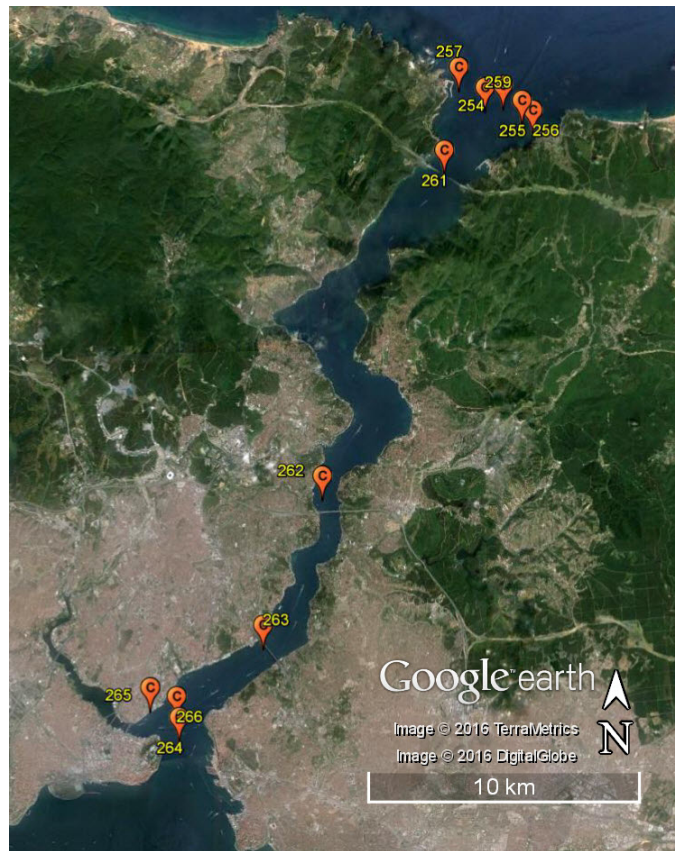


Figure 3.5. Location map of CTD stations for BU measurement.

3.4. Water Level

Water level difference between northern and southern boundaries of SOI was measured manually by rod and leveling device which presented 14 *cm* difference value for 15 minutes measurement interval during six hours. The location of the reference points is presented in Figure 3.6.



Figure 3.6. Location of stations for water level measurement. Northern and southern stations are located at $(41.206461^{\circ}\text{N}, 29.130824^{\circ}\text{E})$ and $(41.018125^{\circ}\text{N}, 29.008641^{\circ}\text{E})$ UTM coordinates, respectively.

4. HYDRODYNAMIC MODELING

EFDC_Explorer V.7.2 is used to model the 3D hydrodynamics of SOI and GH domain. This program is a Microsoft Windows based software interfaced on public domain Environmental Fluid Dynamic Code (EFDC) by the US Environmental Protection Agency (EPA).

4.1. Hydrodynamics

4.1.1. Governing Equations

According to Hamrick [3], EFDC is based on a Finite Difference Method (FDM) which solves 3D equation of motion in horizontal and hydrostatical in vertical directions, incompressible and variable density fluids. The program handles curvilinear and orthogonal in the horizontal plane ($x - y$) and sigma coordinate system in vertical dimension in which the secondary elevation (z) is stretched from free surface elevation and bounded to the bottom elevation of the cell.

Blumberg and Mellor [24] closure turbulence method is used to model vertical turbulent viscosity and molecular diffusivity. The Boussinesq approximation is applied in order to simplify the equations which density neglects the difference in density terms unless they are multiplied by gravity, g .

Conservation of mass, salinity and temperature are the complimentary equations for satisfying the computation process. The overall governing equations are expressed as follow.

In mapping equation, Eq. 4.1, the quantity of z , represents new relative elevation varies between 0 and -1 for the the corresponding bottom ($z^* = -h$) and free surface elevations ($z^* = \zeta$), respectively, in primary physical vertical coordinate system as shown in Figure 4.1.

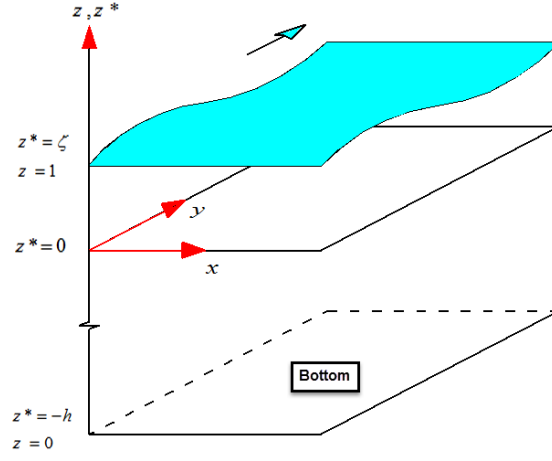


Figure 4.1. The stretched vertical coordinate system.

$$z = \frac{z^* + h}{\zeta + h} \quad (4.1)$$

Conservation of mass for incompressible fluid,

$$\frac{\partial u}{\partial x} + \frac{\partial v}{\partial y} + \frac{\partial w}{\partial z} = 0 \quad (4.2)$$

According to Blumberg and Mellor [24], x-direction equation of motion,

$$\frac{\partial u}{\partial t} + u \frac{\partial u}{\partial x} + v \frac{\partial u}{\partial y} + w \frac{\partial u}{\partial z} - fv = -\frac{1}{\rho_0} \frac{\partial P}{\partial x} + \frac{\partial}{\partial z} (A_V \frac{\partial u}{\partial z}) + Q_u \quad (4.3)$$

where Q_u is x - *direction* momentum sink-source term,

$$Q_u = \frac{\partial}{\partial x} (2A_H \frac{\partial u}{\partial x}) + \frac{\partial}{\partial y} \left(A_H \left(\frac{\partial u}{\partial y} + \frac{\partial v}{\partial x} \right) \right) \quad (4.4)$$

Y-direction equation of motion,

$$\frac{\partial v}{\partial t} + u \frac{\partial v}{\partial x} + v \frac{\partial v}{\partial y} + w \frac{\partial v}{\partial z} + fu = -\frac{1}{\rho_0} \frac{\partial P}{\partial y} + \frac{\partial}{\partial z} (A_V \frac{\partial v}{\partial z}) + Q_v \quad (4.5)$$

where Q_v is y - *direction* momentum sink-source term,

$$Q_v = \frac{\partial}{\partial y} (2A_H \frac{\partial v}{\partial y}) + \frac{\partial}{\partial x} \left(A_H \left(\frac{\partial u}{\partial y} + \frac{\partial v}{\partial x} \right) \right) \quad (4.6)$$

Hydrostatic for vertical direction equation of motion,

$$\rho g = -\frac{\partial P}{\partial z} \quad (4.7)$$

Conservation of salinity equation,

$$\frac{\partial S}{\partial t} + u \frac{\partial S}{\partial x} + v \frac{\partial S}{\partial y} + w \frac{\partial S}{\partial z} = \frac{\partial}{\partial z} (D_V \frac{\partial S}{\partial z}) + Q_S \quad (4.8)$$

where Q_S is salinity sink- source term

$$Q_S = \frac{\partial}{\partial x} (D_H \frac{\partial S}{\partial x}) + \frac{\partial}{\partial y} (D_H \frac{\partial S}{\partial y}) \quad (4.9)$$

Conservation of temperature equation,

$$\frac{\partial T}{\partial t} + u \frac{\partial T}{\partial x} + v \frac{\partial T}{\partial y} + w \frac{\partial T}{\partial z} = \frac{\partial}{\partial z} (D_V \frac{\partial T}{\partial z}) + Q_T \quad (4.10)$$

where Q_T is temperature sink- source term

$$Q_T = \frac{\partial}{\partial x} (D_H \frac{\partial T}{\partial x}) + \frac{\partial}{\partial y} (D_H \frac{\partial T}{\partial y}) \quad (4.11)$$

Equation of state for density calculated based on potential salinity and temperature at atmospheric pressure provided by Fofonoff [25],

$$\rho = \rho(T, S) \quad (4.12)$$

Totally, there are eight unknowns $\vec{V} = (u_x, v_y, w_z)$, p , ρ , ζ , salinity and temperature, which can be solved by eight aforementioned equations, in addition to known turbulent parameters of water and flow.

4.1.2. Turbulence Modeling

Q_u , Q_v , Q_S and Q_T in Eq. 4.4, 4.6, 4.9 and 4.11 are the source or sink terms of momentum, salinity and temperature transport equations. These equations contain horizontal and vertical eddy turbulence eddy viscosity parameters (A_H and A_V) and molecular diffusivity parameters (D_H and D_V) as flow and water properties, respectively.

4.1.2.1. Turbulence modeling in horizontal plane. In horizontal direction, the molecular diffusivity (D_H) acts equal to horizontal turbulence eddy viscosity (A_H) [24]. Smagorinsky [26] sub-grid scale turbulence modeling is used to calculate the turbulence shear stress by eddy viscosity parameter which is presented by deformation, constant coefficient and mesh size in a cell. According to this theory, the sub-grid eddy viscosity (A_H) is,

$$A_{H_{xy}} = (C_s \Delta_x \Delta_y)^2 \sqrt{2S_{xy}S_{xy}} \quad (4.13)$$

where, the deformation of horizontal plane is given by,

$$S_{xy} = \frac{1}{2} \left(\frac{\partial u}{\partial y} - \frac{\partial v}{\partial x} \right) \quad (4.14)$$

by combining these above two equations, the horizontal eddy viscosity calculated by model is

$$A_{Hxy} = (C_s \Delta_x \Delta_y)^2 \sqrt{2 \left(\frac{\partial u}{\partial y} \right)^2 + \left(\frac{\partial v}{\partial x} \right)^2 + \left(\frac{\partial u}{\partial y} - \frac{\partial v}{\partial x} \right)^2} \quad (4.15)$$

4.1.2.2. Turbulence modeling in vertical direction. Mellor and Yamada [27] turbulence closure scheme is used to model the vertical mixing. The method characterizes the turbulence by turbulence kinetic energy (TKE), $\frac{q^2}{2}$, and a turbulence length scale (TLS), ℓ .

Transport equations for TKE and TLS are expressed as,

$$\begin{aligned} \frac{\partial q^2}{\partial t} + u \frac{\partial q^2}{\partial x} + v \frac{\partial q^2}{\partial y} + w \frac{\partial q^2}{\partial z} &= \frac{\partial}{\partial z} (A_q \frac{\partial q^2}{\partial z}) + 2A_V \left(\left(\frac{\partial u}{\partial z} \right)^2 + \left(\frac{\partial v}{\partial z} \right)^2 \right) \\ &+ \frac{2g}{\rho_0} D_V \frac{\partial \rho}{\partial z} - \frac{2q^3}{B_1 \ell} + Q_q \end{aligned} \quad (4.16)$$

$$\begin{aligned} \frac{\partial q^2 \ell}{\partial t} + u \frac{\partial q^2 \ell}{\partial x} + v \frac{\partial q^2 \ell}{\partial y} + w \frac{\partial q^2 \ell}{\partial z} &= \frac{\partial}{\partial z} (A_q \frac{\partial q^2 \ell}{\partial z}) + 2E_1 A_V \left(\left(\frac{\partial u}{\partial z} \right)^2 + \left(\frac{\partial v}{\partial z} \right)^2 \right) \\ &+ \frac{\ell L_1 g}{\rho_0} D_V \frac{\partial \rho}{\partial z} - \frac{q^3}{B_1} \tilde{W} + Q_\ell \end{aligned} \quad (4.17)$$

wall proximity function \tilde{W} is define as,

$$\tilde{W} \equiv 1 + E_2 \left(\frac{\ell}{\kappa L} \right)^2 \quad (4.18)$$

and

$$\frac{1}{L} = \frac{1}{\eta - z} + \frac{1}{H + z} \quad (4.19)$$

Q_q and Q_ℓ are the horizontal mixing terms similar to equation 4.9 and 4.11. To simplify solving of equations 4.16 and 4.17, the vertical eddy viscosity and diffusivity parameters are presented based on analytical stability functions, S_A , S_D and S_q ,

$$A_V = \ell q S_A \quad (4.20a)$$

$$D_V = \ell q S_D \quad (4.20b)$$

$$A_q = \ell q S_q \quad (4.20c)$$

Mellor and Yamada (1982) expressed the Eq. 4.16 and 4.17 in terms of stability functions which are analogous to Richardson number,

$$G_A = \frac{\ell^2}{q^2} \left(\left(\frac{\partial u}{\partial z} \right)^2 + \left(\frac{\partial v}{\partial z} \right)^2 \right)^{0.5} \quad (4.21a)$$

$$G_D = \frac{\ell^2}{q^2} \frac{g}{\rho_0} \frac{\partial \rho}{\partial z} \quad (4.21b)$$

Therefore, the stability functions reduce to,

$$e_2 = S_A (6e_1 G_A) + S_D (1 - 2e_2 e_5 G_D - 12e_1 e_2 G_D) \quad (4.22a)$$

$$e_1 (1 - 3e_3) = S_A (1 + 6e_1^2 G_A - 9e_1 e_2 G_D) - S_D (12e_1^2 G_D + 9e_1 e_2 G_D) \quad (4.22b)$$

$$S_q = 0.20 \quad (4.22c)$$

All of the empirical constant values used in turbulence modeling are shown in Table 4.1 which portrays the EFDC Turbulence Closure Tab.

Table 4.1. Turbulence Closure modeling constants.

Von Karman's Constant	κ	0.4	Turbulence Constant	e_2	1
Min. Turb. Intens. Squared	q^2	1E-08	Turbulence Constant	e_3	0.25
Min. Dim.less Length Scale	ℓ	0.0001	Turbulence Constant	e_4	16.6
Min. $q^2 \times \ell$	-	1E-12	Turbulence Constant	e_5	10.1
Stability Function ($\sim Ri$)	G_A G_D	0.28	Turbulence Constant	E_1	1.8
Turbulence Constant	e_1	1.8	Turbulence Constant	E_2	1.33

4.2. Bathymetric Gridding

EFDC can generate grid cells in the curvilinear or orthogonal system in the horizontal plane. In vertical, the layers are set by dividing each column to the user specified number of layers based on sigma transformation system [28]. The fine gridding properties such as dimension, orientation, and numbers in $x - y$ direction are important in order to generate the appropriate geometry of the case study. This configuration and number of cells in horizontal and vertical dimensions shall be optimized according to fineness of bathymetry data and test run trials in order to favor the modeling process in the case of using large time steps with no hydraulic instabilities.

The SOI is a long and narrow width channel with sharp changes in horizontal and vertical directions. The dimensions of Golden Horn estuary are much smaller than SOI; therefore, the Gridding process must satisfy the necessary properties of both for SOI and GH.

In this model, cell distribution has been defined based on trial and error, considering having at least 10 cells in the narrowest width of SOI and entrance of GH to ease the flow circulation with no difficulties. To apply this, the focal point has been considered at Lat/Lon UTM coordinates of 41.006863°N, 29.003346°E. The 62.1 km^2 of SOI and GH are covered by the initial cell size from focal point which is considered 75 m and the maximum of 200 m with increasing factor of 1.02 for the $x - direction$ and 50 with increasing rates of 1.05 and maximum 200 m in the $y - direction$. Noted that, the

$+x$ and $+y$ vectors represents eastward and southward directions, respectively, with 28-degree clockwise orientation for cell settlements. The available measured data on North and South boundaries are the reason for the mentioned cell rotation to have perpendicular inflow and outflow BC's.

According to measured ADCP data logs in northern flow boundary and having a fine resolution in z -*direction*, 20 number of layers are set to the domain columns. This quantity of layers provided satisfying results for the model in regards to simulation time and desirable accuracy for the comparison into the domain. 3,878 cells in horizontal plane multiplied to 20 layers in vertical direction generates 77,560 cells in total.

EFDC can import ASCII bathymetry data and interpolate in different ways based on the fine or coarse status of the available data. To meet the realistic condition of bottom topography, the model bathymetry is interpolated to nearest depth value to cover all the cells and any sharp depth changes at the bottom. The maximum depth of the interpolated water depth in this model is 108 *m* corresponding the narrowest width of SOI and 39 *m* for the entrance of GH estuary. In addition, the maximum depth of northern and southern boundaries of SOI domain are 71 *m* and 56 *m*, respectively. The model bathymetry and layer-wise thalweg line longitudinal-section are shown in Figures 4.2 and 4.3.

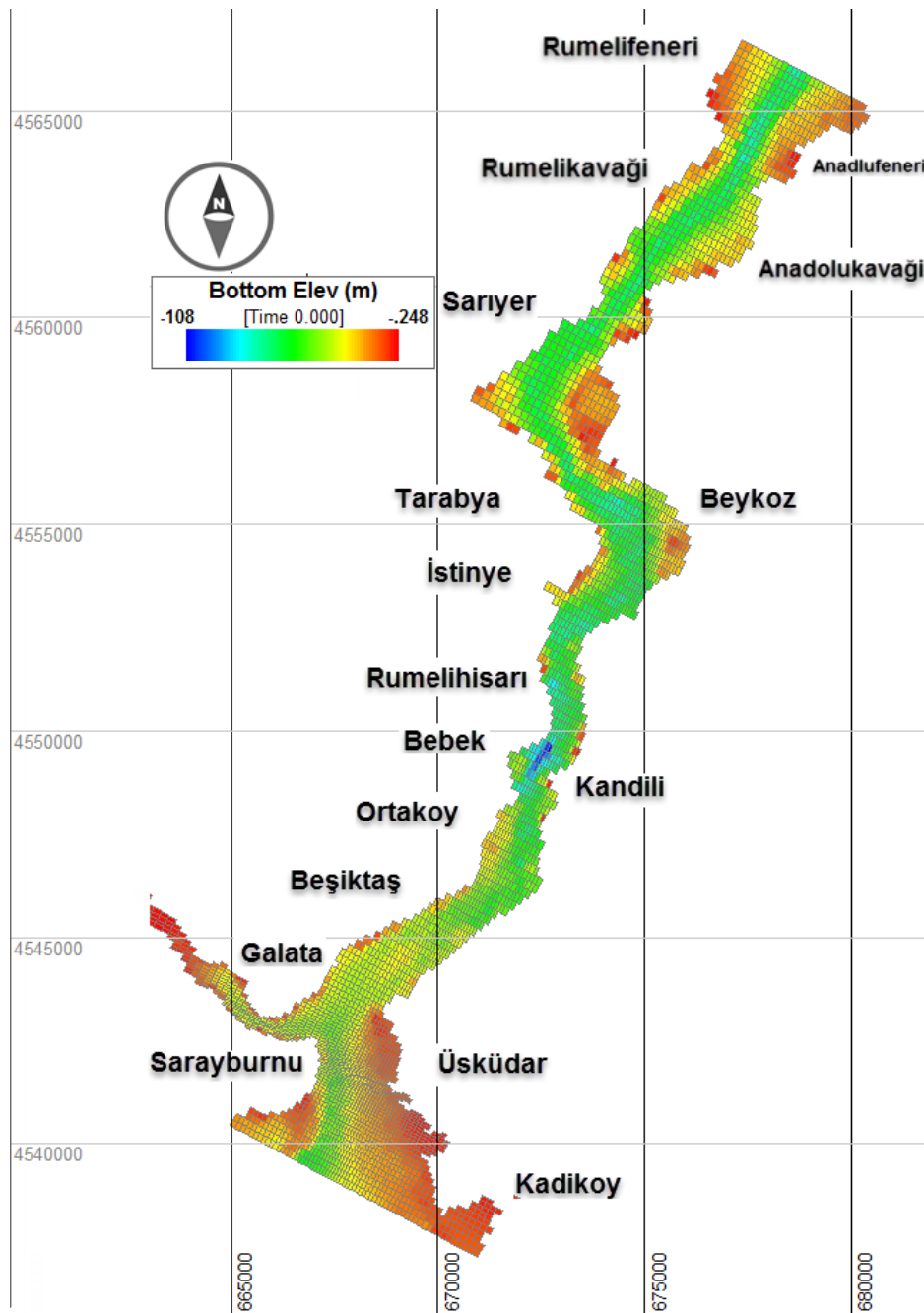


Figure 4.2. SOI and GH bathymetric grid.

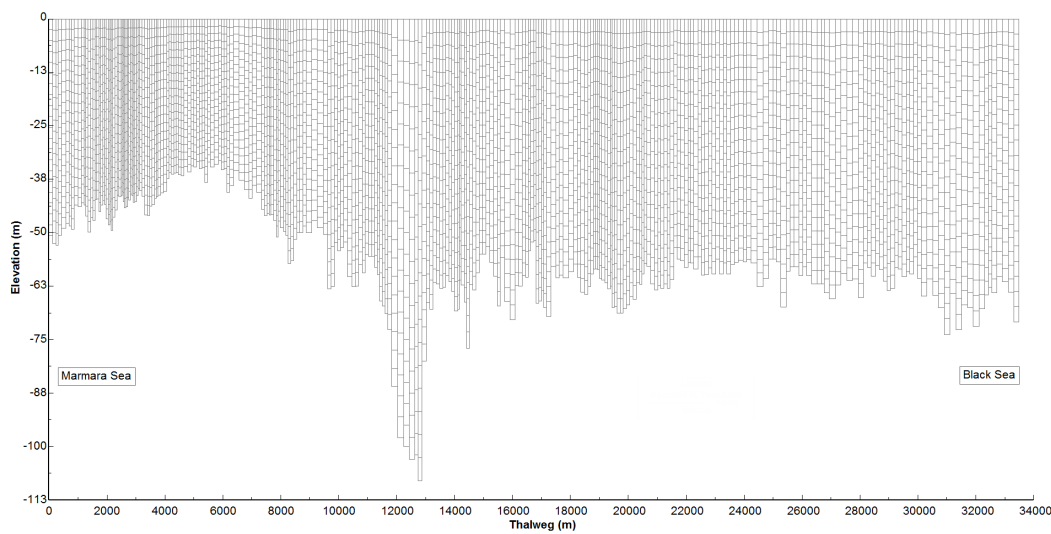


Figure 4.3. Layer-wise longitudinal-section of thalweg line.

4.3. Boundary Conditions

EFDC can solve 3D hydrodynamics of SOI domain by setting of realistic boundary conditions. Several hydrodynamical, meteorological and water quality boundary conditions can be applied to the cell groups in EFDC. In order to achieve realistic short term flow structure, it is important to set the hydrodynamic parameters appropriately. Hence, measured ADCP and CTD data expressed in Section 2.1 are converted to EFDC input format to be used as BC values. Flow and head boundaries, salinity, temperature and the wind are the main effective BC's which are applied to present study's Model.

North boundary consists of 29 horizontal cells and 20 layer in vertical, with depth varies from 12 *m* to 71 *m* (Figure 4.4). Regions near to flow boundary may suffer from hydraulic instabilities which this problem is solved by inputting realistic flow rate values through the vertical layers and choosing flow boundary at the north to be in the far distance to GH estuary as the focus area of this study. In this case, the flow structure and consequence head differences will be established before reaching the GH. For the north flow the boundary in every vertical layer, temperature, and salinity

profile values are extracted from measured CTD data and flow quantities calculated based on cross-sectional continuous ADCP measurement at northern boundary.

In southern boundary, the reference zero head BC in addition to measured CTD data for salinity and temperature have been applied to the boundary line. By this means, water level distribution through the strait will be calculated by the southern reference zero-head boundary. So that, the baroclinic gradient between North and South boundaries is free to behave realistically to reach the stability. Noted that, the water level elevation is flexible to fluctuate according to domain hydraulics. The cell and column distribution of North and South boundary cross-sections are presented in Figure 4.4.

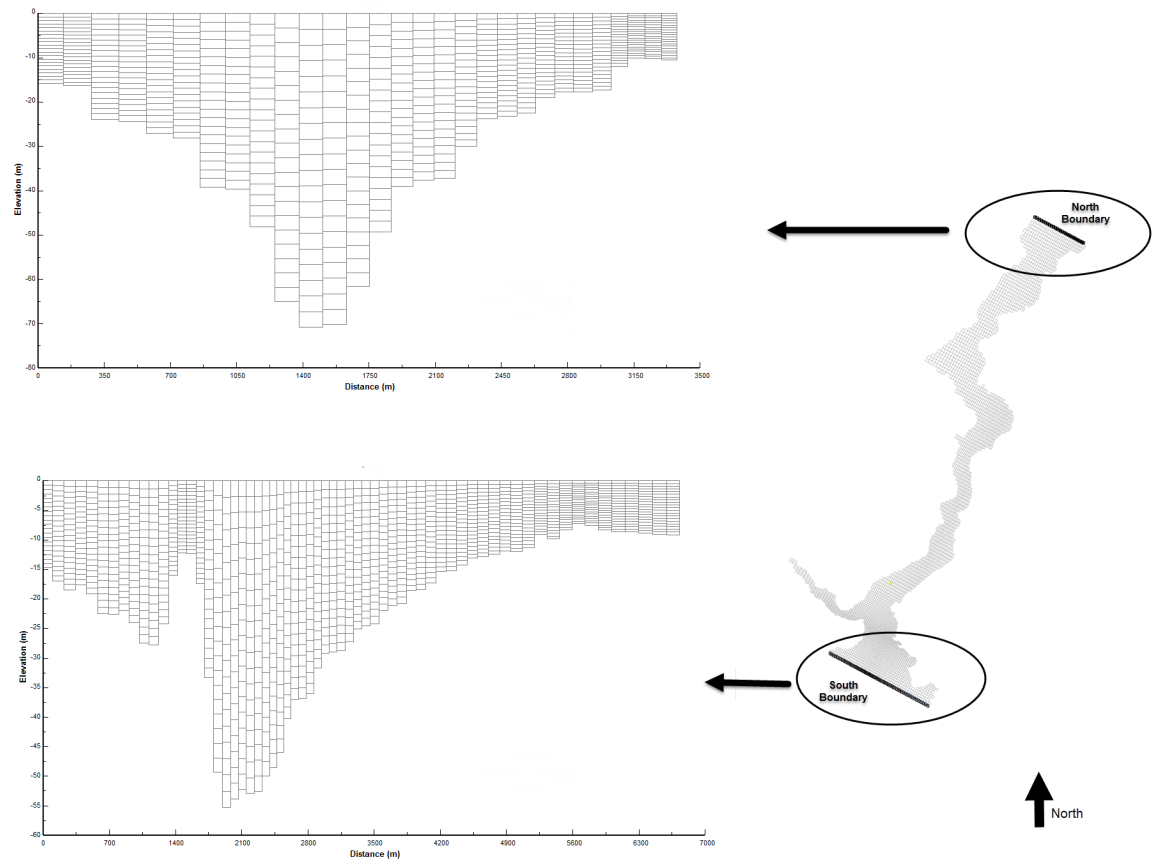


Figure 4.4. Cross-section of the North and South boundaries.

The hydrodynamics of SOI responds to the governing winds on the northern and southern seas [7], so their effects are included in realistic flow, salinity, and temperature boundary profiles. In addition, although the winds on the domain are negligible, in some test runs it is considered to act as a boundary condition.

The tide, evaporation, and precipitation have minor effects on the hydrodynamic structure of SOI [12,29]. Noted that the bottom and wall friction, Coriolis and atmospheric effects are neglected in these test runs.

4.4. Model Input Parameters

4.4.1. Initial Condition

If the Initial values for temperature and salinity would set properly, the can reach the model to stability soon. However, the setting of this condition can induce the model to encounter influencing initial gradients which can influence the real hydrodynamic condition. Therefore, in order to solve this problem, applying no initial condition for salinity and temperature is considered for this model to let parameters be distributed due to baroclinic and barotropic gradients with no external forces. Instead, the first two days of the runtime are considered as stabilization of flow. In spite of the fact that this can increase the test run time, this is the proper solution in case o stabilizing the model properly. In this model's test runs the hydraulic structure reach the stability in the second day of the run.

4.4.2. Timing

The model runtime must cover the needed time for reaching the hydraulic consistency of the model. The test runs stabilize in the second day normally. Therefore, considering almost 30,000 *m* length of the domain, a surface water particle needs almost three days to travel the whole domain with the minimum speed of 10 *cm/s*. Hence, minimum total time of five days is considered as the proper duration for test runs.

The computational time step is sensitive to the defined gridding and boundary conditions. This value changes from test to test according to the complexity of the flow structure such as the upper and lower layer blockages and two-layer flow conditions as shown in Table 4.2.

The test runs have been launched in 64-bit Windows PC, Intel® Core™ i7-3770S CPU @ 3.10 GHz Processor, 8.00 GB RAM. EFDC_Explorer v7.2 is applicable in 32-bit operational a system which the CPU runtime differs based on time step and flow conditions as shown in Table 4.2.

Table 4.2. Timing table.

Flow Condition	Computational Time Step	Model Runtime	CPU Runtime
	<i>sec</i>	<i>day</i>	<i>hour</i>
Two-layer Flow	0.5 - 1	5	4.5 - 9
LLB	0.5	5	4.5
ULB	0.5 - 1	5	4.5 - 9

4.4.3. Hydrodynamic Parameters

The discussed hydrodynamic such as turbulence viscosity and molecular diffusivity coefficients in Section 4.1.2 are effective calibrating parameters to configure the stratification, mixing layer properties and velocity vector fields. In the horizontal plane, it is tested that applying the Smagorinsky turbulence dimensionless constant (C_S) affects the occurrence of blockages or two-layer events. Furthermore, setting this value as *zero* or larger than *zero* induces model to use constant or real-time calculating horizontal turbulence eddy viscosity (A_H) in model [30]. Noted that, according to Section 4.1.2.1, the horizontal turbulence eddy viscosity, and molecular diffusivity values are considered equal in the horizontal plane.

In the vertical direction, vertical turbulence eddy viscosity (A_V) and vertical molecular diffusivity (D_V) parameters are defined according to literature and trial and error to distinguish calibrating values. Similar to the horizontal plane, the user can define the vertical turbulent eddy viscosity or molecular diffusivity values as constant or calculating status. The used values which archived the best-fitting result between measurements and model for upper and lower layer blockages and two-layer flow are tabulated in Table 4.3.

Table 4.3. Turbulence eddy viscosity and molecular diffusivity coefficients.

Flow Condition	A_H	C_S	A_V	D_V
	m^2/s		m^2/s	m^2/s
Two-layer	0.01	1	1E-05	1E-06
ULB	0.01	1	1E-06	1E-08
LLB	0.01	0	1E-08	1E-06

5. HYDRODYNAMIC MODEL RESULTS

Regarding the Test Run BU (Otay et al. [14]) which is implemented based on present study measurement; the fresher Black Sea water has salinity value around 16.5 to 18.5 *psu* compared to 38.5 *psu* maximum salinity of Marmara Sea [7]. The found 36 *psu* salinity at lower layers of the North boundary by CTD is a prove of the existence of Marmara Sea layer water in the domain. Therefore, after modeling with these BC values, it is expected that model structure results in two-layer flow condition. In spite of the signs of the two-layer flow condition by measured CTD data, applying these flow rate and stratification gradients between two ends of the strait model shows fully southward flow with lower layer blockage scenario at SOI.

There are two possible scenarios on this contradiction between model results and CTD measurements; the existence of two-layer flow or the trapped water of Mediterranean Sea in the north of the SOI. The meteorological data collected in Kilyos station show governing northerly wind with a value of 5.5 *m/s* lasting from the previous day. This can be a proof to receive lower layer blockage scenario in the model due to the higher barotropic gradient in Black Sea part. Consequently, the existing saline water at northern lower layer might be explained by the complicated hydrodynamic of SOI considering the effects of described sills in Section 2.3.2 [7]. So as the occurrence of lower layer blockage scenario starts, some Mediterranean saline water can be trapped in northern lower layers. Therefore, in this case, the measured saline water is not a sign of existing northward lower layer flow regime.

The other possibility of the occurrence is due to ADCP recording failure in which the survived ADCP data are not extracted appropriately to define the realistic corresponding flow condition of the strait, as explained in Section 3.2. Consequently, the existence of higher salinity by CTD in lower layers can not be a literal proof of northward lower layer flow in this test run. According Table 5.1, the modeled water level difference value presents only 2 *cm* deviance to the measurement. Considering approximately matched water level difference as an advantage and contradiction be-

tween test run and failed ADCP/CTD measurement results, in order to understand the flow structure of SOI, more realistic modeling based on accurate CTD/ADCP measurements are demanding. The more detailed figure regarding the model based on present study measurement are shown in Appendix B.

Additional test runs according to Section 2.1 are modeled to attain a comprehensive understanding of the SOI hydrodynamics. The three complete CTD/ADCP data by Altıok et al. [6] and IU-IMSM (2009), which represent the upper and lower layers blockages and two-layer flow scenarios, provided the comparison and validating models. In addition, other sources such as measured ADCP data by Özsoy et al. [4, 5] and as model input data from Bosphorus-ROMS (Sözer [15]) and Bosphorus-TSS (Sannino et al., [16]) are used as input values for more test runs. The overall description regarding the test runs is shown in Table 5.1.

Note. The final comprehensive description regarding the present study is shown in Appendix A.

Table 5.1 presents the detailed information regarding the test runs. Noted that this table represent test run BU as the model on this study measurement, tests *A*, *B* and *C* as validation runs provided by Altıok et al. [6] and IU-IMSM (2009), Test Runs *D* to *Z* in presented order at table, as measured and test runs *O*, *U*, *V*, *W*, *X* and *Y* as complimentary computed flow scenarios. The resultant flow conditions of the scenarios are categorized in 10 two-layer flow, four ULB and seven LLB occurrences.

The upper and lower flow BC values used as input for the present model are shown in Figure 5.1. This figure presents that the flow rate values of conducted measurements on SOI in North boundary are covered in the range of previous measured or computed values. In this table Möller [11] and Özsoy et al. [4, 5] are the measurement flow data source in green circles. In addition, the existing computed/modeled sources by Sözer [15] and Sannino et al. [16] are introduced in triangle and square signs.

Table 5.1. Test runs description table.

Description for Strait of Istanbul Hydrodynamic Modeling by EFDC_Explorer				Input Flow Boundary Condition for Model (Southward "+" Northward "-")			Water Level Difference $\Delta h =$ ($h_{North} - h_{South}$)		Flow Condition (Predicted by Model)
Test Case	Data Source	Type	Date	Q_U	Q_L	Q_{Net} ($Q_U + Q_L$)	Present Model	Meas.(M) Comp.(C)	
				m^3/s	m^3/s	m^3/s	cm	cm	
BU	Otay et al. (2015)	Meas.	23-Jun-15	21,000	-7,000	14,000	16	14(M)	Two-L
A	IU-IMSM (2009)	Meas.	17-Feb-09	13,195	-7,360	5,835	26	35(M)	Two-L
B	Altıok et al. (2014)	Meas.	22-Oct-03	6,015	-23,846	-17,831	-9.5	-	ULB
C	Altıok et al. (2014)	Meas.	28-Feb-03	25,285	0	25,285	38	38.5(M)	LLB
D	Özsoy et al. (1996)	Meas.	N/A	13,435	-5,740	7,695	26.3	-	Two-L
E	Özsoy et al. (1996)	Meas.	N/A	8,287	-8,287	0	20	-	Two-L
H	Özsoy et al. (1996)	Meas.	N/A	4,256	-11,012	-6,756	6.4	-	ULB
K	Özsoy et al. (1995)	Meas.	18-May-92	19,000	-4,000	15,000	34	-	LLB
L	Özsoy et al. (1995)	Meas.	15-May-92	30,000	0	30,000	44	-	LLB
M	Özsoy et al. (1995)	Meas.	2-Sep-92	4,000	-15,000	-11,000	2.7	-	ULB
N	Özsoy et al. (1995)	Meas.	2-Oct-91	4,000	-9,500	-5,500	9.7	-	Two-L
P	Özsoy et al. (1995)	Meas.	14-May-92	32,000	0	32,000	49	-	LLB
Q	Özsoy et al. (1996)	Meas.	N/A	10,030	-7,382	2,648	20.5	-	Two-L
R	Özsoy et al. (1996)	Meas.	N/A	17,128	-4,256	12,872	32	-	LLB
Z	Özsoy et al. (1996)	Meas.	N/A	6,923	-9,139	-2,216	16	-	Two-L
O	Sannino et al. (2016) Sözer (2013)	Comp.	generic	9,950	-4,550	5,400	25	12.6(C) 22(C)	Two-L
U	Sannino et al. (2016) Sözer (2013)	Comp.	generic	19,200	1,200	18,000	36	24.6(C) 34.6(C)	LLB
V	Sannino et al. (2016)	Comp.	generic	50,000	0	50,000	88	91.1(C)	LLB
W	Sannino et al. (2016) Sözer (2013)	Comp.	generic	6,950	-6,950	0	18.7	9(C) 16.9(C)	Two-L
X	Sannino et al. (2016) Sözer (2013)	Comp.	generic	13,000	-3,400	9,600	16.6	16.7(C) 25.6(C)	Two-L
Y	Sannino et al. (2016) Sözer (2013)	Comp.	generic	1,900	-11,500	-9,600	2.9	2.2(C) 8.9(C)	ULB

The upper and lower flow BC values used as input for the present model are shown in Figure 5.1. This figure presents that the flow rate values of conducted measurements on SOI in North boundary are covered in the range of previous measured or computed values. In this table Möller [11] and Özsoy et al. [4, 5] are the measurement flow data source in green circles. In addition, the existing computed/modeled sources by Sözer [15] and Sannino et al. [16] are introduced in triangle and square signs.

The flow structures and characteristics are correlated to effective parameters which can be measured with no more measurement operation efforts. For instance, the water level difference is a measurable variable which can be analyzed to study the flow characteristics of the SOI directly [13].

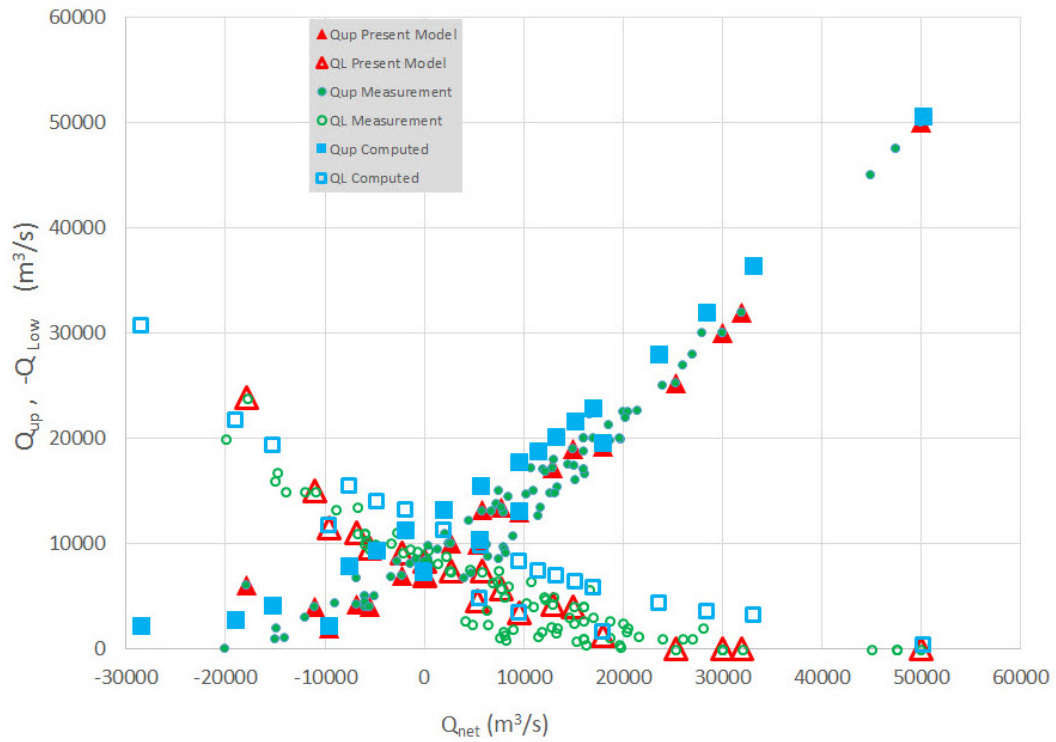


Figure 5.1. Known flow scenarios of the SOI with the used flow boundary values in present model runs highlighted in between (Red points).

5.1. Boundary Input Profiles

5.1.1. Two-layer Flow Scenario, Test Run A

Measured data on 17/Feb/2009 are used to supply boundary values for this test run. The day corresponds calm northerly wind with average speed of $2 m/s$ and flow condition with $Q_U = 13,195 m^3/s$ and $Q_L = -7,360 m^3/s$. 14 number of CTD and ADCP stations are selected as comparison points. The northern and southern flow, salinity and temperature layer-wise BC profiles are presented in Figures 5.2, 5.3 and 5.4.

Noted that Southward flow in flow plot represents the positive direction.

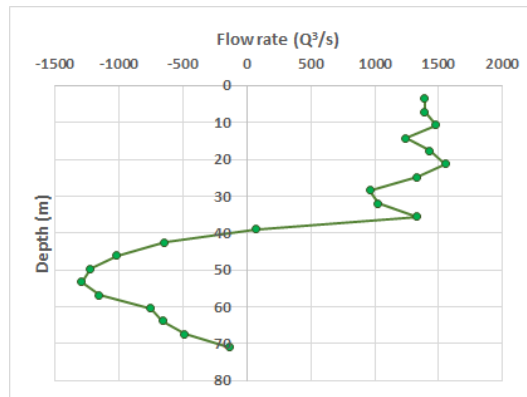
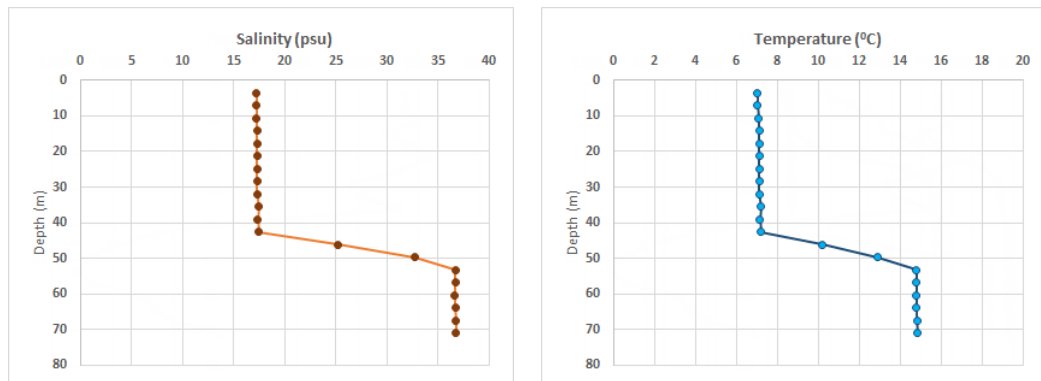


Figure 5.2. Measured flow profile at the North boundary used as input value for Test Run A.



(a) Salinity profile.

(b) Temperature profile.

Figure 5.3. Measured salinity and temperature profiles at the North boundary used as input value for Test Run A.

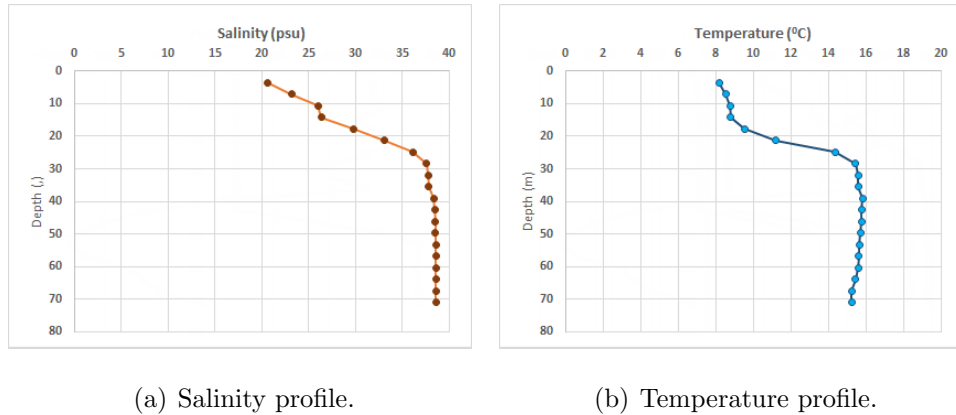


Figure 5.4. Measured salinity and temperature profiles at the South boundary used as input value for Test Run A.

5.1.2. ULB Scenario, Test Run B

Measurement CTD and ADCP data conducted on 22/Oct/2003 demonstrate upper layer blockage event. The strong SW 5.6 m/s wind blowing for three days on measurement day induces strong northward lower layer flow with $Q_L = -23,846 m^3/s$ governs the flow structure against southward upper layer $Q_U = 6,015 m^3/s$. The northern and southern flow, salinity and temperature profiles are shown in Figures 5.5, 5.6 and 5.7.

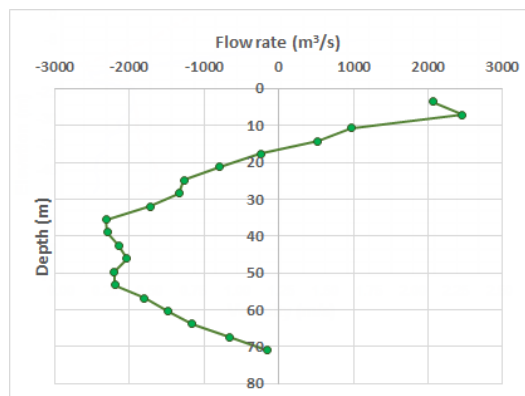


Figure 5.5. Measured flow profile at the North boundary used as input value for Test Run B.

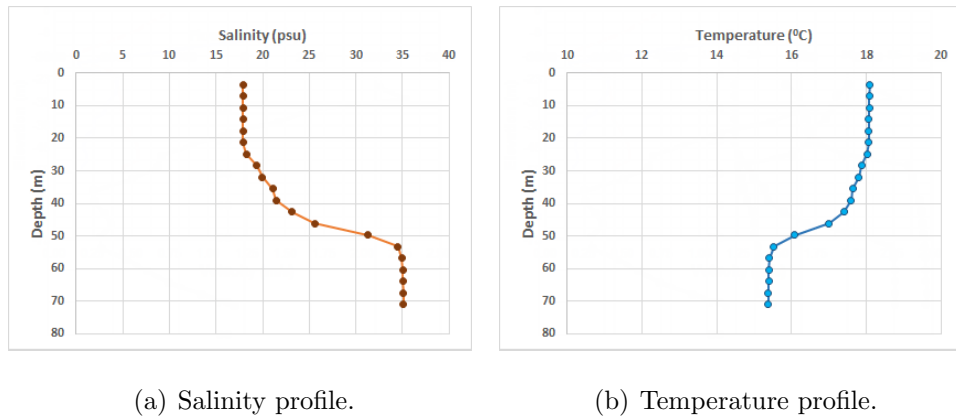


Figure 5.6. Measured salinity and temperature profiles at the North boundary used as input value for Test Run B.

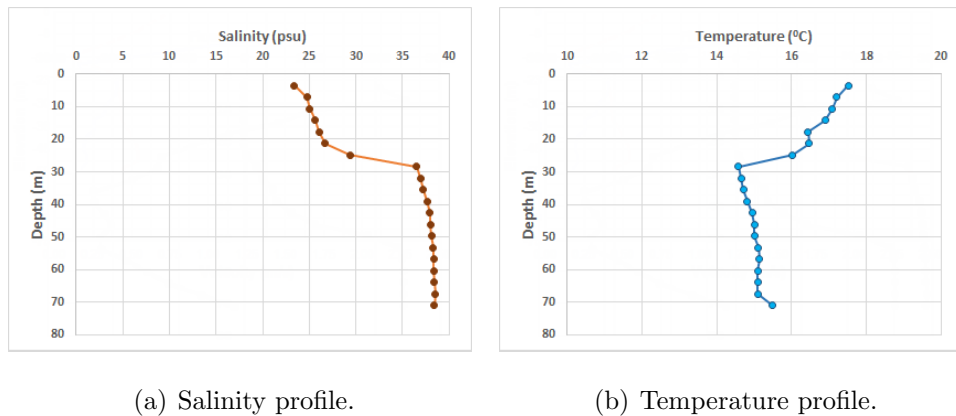


Figure 5.7. Measured salinity and temperature profiles at the South boundary used as input value for Test Run B.

5.1.3. LLB Scenario, Test Run C

This dominant strong northerly wind with an average of 10 m/s on the SOI lasted for three days. Consequently, this meteorological front induces the barotropic gradient prevail the baroclinic gradient and block the northward lower layer flow on 28/Feb/2003. The measured CTD and ADCP data for this day are used to validate the corresponding model result for LLB event.

Number of 10 CTD and ADCP stations (Table C.3), including one cross-sectional continuous current measurement northern, provide BC and comparison values. The used flow boundary values in this test run are $Q_U = 25,285 \text{ m}^3/\text{s}$ and $Q_L \approx 0 \text{ m}^3/\text{s}$ confirms that the lower layer flow never reaches to the north as the evidence for LLB. The straight vertical profiles of the northern and southern flow, salinity, and temperature are the evidence for no existence of different density northward different flow (Figures 5.8, 5.9 and 5.10).

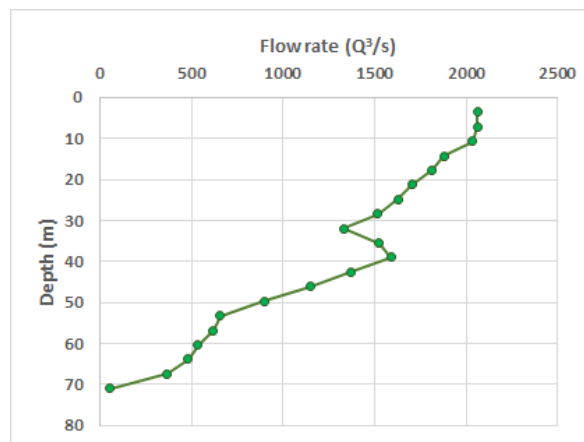
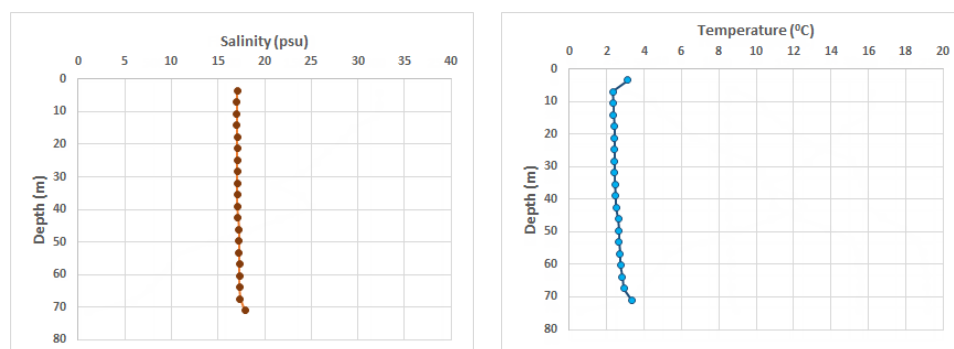


Figure 5.8. Measured flow profile at the North boundary used as input value for Test Run C.



(a) Salinity profile.

(b) Temperature profile.

Figure 5.9. Measured salinity and temperature profiles at the North boundary used as input value for Test Run C.

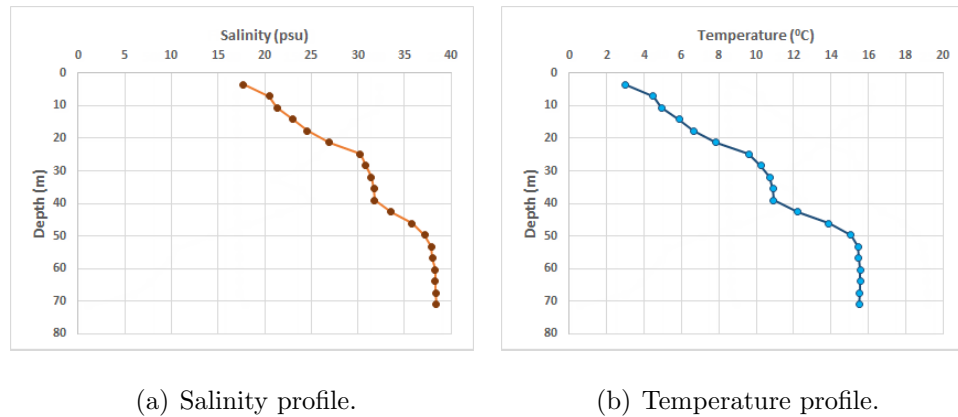


Figure 5.10. Measured salinity and temperature profiles at the South boundary used as input value for Test Run C.

5.2. Validation of Model Results with Measurement (Test Runs A,B,C)

These data sources provide three comprehensive sets of CTD and ADCP data as described in Section 3. Three common hydrodynamic structures, named upper and lower layer blockages and two-layer flow, are included in this data source. These scenarios are modeled by using the measured data as the North and South salinity, temperature and flow boundary values into the EFDC. The models are calibrated by turbulence modeling parameters, shown in Table 4.3, by running numerous test runs in order to achieve best-matching results to the inside domain measured CTD and ADCP comparison data. These calibration parameters will be used as verified constant values in other arbitrary test runs according to the estimated blockages and two-layer or blocked flow events such.

The 3D distribution of salinity in the stratified flow of SOI is shown for the Two-layer flow scenario after five days of the run is presented in Figure 5.11. The upper fresher water is southward in contradiction to northward more saline Mediterranean water.

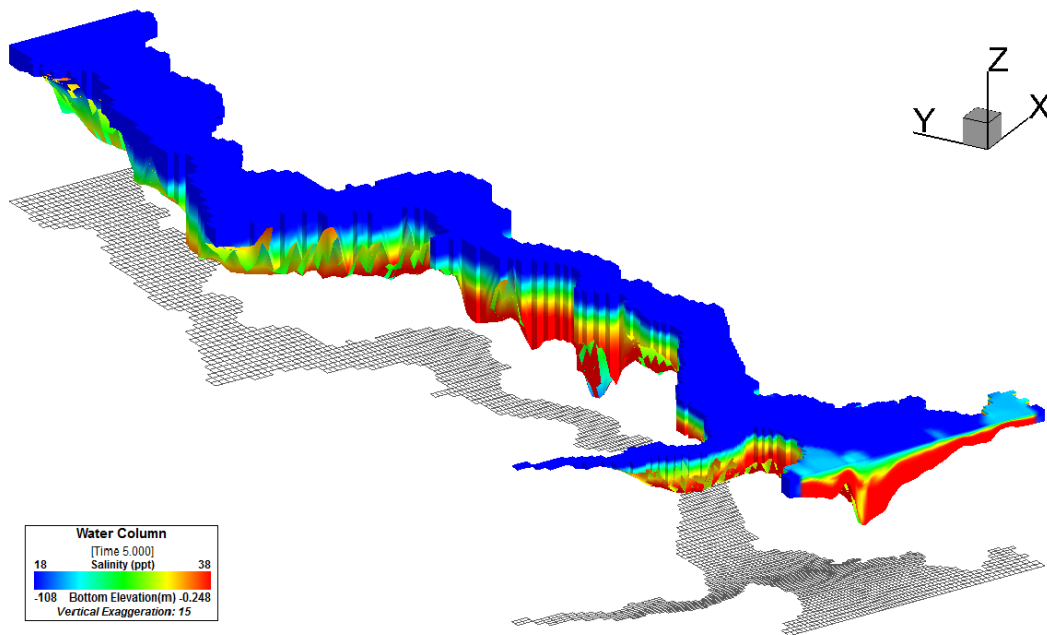


Figure 5.11. 3D salinity distribution along the SOI for Test Run C.

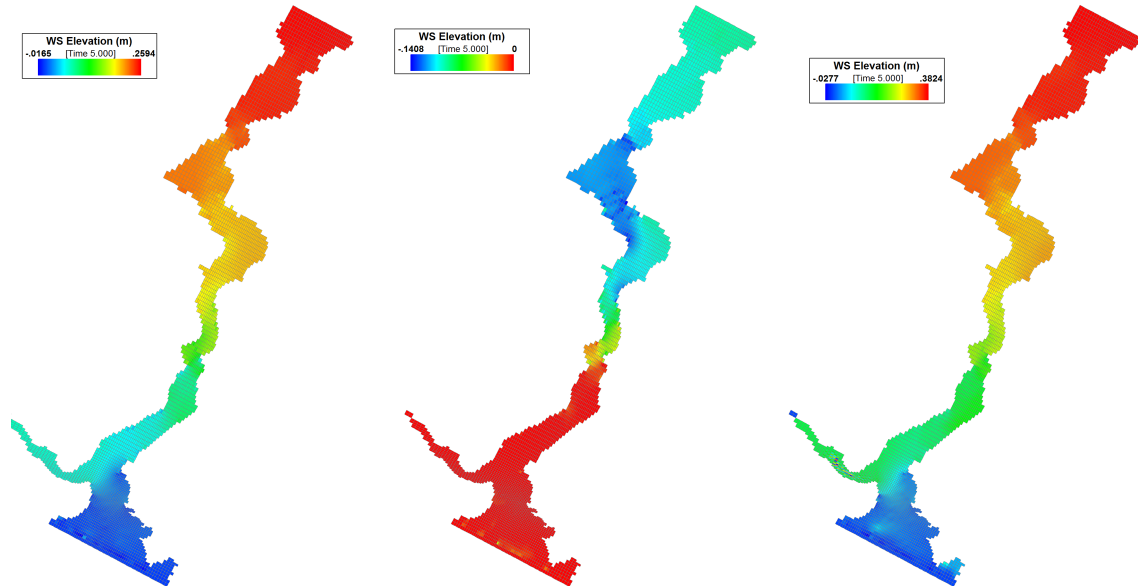
5.2.1. Water Level Difference

Table 5.2 represents the modeled and measured water level difference (WLD) between northern and southern boundaries of SOI domain. The distribution of surface water level regarding validated ULB, LLB, and Two-layer flow scenarios are shown in Figure 5.12.

Despite that the model structure is validated for LLB, ULB, and Two-layer flow scenarios, the water level difference value between two ends of SOI is the critical parameter which responds to hydrodynamic of the strait. Therefore, studying the resulted WLD are compared to available measured/computed values to provide more validation source for the model.

Table 5.2. Description of model and measured/computed water level differences (WLD).

Used Data Source as EFDC Flow BC Value				Flow		Δh	
Test Case	Flow	Water Level Difference	Date	Flow Condition	Q_{net}	Meas.(M) Comp.(C)	Present Model
					m^3/s	cm	cm
A	Meas. and IU-IMSM (2009)	Meas. HGK (2016)	17-Feb-09	Tow-L	13,128	35.0(M)	26.0
C	Meas. Altıok et al. (2014)	Meas. Altıok et al. (2014)	28-Feb-03	LLB	25,285	38.5(M)	38.0
Y	Sannino et al. (2016) Sözer (2013)	Sannino et al. (2016) Sözer (2013)	generic	ULB	-9,600	2.2(C) 8.9(C)	2.9
X	Sannino et al. (2016) Sözer (2013)	Sannino et al. (2016) Sözer (2013)	generic	Tow-L	9,600	16.7(C) 25.6(C)	16.6
V	Sannino et al. (2016)	Sannino et al. (2016)	generic	LLB	50,000	91.1(C)	88.0
O	Sannino et al. (2016) Sözer (2013)	Sannino et al. (2016) Sözer (2013)	generic	Two-L	5,400	12.6(C) 22.0(C)	25
U	Sannino et al. (2016) Sözer (2013)	Sannino et al. (2016) Sözer (2013)	generic	LLB	18,000	24.6(C) 34.6(C)	36
W	Sannino et al. (2016) Sözer (2013)	Sannino et al. (2016) Sözer (2013)	generic	Two-L	0	9.0(C) 16.9(C)	18.7



(a) Test Run A, Two-layer flow. (b) Test Run B, LLB. (c) Test Run C, ULB.

Figure 5.12. Water level difference distribution along the SOI, Test Runs A,B,C.

Maderich and Konstantinov [13] proposed simplified quasi-steady two-layer model regarding the two ends water level difference (WLD) and flow regimes of the Strait of Istanbul. The named study uses two-layer hydrostatic flow assumption and internal composite Froude number to define a simplified equilibrium between flow regimes and cross-sectional geometry of rectangular strait [10]. They used Özsoy and Möller's measurements as flow values to integrate the corresponding WLD (Test Runs *D, E, H, R, Q* and *Z*). The Figure 5.13 correlates the flow and WLD between Maderich and Konstantinov [13] and all the test runs excluding test run *BU, V, X* and *Y*.

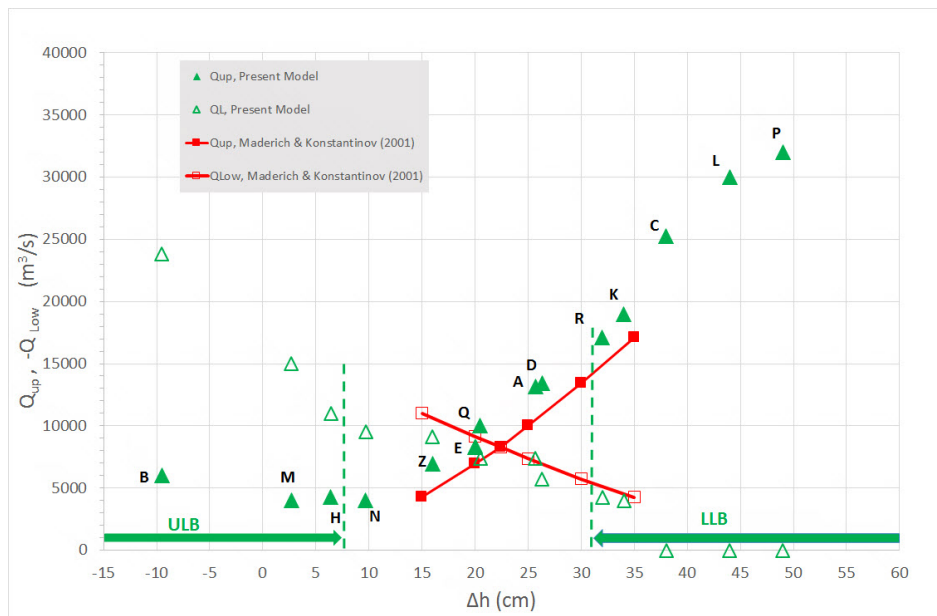


Figure 5.13. Correlation the plot between water level The difference (WLD) versus used upper and lower layers flow values as model's flow BC. Corresponding test run titles are shown adjacent to points.

The trend of modeled WLD to the upper and lower flow rate values are matching corresponding measurement values with some deviances. The reason can be explained by the fact that Maderich's simplified the model does not consider baroclinic gradient in a simplified model in comparison to present model which evaluates all governing equations to the domain. The present model predicts that the blockage events for

the lower and upper layers occur for Δh larger than 32 cm and smaller than 8 cm, respectively.

The model resultant WLD values are compared to other modeled sources including Bosphorus (ROMS) and Bosphorus (TSS) in Figure 5.14. The figure shows that the present model finely matches to the Bosphorus (ROMS) model rather than Bosphorus (TSS) which is a larger domain covering all Turkish Strait System in which the SOI is included as a small zone of the domain. The blockage occurrences are presented by net flow and WLD correlation. The model predicts blockage event for the approximate net flows larger than 12,900 m^3/s and less than -6,700 m^3/s in the lower and upper layers, respectively.

Figure 5.15 suggests correlation plot between EFDC model versus 8 available measured or computed WLD values according to Table 5.2. The high quantity of R^2 value and well-distribution of the correlation WLD points around 45° line state appropriately results between model and measured/compared values.

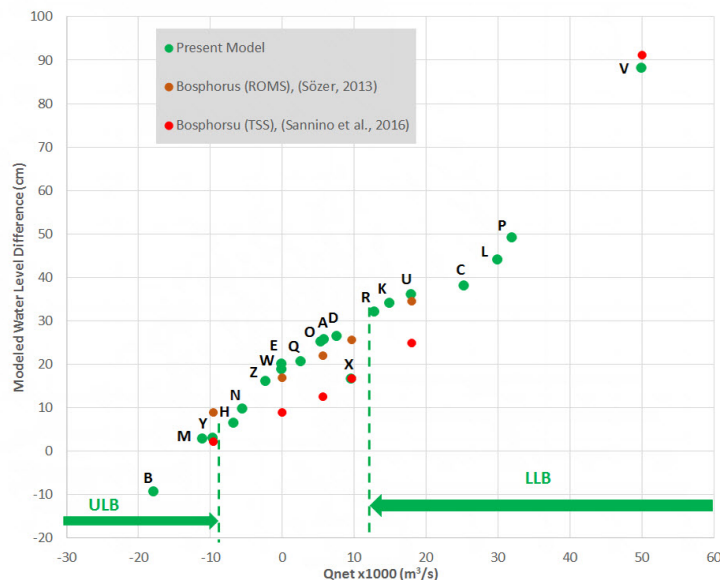


Figure 5.14. Net flow and WLD correlation plot.

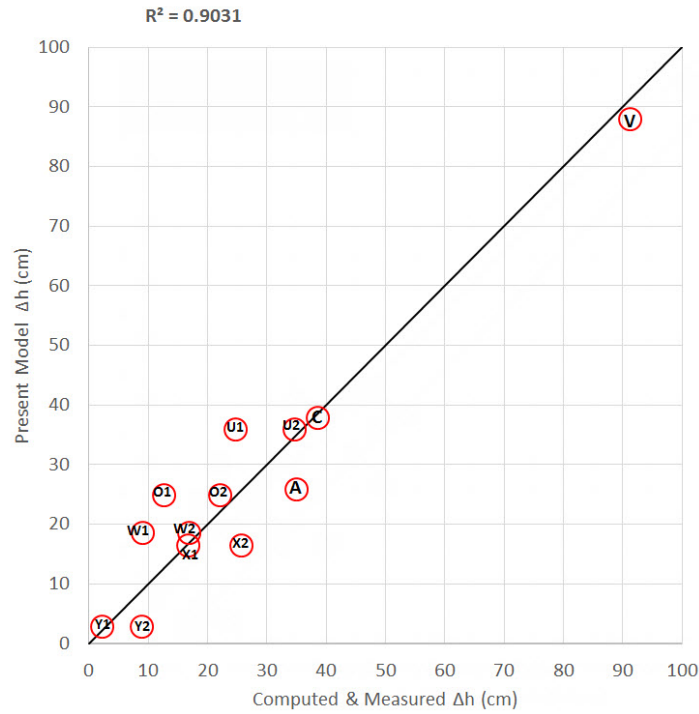


Figure 5.15. WLD correlation plot for present model versus available computed / measured. i.e. (Y1,W1,O1,U1,X1) and (Y2,W2,O2,U2,X2) represent Bosphorus-TSS and Bosphorus-ROMS models, respectively.

5.2.2. Vertical Profiles of Salinity, Temperature, and Velocity at Multiple Cross-sections Along the Strait

Regarding the Two-layer flow scenario; the salinity, temperature, and velocity are compared to measured data in stations shown in Figure 5.16. After calibration step by trial and error by changing on hydrodynamic parameters, the vertical profiles are matched to the experiment. Noted that according to these comparison plots, the horizontal gradients error generates deviances between model and experiment results which are due to the Sigma coordinate system used by EFDC program [31].

According to Figure 5.16, as model approaches to south of domain, the mixing layer thickness and properties such as values and trends are being best-matched in

salinity and temperature plots (first and second columns). This provides the model to have realistic results in front of GH which is this study's focus zone. Regarding the velocity comparison plots (third column), the mixing layer elevation (sharp edges) are properly distinguished by model and the trend of velocities fit the measurement. The upper layer velocity magnitudes are close to the measured data whereas in lower parts the model shows smaller quantities. Five selective points are plotted and the other comparison profiles in other stations are presented in Appendix C, Figure C.2.

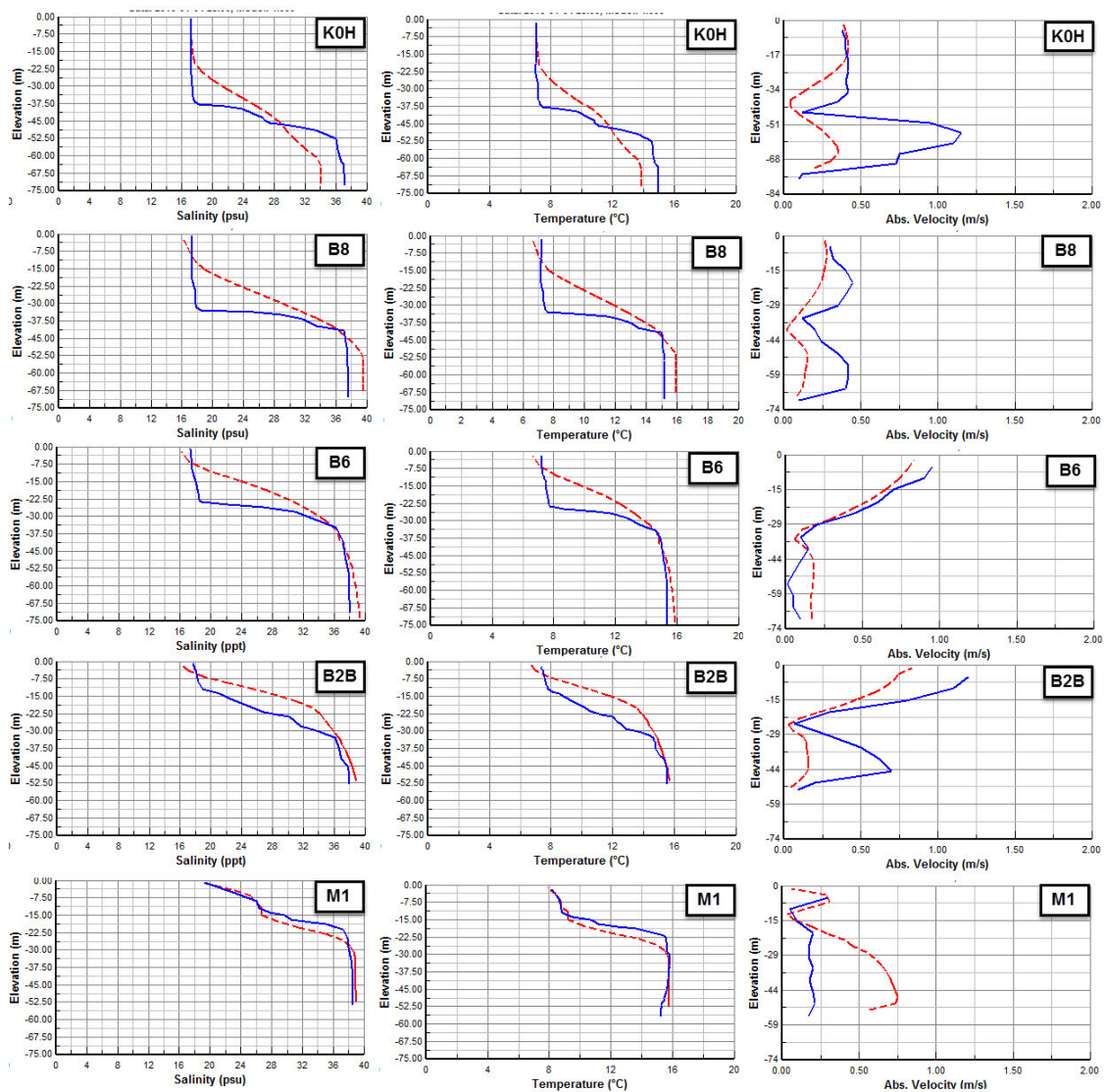


Figure 5.16. Comparison plots for model versus measured data IU-IMSM (2009), Test

Run A. Columns represent salinity, temperature and absolute velocity magnitude

$|\vec{V}| = \sqrt{V_{East}^2 + V_{North}^2}$. Model result is shown in Red and experiment results in Blue.

For the ULB scenario; according to measured data in 10 station (Table C.2), calibrated model is validated including errors in distinguishing the vertical mixing layer thickness and values which are imposed by Sigma coordinate system. In addition, it is obvious that as checkpoints get close to northern flow boundary this vertical profile mixing introduces, more deviance from measurement data on mixing layer trend and thickness are being obtained, Figure (5.17).

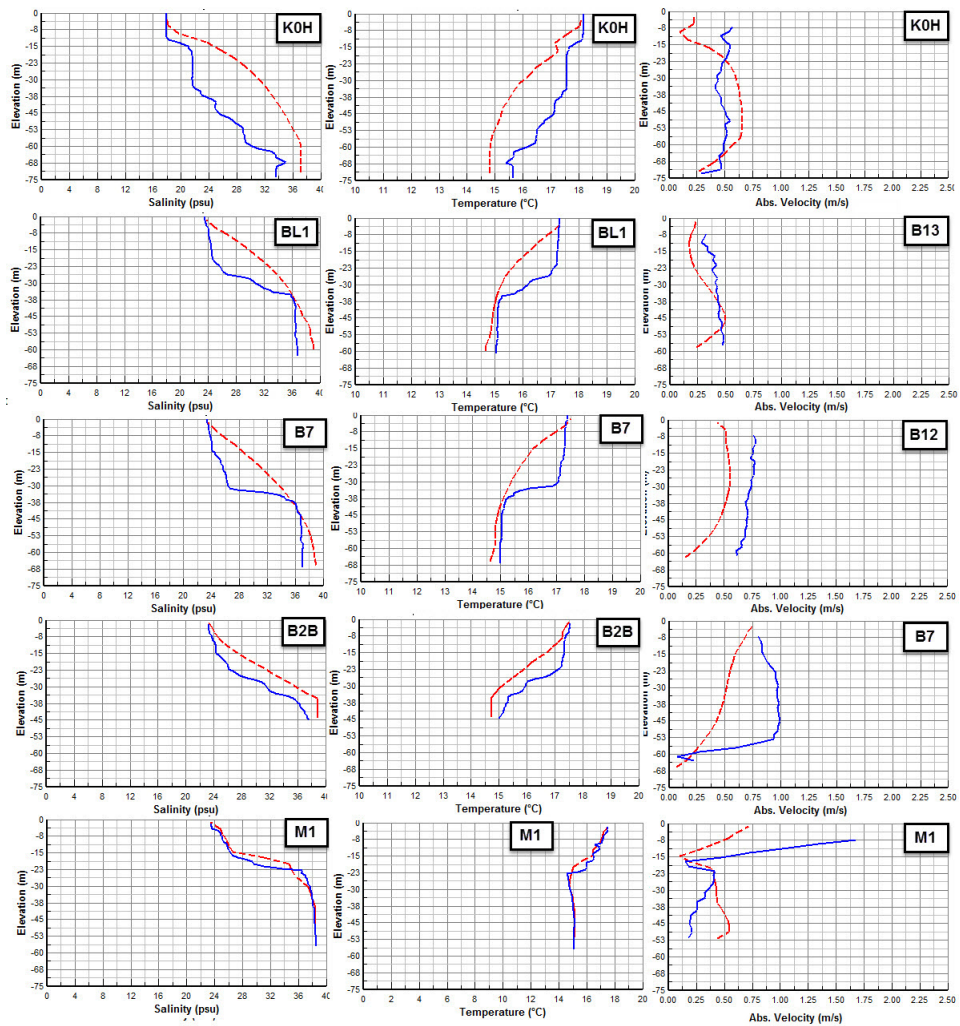


Figure 5.17. Comparison plots for model versus measured data [6], test Run B. Columns represent salinity, temperature and absolute velocity magnitude $|\vec{V}| = \sqrt{V_{East}^2 + V_{North}^2}$. Model result is marked in Red and experiment results in Blue.

According to comparison plots in this figure, the model have predicted the salinity and temperature profiles match to measured quantities, especially in the upper and lower sections of vertical profiles. Due to horizontal gradient error of Sigma coordinate system, the trend of mixing layer has deviances to the measured data (first and second columns). Five selective points are plotted and the other comparison profiles in other stations are presented in Appendix C, Figure C.3.

Regarding the LLB scenario; the calibration by hydrodynamic parameters, from Table 4.3, result in satisfying comparison in the 10 measurement points, Figure C.1. By straight vertical salinity and temperature profiles in Figure 5.18, the lower layer blockage occurrence is obvious; The northern profiles do not present any saline water from the Marmara Sea; therefore, the water body is consist of fresher Black Sea water with salinity around 17 *psu* (St. K0 to BL1 stations at Figure C.1). The St. B7 shape on lower parts of vertical profile demonstrates the existence of northward flow; therefore, it is a conclusion for distinguishing the location of LLB in front of Rumelihisar coast. The realistic model result is obtained by this LLB scenario. In velocity plots, the mixing layer elevation and magnitudes are matched to the measurement data satisfying. Five selective points are plotted and the other comparison profiles in other stations are presented in Appendix C, Figure C.4.

Three common flow structure in SOI are covered by this data source. The calibrated turbulence parameters are introduced for scenarios to expedite the consuming time for establishing further test runs. The model structure is tested appropriately by comparing to measure data.

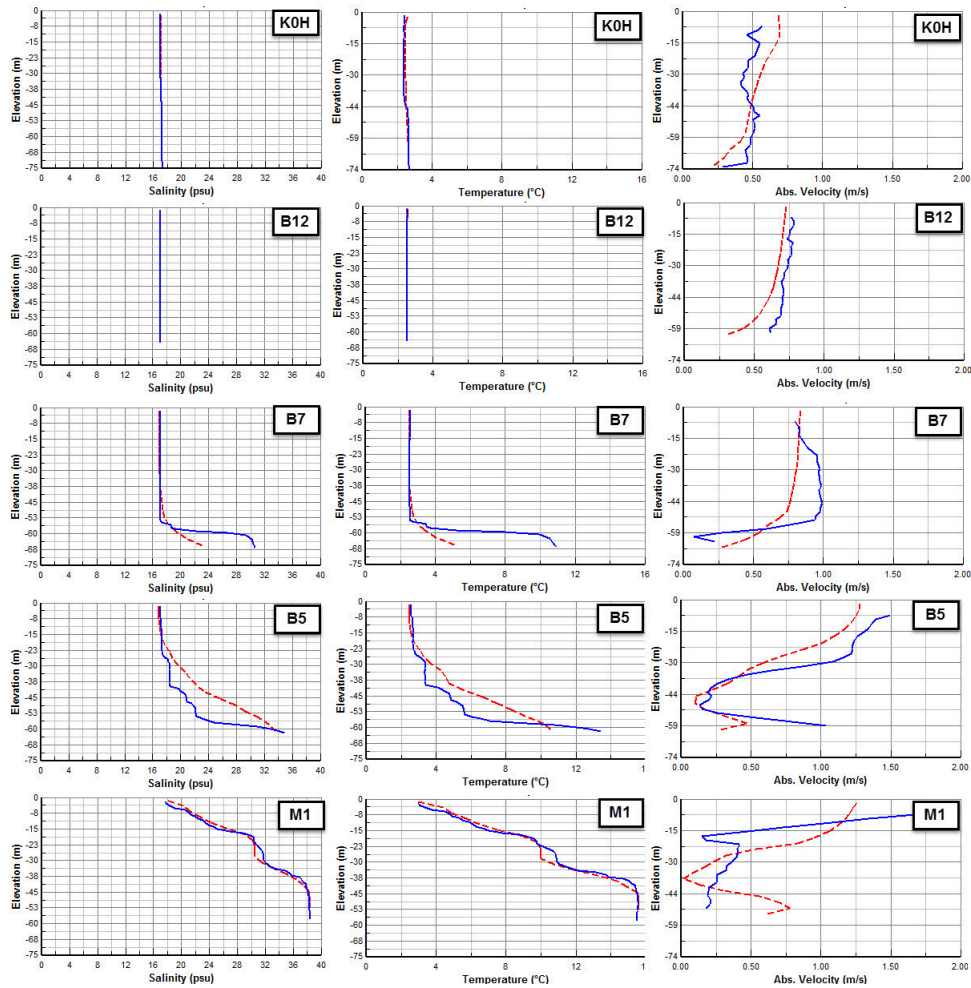


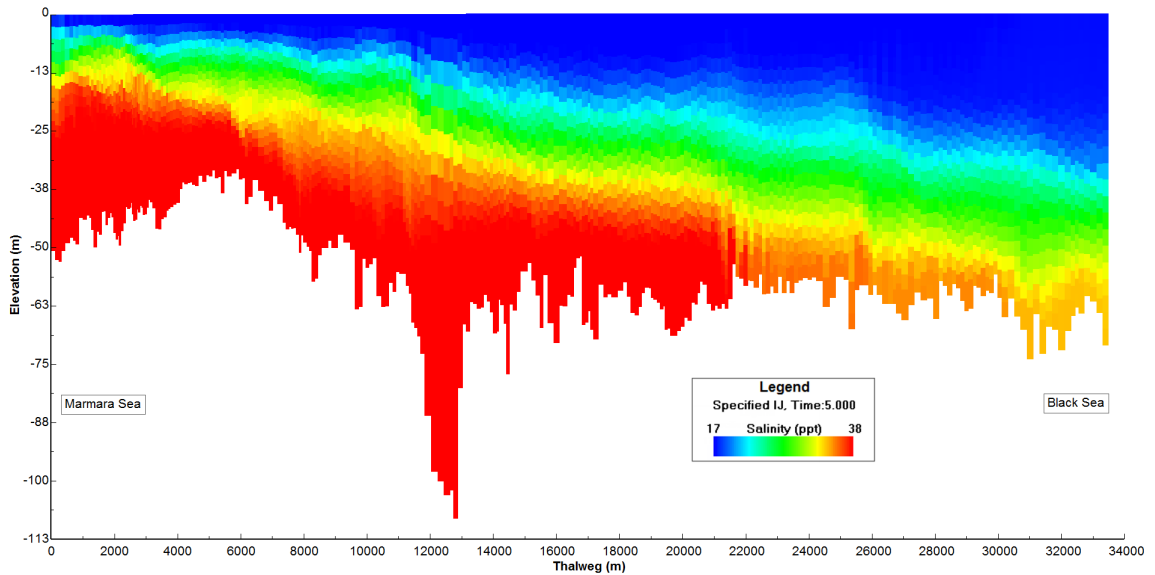
Figure 5.18. Comparison plots for model versus measured data [6], test Run C. Columns represent salinity, temperature and absolute velocity magnitude $|\vec{V}| = \sqrt{V_{East}^2 + V_{North}^2}$. Model result is marked in Red and experiment results in Blue.

5.3. Presentation of Model Results

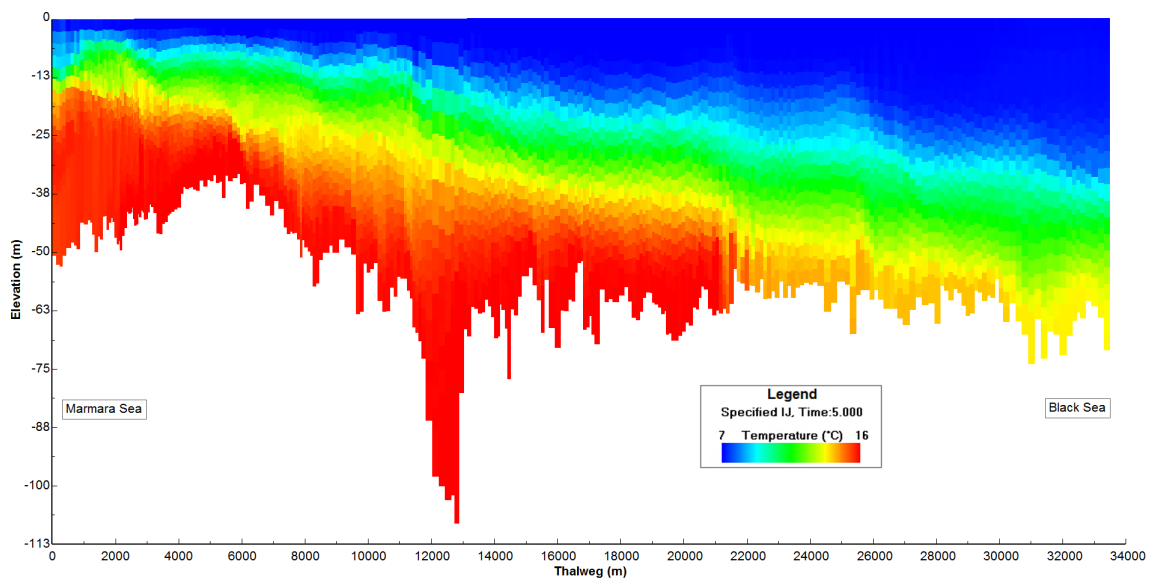
5.3.1. Vertical Distribution of Salinity, Temperature, Density and Velocity Along the Thalweg

Regarding the Two-layer flow scenario; considering 21 and 33 *psu* as upper and lower identification of interface layer salinity values for the stratified two-layer flow test run, the 12 *m* thickness interface layer at the north of SOI is found at 42 *m* to 54 *m*

depths. The interface layer at South boundary reaches the 8 *m* thickness from 4 *m* to 12 *m* depth for the southern zone in kilometer one on the thalweg line (Figure 5.19). The temperature and density profiles have the same trend of salinity profile, warmer Marmara water follows the baroclinic deviance to favor lower layer to reach the Black Sea.

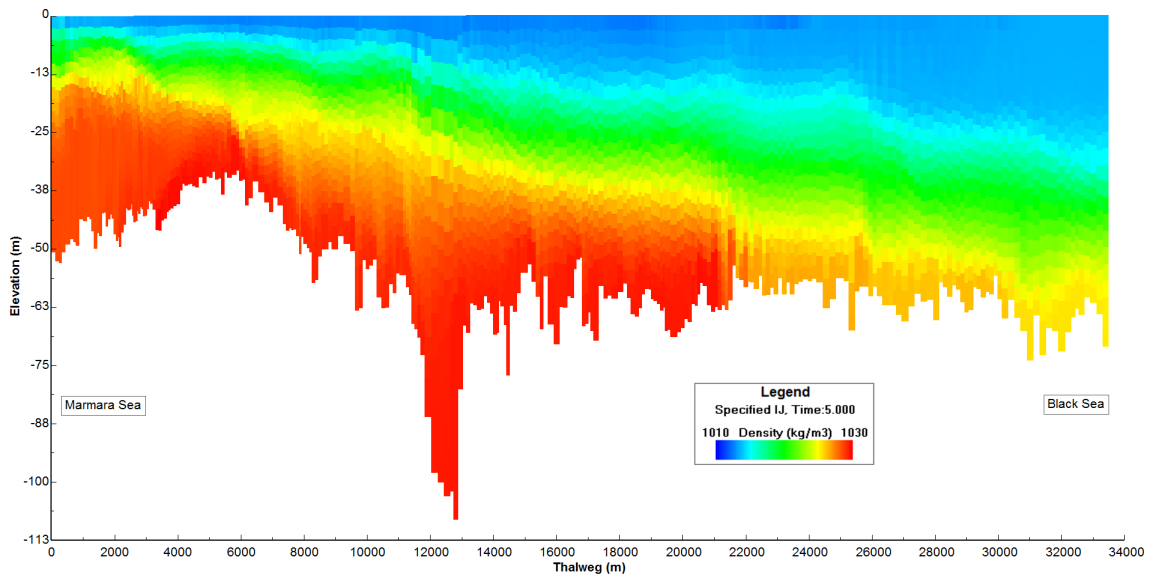


(a) Salinity profile.



(b) Temperature profile.

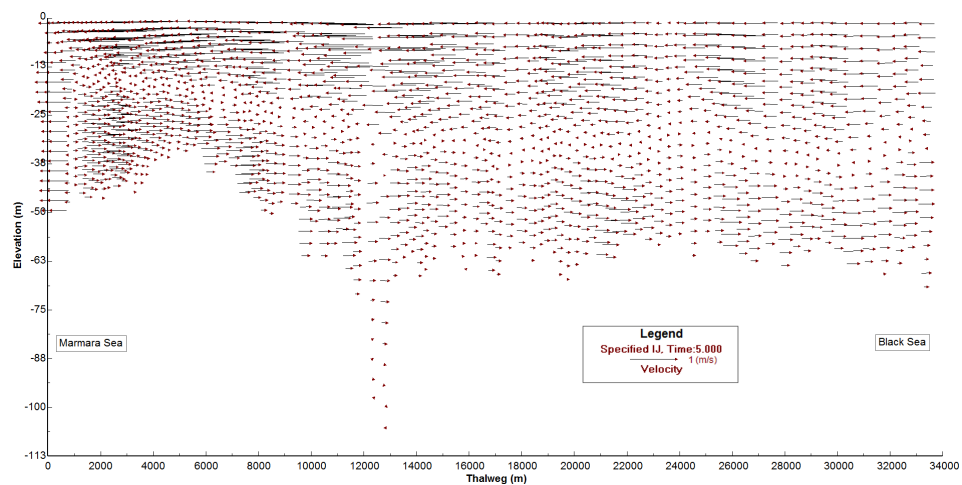
Figure 5.19. Thalweg line longitudinal-section profiles for Test Run A.



(c) Density profile

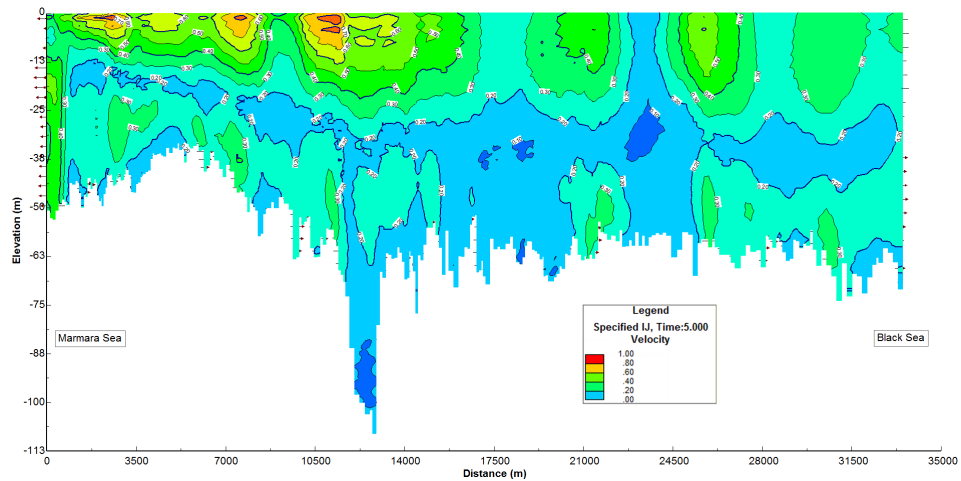
Figure 5.19. Thalweg line longitudinal-section profiles for Test Run A(cont.).

The two-layer flow condition is distinguished by interface layer between upper southward and lower northward velocity vectors on thalweg line, as shown in Figure 5.20(a). The minimum velocities are allocated to interface layer for two opposite direction flow meet each others.



(a) Velocity vectors.

Figure 5.20. Thalweg line longitudinal-section velocity profiles for Test Run A.



(b) Velocity contour.

Figure 5.20. Thalweg line longitudinal-section velocity profiles for Test Run A (cont.).

Note. For below-described LLB and ULB scenarios, the figures are presented in Appendix C.

Regarding the LLB scenario; According to Figure C.5(a), it is observed that the LLB occurs near to Bebek coast at the deepest bottom elevation. As the The Marmara Sea blocks, the small quantity of mixing occurred. The interface layer has 10 *m* thickness at southern boundary and reaches to minimum value at blockage point (St. B7). According to Figure C.6 which describes the northern cross-section of the domain, the Black Sea water with the salinity of around 17 *psu* uniformly distributed in the vertical direction.

The $Q_U = 25,285 \text{ m}^3/\text{s}$ is dominant flushing flow through the domain. Figure C.9(a) depicts the velocity vectors corresponding to this test run in which the northward flow is diminished at kilometer 13 on thalweg line with at the depth of 104 *m*. As the two opposite directional flow reach each other, the interface layer is shaped. Hence, the reduction in thickness of southward governing flow increases the velocity in the upper layer, as shown in Figure C.9(b).

Regarding the ULB scenario; Salinity and temperature plots in Figure C.7(a) prove that ULB occurs on the northern part the strait, in front of Anadolukavağı coast. The Black Sea water cannot proceed southward; therefore, the channel is filled with Marmara Sea saline water. In this case, the vertical stratification of Marmara Sea steps into the SOI and the small quantity of mixing between two seas occurs at blockage zone at northern part. The halocline moves upward so that the Marmara saline water flushes into the Black Sea readily and interface layer is created in short longitudinal length of the strait. Figure C.8 presents the salinity and temperature distribution at the very northern part of the SOI.

The thalweg velocity profile is shown on Figure C.10(a) represents the occurrence of ULB at Anadolukavağı coast. The northward Marmara Sea lower layer flow easily flushes to the Black Sea except small disturbance under northern short interface zone after blockage zone. Under the blockage zone, the lower layer flow speeds up towards the Black Sea exit due to suppression by upper blocked Black Sea water, as shown in Figure C.10(b).

Further plots of Test Run B regarding bed shear stress and Densimetric Froude number as hydraulic control of system have been presented in Appendix C, Figures C.11 and C.12 .

5.3.2. Horizontal Distribution of Surface Velocities Along the Strait of Istanbul

For Two-layer flow condition (Test Run A), the northward lower layer velocity reaches the maximum magnitudes of 0.40 m/s and 0.47 m/s at 60 m depth at Beşiktaş and Tarabya coasts. The maximum southward velocity recorded as 1 m/s at surface layer at the narrowest width of SOI in Bebek coast and in front of Haydarpaşa coast, as shown Figure 5.21(b). The surface water inflows with magnitude of 0.16 m/s towards GH estuary with no any eddy current at junction, as shown in Figure 5.21(a).

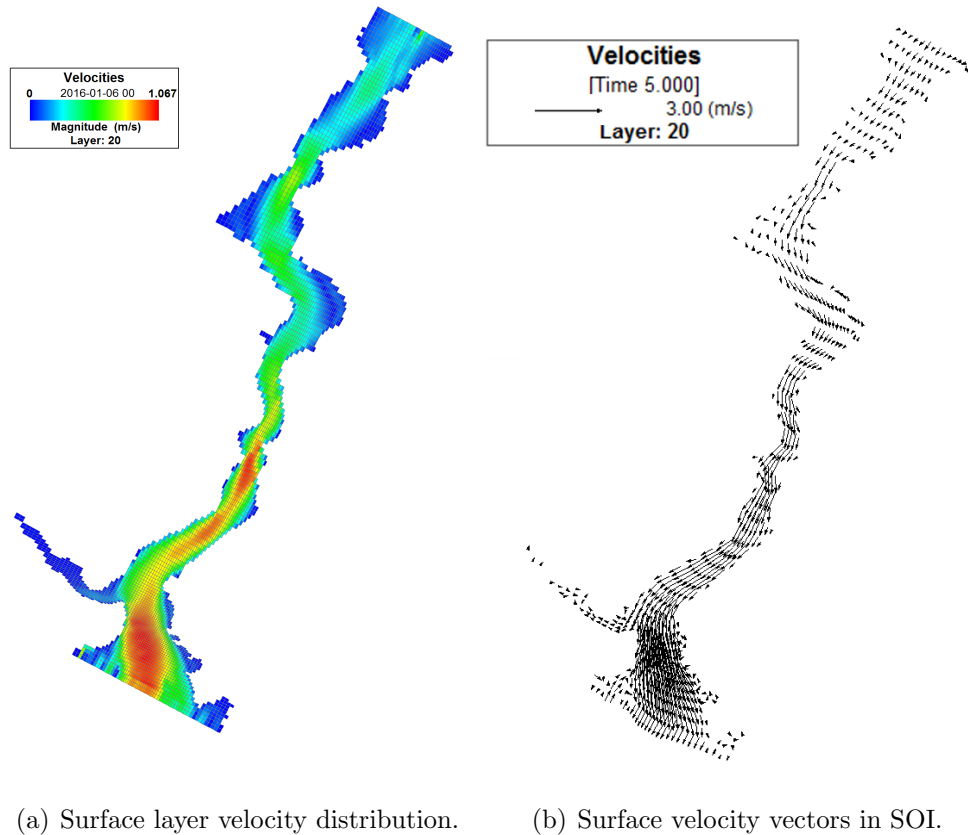
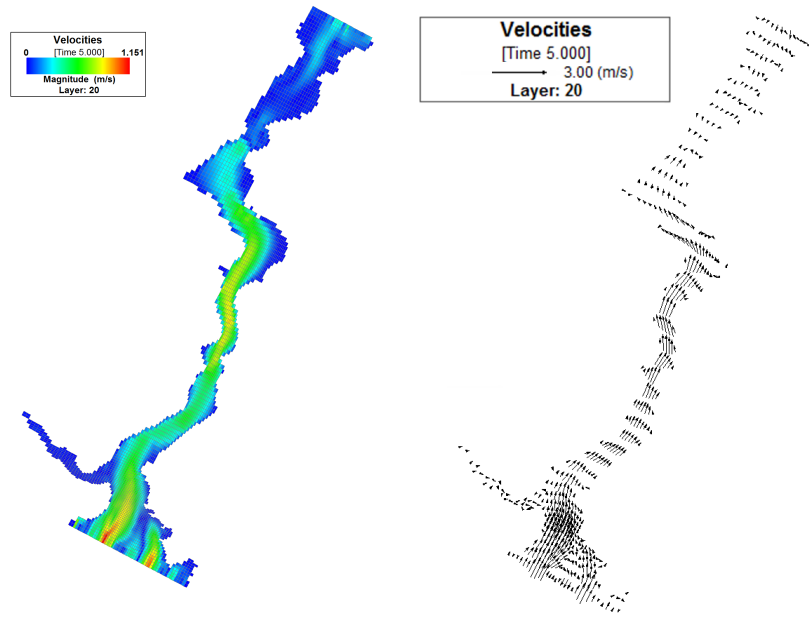


Figure 5.21. Surface water velocity plots for Test Run A.

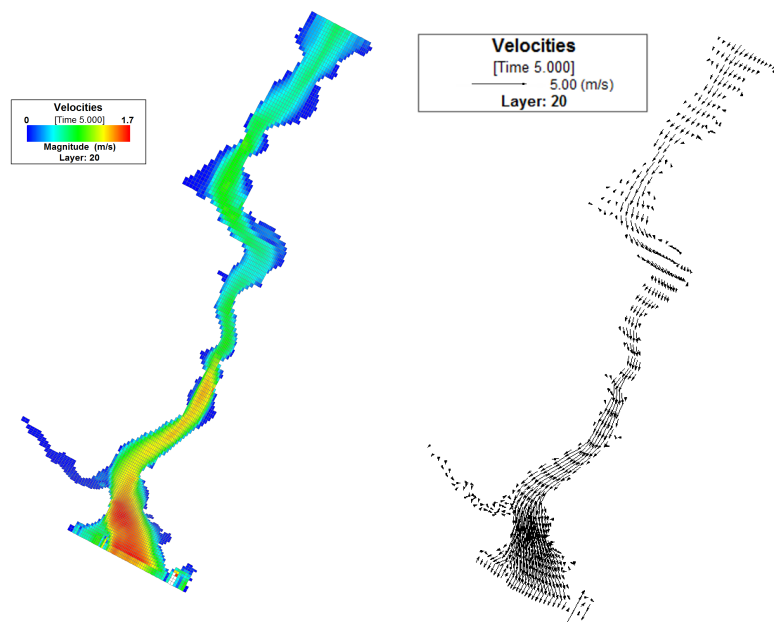
For ULB flow condition (Test Run B), the maximum flow velocity is 0.90 m/s which is apparent at surface layer between Bebek and Istinye, as shown in Figure 5.22(a). Despite that there is large CCW surface eddy at the junction of GH and SOI, on the surface, the water flows out from GH with a small magnitude of 0.04 m/s , as presented in Figure 5.22(b).

For LLB flow condition (Test Run C), the maximum velocity is recorded on kilometer 3 with quantity of 1.7 m/s . The surface water velocity in narrowest location of SOI reaches to 1.4 m/s , as shown in Figure 5.23(b). At GH and SOI junction clockwise (CW) flow prevents the surface water of main strait to flush into Golden Horn, as shown in Figure 5.23(b).



(a) Surface layer velocity distribution. (b) Surface velocity vectors in SOI.

Figure 5.22. Surface water velocity plots for Test Run B.



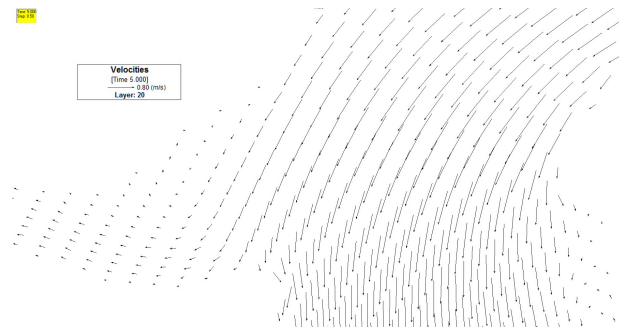
(a) Surface layer velocity distribution. (b) Surface velocity vectors in SOI.

Figure 5.23. Surface water velocity plots for Test Run C.

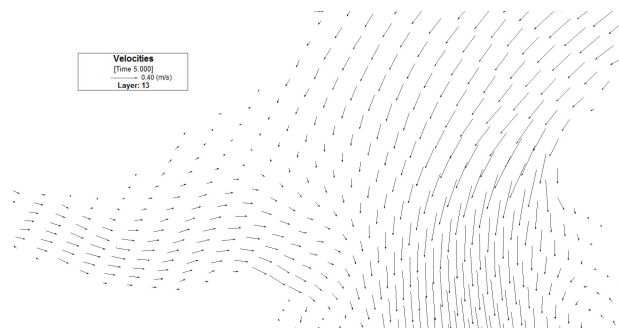
5.4. Hydrodynamics of the Junction of Golden Horn

5.4.1. Horizontal Velocity Distribution of Surface, Interface and Bottom Layers at Junction of Golden Horn

For Two-layer flow condition (Test Run A), the current's behavior in the surface, interface and bottom layers are compared in Figure 5.24. According to the main strait surface flow, the flow, in following of upper layer direction, flushes toward the Marmara Sea while the some collide to the Sarayburnu and stir towards Golden Horn with no eddy generating. In layer 13 (~ 14 m depth), interface layer outflows from Golden Horn in parallel to main strait flow. In Layer 9 (~ 22 m depth) the main strait flow flushes northward and the CCW eddy currents at the junction are created in which this trend complies until the bottom layer.



(a) Surface layer- Layer 20.



(b) Interface layer- Layer 13 (~ 14 m).

Figure 5.24. Water level difference (WLD) distribution plot for Test Run A. (Layer 1 and 20 describe lower and upper layers, respectively).

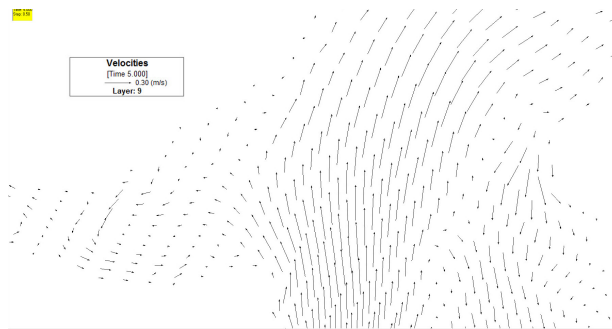
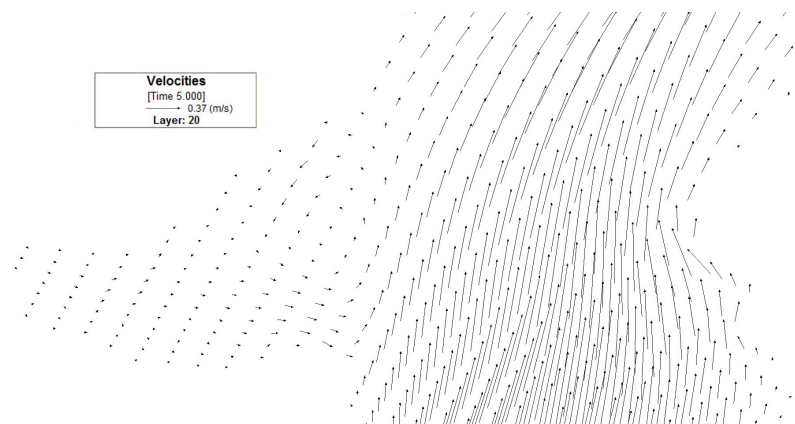
(c) Lower layer- Layer 9 ($\sim -22m$).

Figure 5.24. Water level difference (WLD) distribution plot for Test Run A (cont.).

The ULB condition generates dominant northward flow inside the main channel for all layers surrounding GH junction while the distribution of velocity vectors are different at junction towards the GH, Figure 5.25(a). In the surface water layer, due to the separation of northward flow of the main channel in front of Galata coast which creates CCW eddy currents at the junction. The interface layer is located at Layer 12 ($\sim 16 m$ depth) in which the current outflows from GH and moves northward in parallel to main channel flow, Figure 5.25(b). Below the interface layer, at Layer 7 ($\sim 26 m$ depth) flow of junction changes the trend by generation CCW eddies, Figure 5.25(c).



(a) Surface layer- Layer 20.

Figure 5.25. Layer-wise velocity vectors at junction of GH for Test Run B.

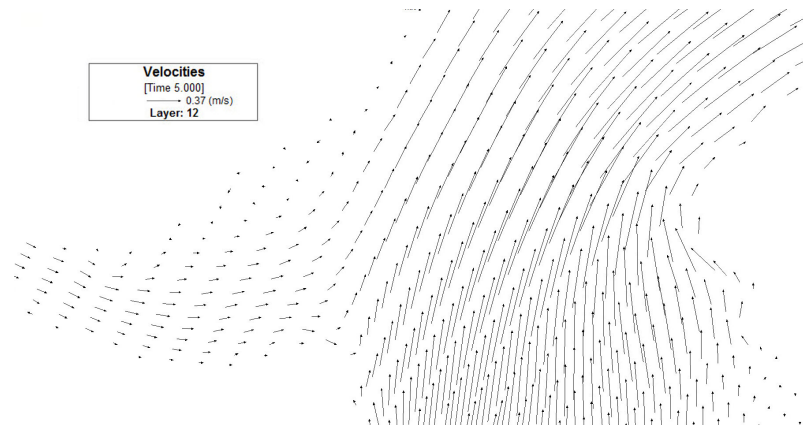
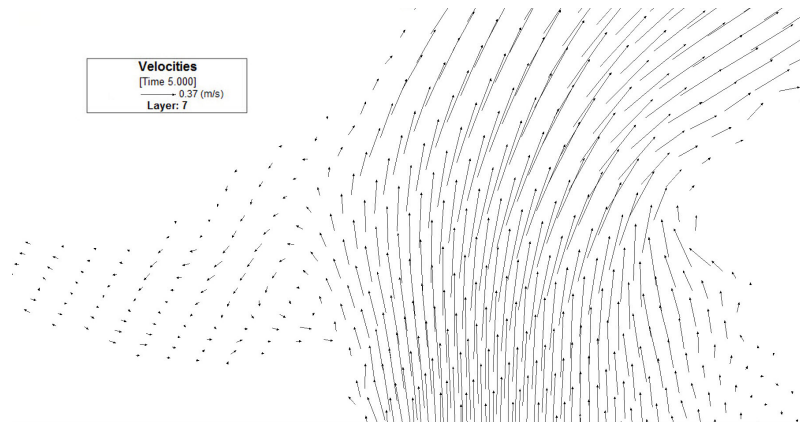
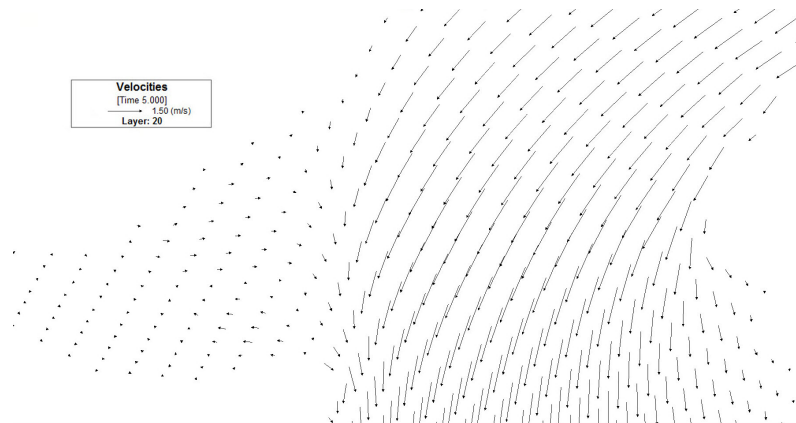
(b) Interface layer- Layer 12($\sim -16m$).(c) Lower layer- Layer 7($\sim -26m$).

Figure 5.25. Layer-wise velocity vectors at junction of GH for Test Run B (cont).

For LLB flow condition (Test Run C), the surface current at main strait flow out towards Marmara Sea exit and in the GH junction small quantity currents outflow from estuary, Figure 5.26(a). As the flow structure is LLB the southward flows allocates the thickness to upper layer flows. Hence, the interface depth moves deeper to Layer 6 ($\sim 28 m$ depth) in which the flow direction the main strait is complicated as presented in Figure 5.26(b). The left side of the main channel as the deeper part water moves northwards compared to southward flow in right side. For this layer, in the Golden Horn junction, the flow leaves the estuary and collides to the main complex flow in interface layer. The bottom layer 2 ($\sim 36 m$ depth) main strait flows northwards while some of this marmara Sea water inflows to GH at junction, Figure 5.26(c).



(a) Surface layer- Layer 20.

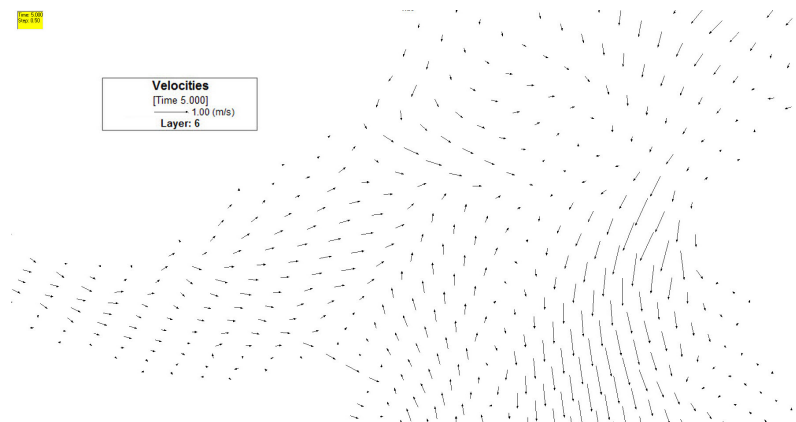
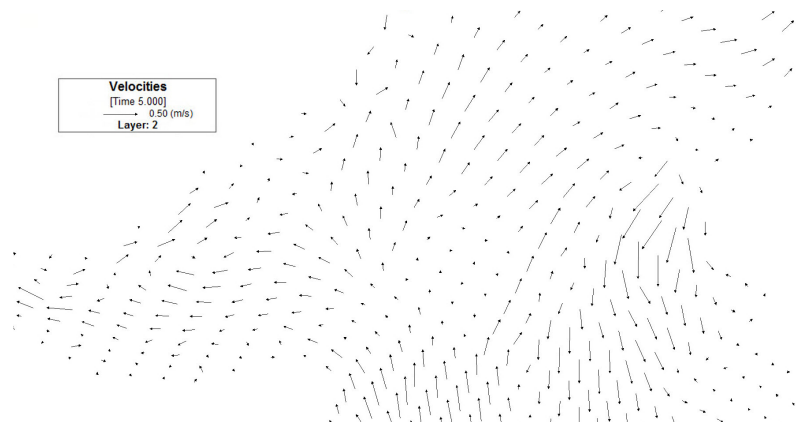
(b) Interface layer- Layer 6($\sim -28m$).(c) Lower layer- Layer 2($\sim -36m$).

Figure 5.26. Layer-wise velocity vectors at junction of GH for Test Run C.

5.4.2. Flow Dynamics of the Junction of Golden Horn

The Golden Horn estuary hydrodynamic is dependant on SOI; therefore, it is more important to correlate the SOI surface current conditions to the GH surface hydrodynamic. By this means, the GH variation to the SOI hydrodynamic condition can be obtained by studying the main strait flow properties. Reynolds number at Junction is utilized to find the dependency of surface water to the velocity intensity of the main strait. The surface velocity at Cell(42,48) which is in the middle of the cross-section is considered as velocity parameter in Reynolds number (Figure 5.27).



Figure 5.27. Sketch of cross-section used for calculation of the Reynolds No.

According to the test run results, the behavior of surface currents can be distinguished by correlating the main strait surface velocity to the net flow and water level difference between two ends of strait. The Reynolds number is the ratio of inertia force over viscous effect as follow,

$$\text{Re} = \frac{\textit{inertia forces}}{\textit{viscous forces}} = \frac{\rho v L}{\mu} = \frac{v L}{\nu} \quad (5.1)$$

where

$$\nu = \frac{\mu}{\rho} \text{ m}^2/\text{s}, \text{ (S.W. Kinematic viscosity)}$$

$$\mu = 0.00123 \text{ N.s/m}^2, \text{ (S.W. Dynamic viscosity)}$$

$$\rho = 1030 \text{ kg/m}^3, \text{ (S.W. Density)}$$

$$L = 1600 \text{ m}$$

By using calculated Reynolds number for the test runs which are set based on measurement flow data, shown in Table 5.3, the surface current condition at entrance of Golden Horn estuary are categorized into four types.

Table 5.3. Hydrodynamic properties of the SOI and Golden Horn junction.

Description for Strait of Istanbul Hydrodynamic Modeling by EFDC_Explorer		Input Boundary Condition for Model (Southward “+” Northward “-”)			Blockage Condition (Predicted by Model)	Δh	Surface velocity at Cell (42,48)	Reynolds Number	Current Condition at Entrance of Golden Horn
Test Case	Date Source	Q_U	Q_L	Q_{Net} ($Q_U - Q_L$)					
		m^3/s	m^3/s	m^3/s		cm	m/s	$\times 1e06$	
C	Altıok et al. (2014)	25,285	0	25,285	LLB	38	1.23	164.8	CW
R	Özsoy et al. (1995)	17,128	4,256	12,872	LLB	32	1.1	147.4	CW
K	Özsoy et al. (1995)	19,000	4,000	15,000	LLB	34	1.16	155.4	CW
L	Özsoy et al. (1995)	30,000	0	30,000	LLB	44	1.08	144.7	OUT
P	Özsoy et al. (1995)	32,000	0	32,000	LLB	49	1.06	142.0	OUT
A	IU-IMSM (2009)	13,195	7,360	5,835	Two-L	26	0.77	103.2	IN
D	Özsoy et al. (1996)	13,435	5,740	7,695	Two-L	26.3	0.84	112.5	IN
E	Özsoy et al. (1996)	8,287	8,287	0	Two-L	20	0.67	89.8	IN
H	Özsoy et al. (1996)	4,256	11,012	-6,756	ULB	6.4	0.21	28.1	IN
N	Özsoy et al. (1995)	4,000	9,500	-5,500	Two-L	9.7	0.35	46.9	IN
Q	Özsoy et al. (1996)	10,030	7,382	2,648	Two-L	20.5	0.69	92.4	IN
Z	Özsoy et al. (1996)	6,923	9,139	-2,216	Two-L	16	0.54	72.35	IN
B	Altıok et al. (2014)	6,015	23,846	-17,831	ULB	-9.5	-0.53	-71.0	CCW
M	Özsoy et al. (1995)	4,000	15,000	-11,000	ULB	2.7	-0.15	-20.1	CCW

For the southward surface flow, according to the flow intensity on the surface, three scenarios can occur; Water can inflow or outflow from GH in addition to CW eddy creation due to flow separation by the collision of currents to the Sarayburnu. Regarding the northward surface flow scenarios, the CCW eddies are created at the junction.

As it is categorized in Table 5.3, when the Reynolds number magnitude (representative for the velocity of the Cell(42,48) velocity) exceeds from 145×10^6 the high-intensity flow generates CW eddies at GH junction entrance. For the Reynolds number ranged between 0 and 125×10^6 the calmer current has the chance to penetrate the GH with no eddy creation at the junction. There is transition status between CW created eddies and inflow conditions which flows out the surface water of GH towards the main street. This scenario occurs for the Reynolds number between 125×10^6 and 145×10^6 , approximately.

Note. Reynolds number less than zero represents that the velocity vector in main strait is northward.

$Re < 0$	<i>CCW Eddies</i>
$0 < Re < +125 \times 10^6$	<i>Inflow</i>
$+125 \times 10^6 < Re < +145 \times 10^6$	<i>Outflow</i>
$+145 \times 10^6 < Re$	<i>CW Eddies</i>

(5.2)

The Reynolds No. can be compared to the existing net flow at strait to allocate relation between the flow condition to the surface current behavior at junction of GH and SOI. The Figure 5.28 suggests that for the below-mentioned net flow (in m^3/s unit) conditions how surface water behaves at the junction.

$$\begin{aligned}
 Q_{Net} < -10000 & \quad CCW \text{ Eddies} \\
 -10000 < Q_{Net} < +10000 & \quad In \text{ flow} \\
 +10000 < Q_{Net} < +28000 & \quad CW \text{ Eddies} \\
 +28000 < Q_{Net} & \quad Out \text{ flow}
 \end{aligned}$$

(5.3)

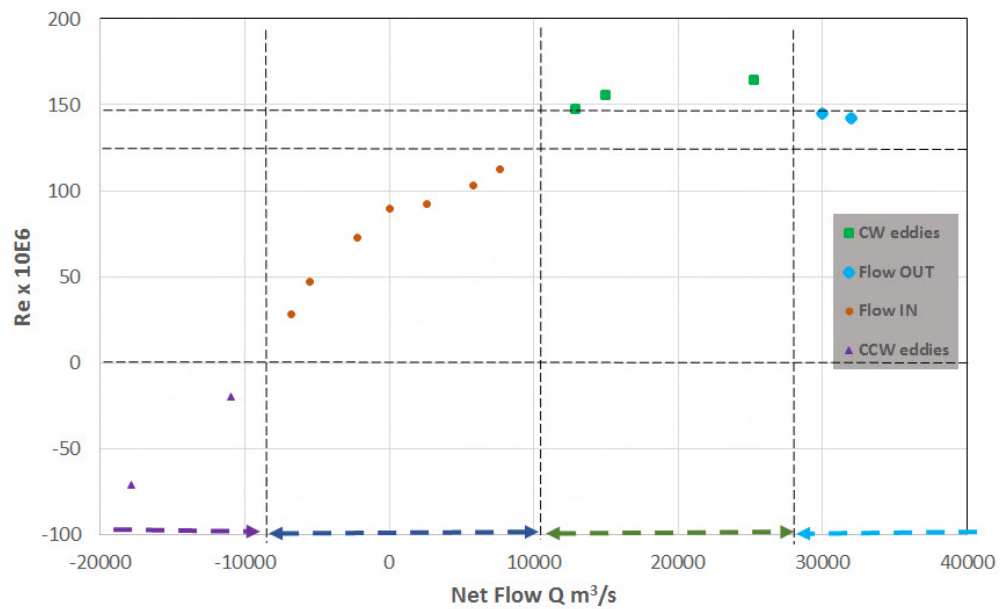


Figure 5.28. Surface water Reynolds number versus Q_{Net} plot.

The same Reynolds No. criterion are applicable to be compared versus WLD which is the easiest parameter to be obtained quickly in the SOI. Therefore, by measuring the WLD the current behavior at junction can be evaluated. The WLD (in cm) can predict the junction currents as follows,

$$\begin{aligned}
 \Delta h < +05 & \quad CCW \text{ Eddies} \\
 +05 < \Delta h < +28 & \quad \text{Inflow} \\
 +28 < \Delta h < +41 & \quad CW \text{ Eddies} \\
 +41 < \Delta h & \quad \text{Outflow}
 \end{aligned}$$

(5.4)

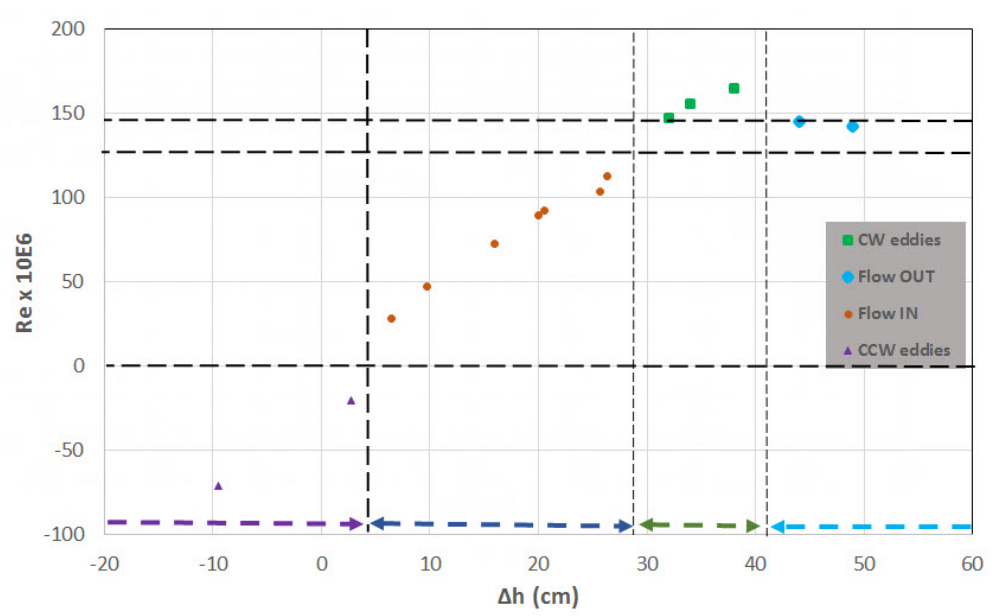


Figure 5.29. Surface water Reynolds number versus WLD plot

6. CONTAMINATION TRANSPORT MODELING AND RESULTS

6.1. Contaminant Transport Theory

6.1.1. Governing Equation

The EFDC model uses 3D advection-diffusion equation for contaminant transport modeling, Eq. 6.1,

$$\frac{\partial c}{\partial t} + \nabla(\vec{V}c) = \frac{\partial}{\partial x} \left(D_H \frac{\partial c}{\partial x} \right) + \frac{\partial}{\partial y} \left(D_H \frac{\partial c}{\partial y} \right) + \frac{\partial}{\partial z} \left(D_V \frac{\partial c}{\partial z} \right) - k_{RC}c + Q_C \quad (6.1)$$

where c is concentration, \vec{V} is flow velocity, (x, y, z) as Lagrangian coordinate of a particle, D_H & D_V the horizontal and vertical molecular diffusion coefficients of oil, k_{RC} is the first-order reaction and Q_c is source/sink term in the equation [32]. The first order biodegradation value is considered as 0.07.

In addition to Eq. 6.1, the 3D random walk approach introduced by Dunsbergen et al. [33] is being used for the Lagrangian particle tracking to study the flow particle circulations throughout the test line follow,

$$dx = dx_{drift} + dx_{ran} = \left(u + \frac{\partial D_H}{\partial x} \right) dt + \sqrt{2D_H dt} (2p - 1) \quad (6.2a)$$

$$dy = dy_{drift} + dy_{ran} = \left(v + \frac{\partial D_H}{\partial y} \right) dt + \sqrt{2D_H dt} (2p - 1) \quad (6.2b)$$

$$dz = dz_{drift} + dz_{ran} = \left(w + \frac{\partial D_V}{\partial z} \right) dt + \sqrt{2D_V dt} (2p - 1) \quad (6.2c)$$

where, p is uniformly distribution of random variables which have 0.5 mean value, therefore, $2p - 1$ value creates the values with range of -1 to 1 with mean of *zero*. In this study the random walk option is set to zero value.

6.1.2. Initial Condition and Transient Forcing

According to total five days hydrodynamic runtime, due to hydraulic stabilization of domain, the oil spillage event is simulated for three days. The initial concentration of oil is zero. As the source of oil concentration (Q_c), the oil releasing is distributed in 12 hours period which starts from the third day. The constant value of $1 \text{ m}^3/\text{s}$ is considered for both the horizontal and vertical diffusion coefficients during the modeling. In addition to oil transport, 2,000 number of drifters are considered to track flow particle transport which can illustrate the vertical and horizontal circulation of water particles.

6.2. Oil Spill Scenarios

The aim is to model the fate of oil contamination at Golden Horn due to ship accident and to track particle traveling route by 3D LPT. The oil spill test runs are run upon the hydrodynamic models discussed in Chapter 5. Therefore, according to Figure 6.1, spillage locations (SL) are established based past accidents information stated in Section 2.2.1 and one more risky area is selected at the junction of the GH. Hence, for mid-strait point (SL.1), for the GH junction, the Gotia accident oil spill characteristics details (SL.2), and for the Marmara Sea entrance (southern boundary) spillage (SL.3), Independenta accident details are used in oil spill model. For the 14 number of test runs in which the boundary conditions are based on measurement data (shown in Table 5.1 for Test Runs *A* to *Z* in presented order).

18,000 tons of oil concentration is being released in middle of strait (SL.1) in front of Emirgan and GH junction (SL.2), and the SL.3 oil spill represents the accident occurred in the southern boundary of the strait (SL.3) with a quantity of 64,000 tons of spillage.



Figure 6.1. Accident location map of used oil spill scenarios.

6.3. Results

The test run results in present appropriate behavior between the fate of oil spill and groups of flow test run cases. According to hydrodynamic structure of the main strait, the fate of spillage is studied to understand which condition can lead the spillage towards the Golden Horn estuary. According to the southward upper layer flow properties, the water can collide the Sarayburnu and shape CW currents at junction or inflow towards GH estuary, hence, the oil slicks of SL.1 and SL.2 accidents can be stirred to estuary by surface CW eddies. The oil contamination induced by accident at SL.3 can either be flushed northward without entering the GH or be stirred towards the estuary by CCW eddies at junction area. In addition, the vertical movement of water particles at southern region and estuary entrance generates the complicated behavior

of contaminant transport.

By categorizing the test runs shown in Table A.1, in regards to flow condition and surface layer direction at GH junction, five possible scenarios are predicted by model as shown in Table 6.1.

Table 6.1. Table of oil spill scenarios.

Oil Spill Scenario	Flow Condition (Predicted by Model)	Surface Current Condition at GH Entrance	Hydrodynamic Test Runs
I	Two-layer Flow	Inflow to GH	A, D, E, N, Q, Z
II	LLB	CW	C, K, R
III	LLB	Outflow from GH	P, L
IV	ULB	CCW	B, M
V	ULB	Inflow to GH	H

The LPT method provided good results regarding the vertical and horizontal circulations of water particles in the case of different flow and spillage conditions. Additionally regarding the concentration, the model can visualize the oil thickness and vertical integrated concentration magnitude.

Table 6.2 describe the comprehensive information regarding the hydrodynamic test runs and the corresponding fate of oil spill. According to the table, by sorting the test runs in respect to water level differences, for the Δh values between 2 *cm* to 35 *cm* the Golden Horn estuary will be contaminated by oil spill SL.1 and SL.2 accidents. In the case of SL.3 accident the ULB condition which carries a thin layer of southward calm currents penetrates the contamination towards the Golden Horn. Additionally, if the high density suspended oil slicks get trapped by vertical flow motions, they can reach the estuary by northward lower layer flows.

Table 6.2. Description table of oil spill. In this table: C: Contamination has entered to GH; N/C: No contamination has entered to GH.

Test Run	Hydrodynamic Characteristics							Oil Spill Scenario	Fate of Oil Spill Scenarios on Golden Horn Estuary		
	Q_U	Q_L	Q_{Net}	Δh	Surface Velocity at Cell (42,48)	Flow Condition	Surface Current Condition at Junction		Mid-strait (SL.1)	GH Junction (SL.2)	South Entrance (SL.3)
	m^3/s	m^3/s	m^3/s	cm	cm/s				18,000 tons	18,000 tons	64,000 tons
A	13,195	7,360	5,836	25.7	0.77	Two-layer	Inflow to GH	I	C	C	N/C
D	13,435	5,740	7,695	26.3	0.84	Two-layer	Inflow to GH	I	C	C	N/C
E	8,287	8,287	0	20	0.67	Two-layer	Inflow to GH	I	C	C	N/C
N	4,000	9,500	-5,500	9.7	0.35	Two-layer	Inflow to GH	I	C	C	N/C
Q	10,030	7,382	2,648	20.5	0.69	Two-layer	Inflow to GH	I	C	C	N/C
Z	6,923	9,139	-2,216	16	0.54	Two-layer	Inflow to GH	I	C	C	N/C
C	25,285	0	25,285	38	1.23	LLB	CW	II	N/C	N/C	N/C
K	19,000	4,000	15,000	34	1.16	LLB	CW	II	C	C	N/C
R	17,128	4,256	12,872	32	1.1	LLB	CW	II	C	C	N/C
L	30,000	0	30,000	44	1.08	LLB	Outflow from GH	III	N/C	N/C	N/C
P	32,000	0	32,000	49	1.06	LLB	Outflow from GH	III	N/C	N/C	N/C
M	4,000	15,000	-11,000	2.7	-0.15	ULB	CCW	IV	N/C	C	C
B	6,015	23,846	-17,831	-9.5	-0.53	ULB	CCW	IV	N/C	N/C	N/C
H	4,256	11,012	-6,756	6.4	0.21	ULB	Inflow to GH	V	C	C	N/C

6.3.1. Oil Spill Scenario (I)

This scenario represents the Two-layer flow models and inflowing surface currents to GH condition. In all of the including test runs (A, D, E, N, Q and Z), for both SL.1 and SL.2 the contamination penetrates to GH. Due to southward upper layer flow, the SL.3 accident has no influence on the strait and estuary.

Test Run A as a Two-layer flow condition, the contamination spreads out southward after the accident and contaminate lower half of strait including GH (Figure 6.2).

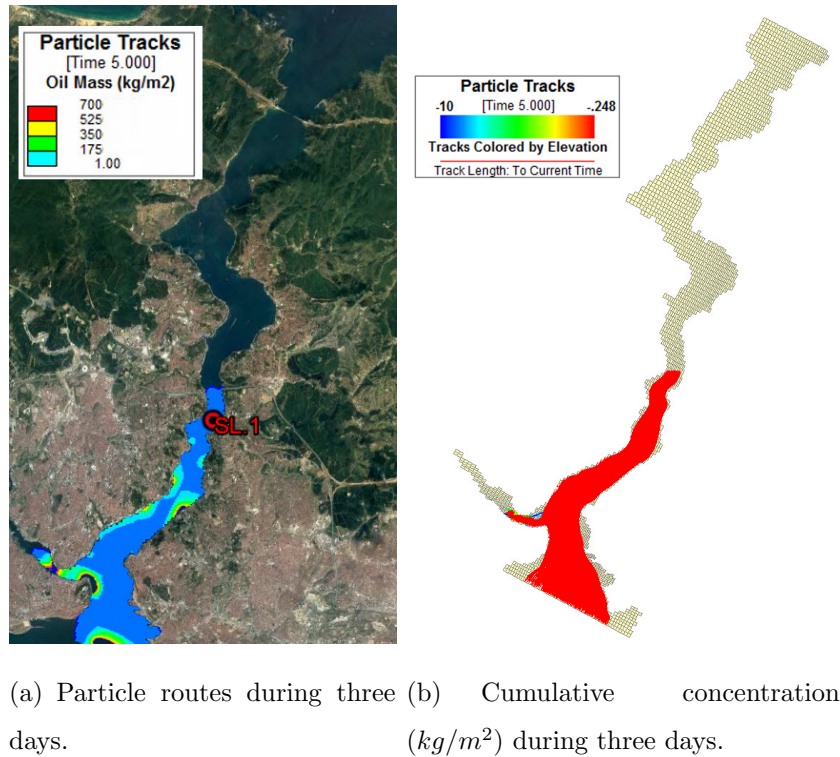


Figure 6.2. Fate of SL.1 accident on Scenario(I), Test Run A.

Considering the average surface current speed of 0.80 m/s the main strait, oil particles reach southern boundary in 3.5 hours. Particles enter the GH after 5.5 hours and reach the maximum concentration of $\sim 20,000 \text{ (kg/m}^2\text{)}$ under the Halic Bridge 24 hours after accident. One day after the spillage, the vertical circulation at Golden Horn transport the particle outwards by exiting interface layer currents, meanwhile,

the oil spill concentration reaches the maximum value of $\sim 5,000$ (kg/m^2) after 72 hours (Figures 6.3 and 6.4).

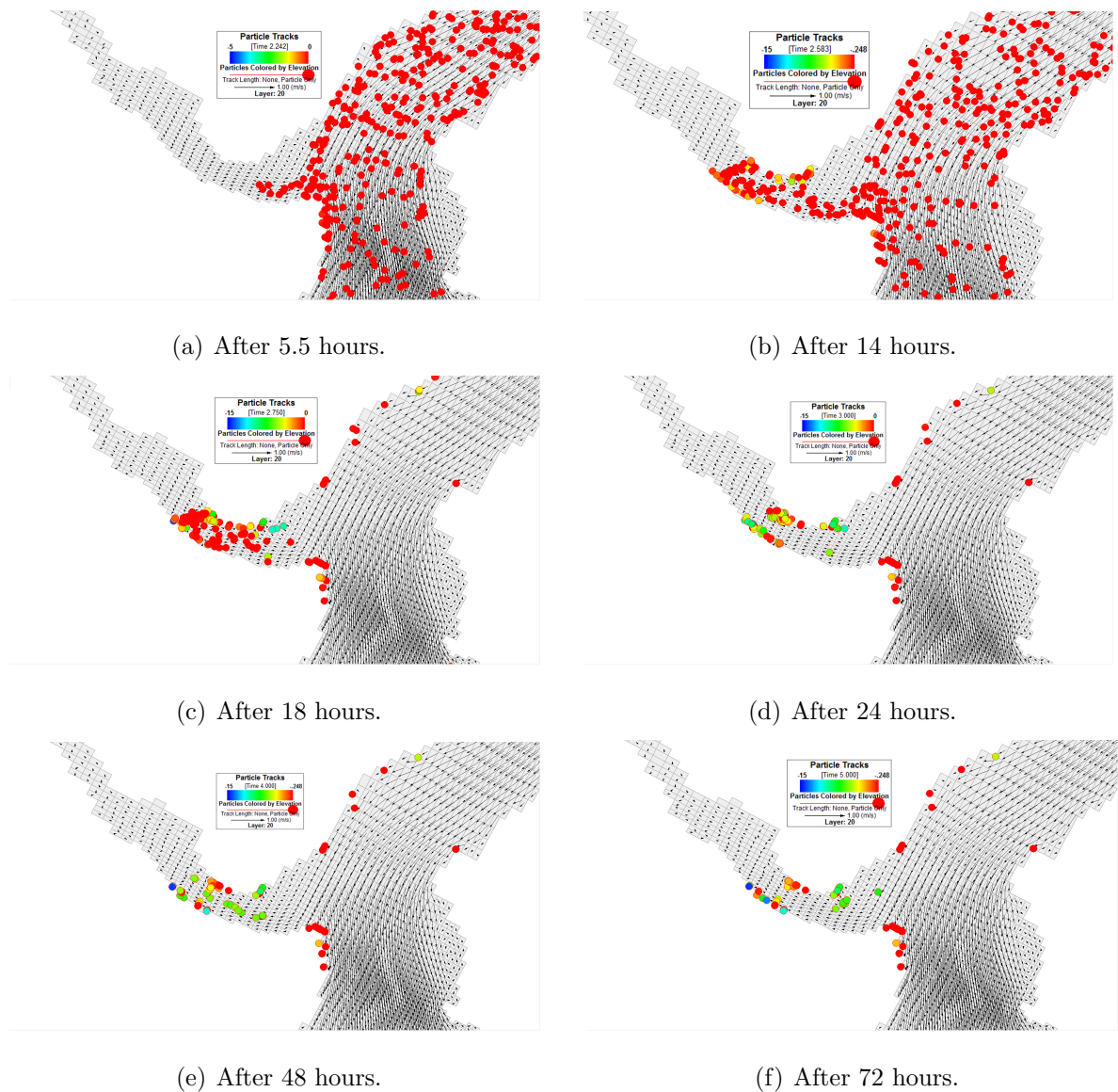
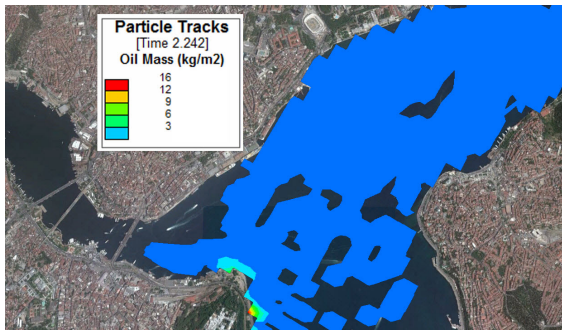
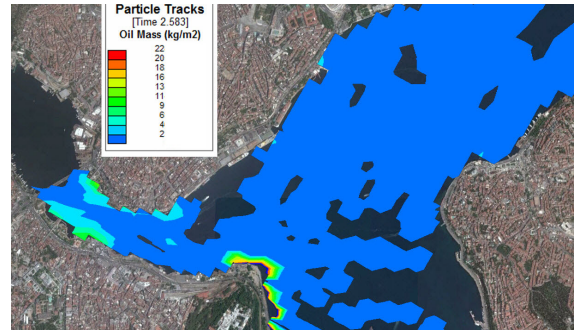


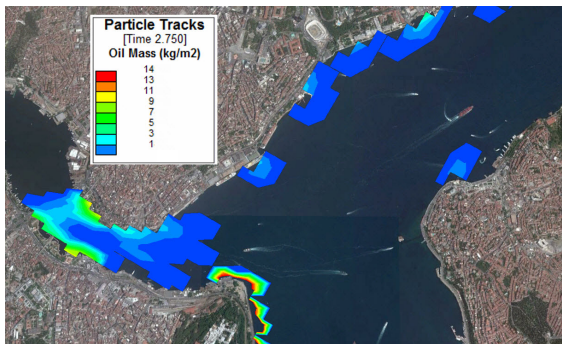
Figure 6.3. Particles location of SL.1 accident on Scenario(I), Test Run A.



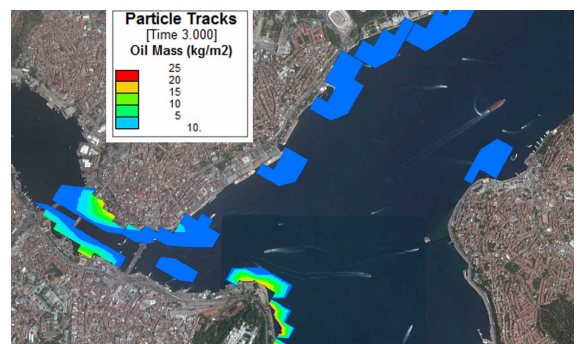
(a) After 5.5 hours.



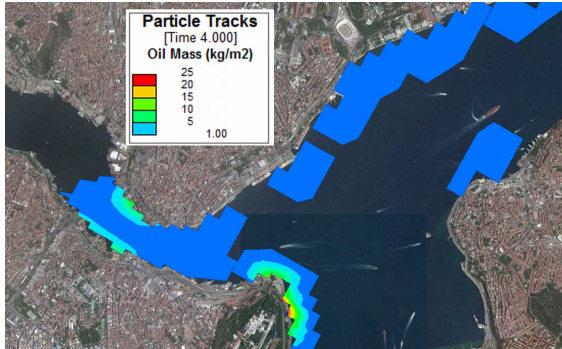
(b) After 14 hours.



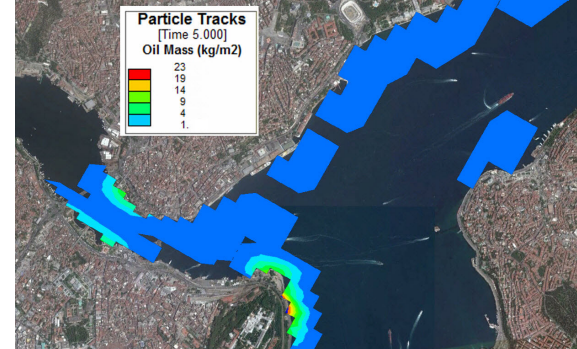
(c) After 18 hours.



(d) After 24 hours.



(e) After 48 hours.



(f) After 72 hours.

Figure 6.4. Oil concentration(kg/m^2) of SL.1 accident on Scenario(I), Test Run A.

The results of other test runs for Scenario(I) accidents at Golden Horn junction (SL.2) are presented in Appendix D.1.

6.3.2. Oil Spill Scenario (II)

This scenario represents the LLB flow hydrodynamic model and CW surface eddy currents at GH junction (Test Run C, R and K). According to Figure 6.5, the Golden Horn estuary is contaminated by SL.1 and SL.2 accidents in Test Runs R and K unlike for Test Run C.

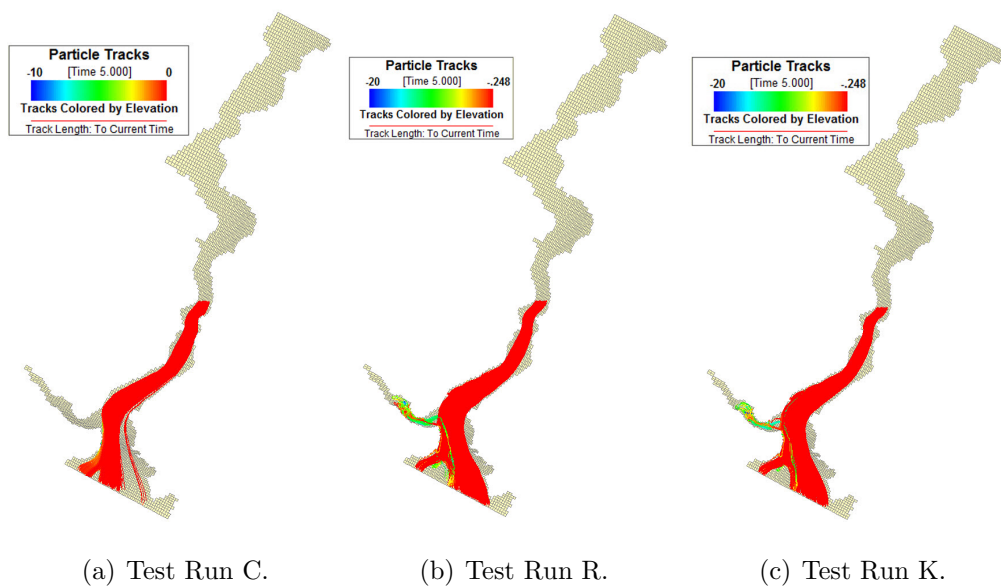


Figure 6.5. Particle Routes of SL.1 accident on Scenario(II) during three days.

The oil particles in Test Run C reach to the southern boundary of the strait in less than three hours and complete leave the strait in less than 16 hours (Figure D.9). On the contrary, in Test Run K and R, the Golden Horn receives the contamination eight hours after spillage, approximately. The CW eddies at junction prevent oil slicks to penetrate to the estuary on the surface, Hence, the concentration in the northern coast of the junction is considerably high during the oil spill scenario. The oil spill concentration in Golden horn reaches the maximum value of $\sim 2,000$ (kg/m^2) after two days and start decreasing (Figure D.11).

The released particles are being transported to GH by being trapped to lower layer flows due to vertical flow transport between layers and mostly leave by lower

layers flow southward the strait (Figure D.10).

The discrepancy in behavior of test runs in Scenario(II) in the case of entering to Golden Horn can be explained by correlation between discussed Reynolds number in Section 5.4.2 versus water level difference and net flow rate properties of the flow. If the corresponding local Reynolds number is larger than $+145 \times 10^6$ (i.e. Test Run C) the contamination never reaches the Golden Horn.

6.3.3. Oil Spill Scenario (III)

This scenario represents oil spill of LLB flow models and outflow from GH junction condition. There is no flow which directs the contamination towards the Golden Horn (Figure 6.6). The SL.1 and SL.2 accident's oil spill is being pushed towards the main strait and reach to the South boundary in two hours, therefore, Golden Horn is not jeopardized by oil spill scenario(III). The concentration plots at GH junction area is shown in Appendix D.

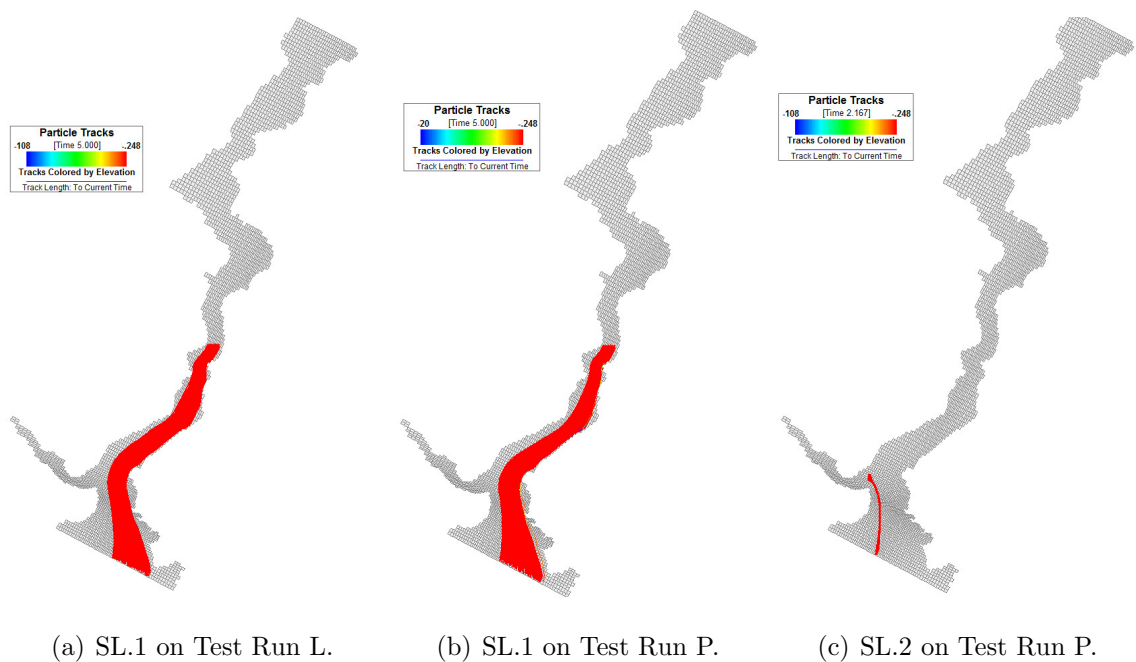
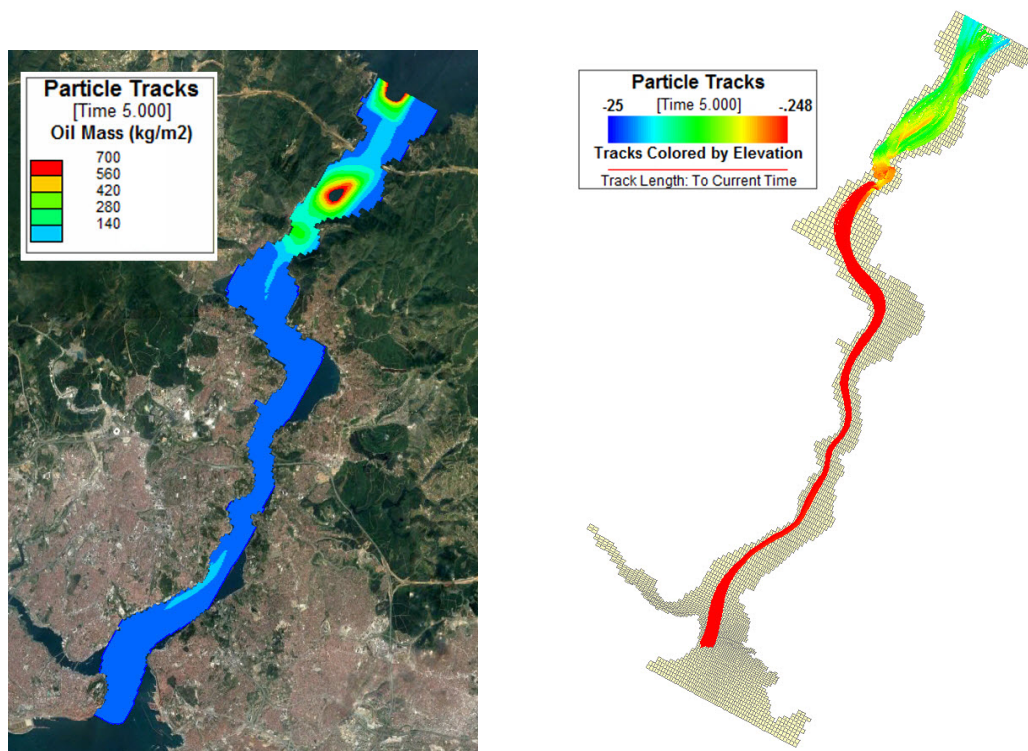


Figure 6.6. Particle Routes of Scenario(III) in three days.

6.3.4. Oil Spill Scenario (IV)

This scenarios represents oil spill of ULB flow and CCW eddies at GH junction conditions. In the ULB flow cases, the northward lower layer flow blocks the upper southward flow layer; therefore, the southward upper Black Sea waters do not have the chance to reach the Golden Horn (Test Run B). Hence, SL.3 accidents, which occurs at southern boundary, can be influencing the Golden Horn. In test Run B despite northward surface current at main strait and CCW eddies at junction, due to the velocity direction and small magnitude, the contamination do not get trapped by eddies to be stirred towards the estuary (Figure 6.7). While in Test Run M, int he case of SL.2 and SL.3 contamination penetrate to estuary. Therefore, for the strong northward upper layer flows, if the main strait velocity at middle point in front of junction exceeds $\sim 0.15 \text{ m/s}$, the stronger flow cannot direct the oil spill towards the GH (Test Run B).



(a) Total concentration(kg/m^2) during three days.

(b) Total contaminated area during three days.

Figure 6.7. Fate of SL.3 accident on Scenario(IV), Test Run B.

On the contrary, in Test Run M the complex current condition due for large CCW eddies and vertical circulation of water particles at the main strait, the particles are trapped by the eddy currents. This model reaches to stabilization in 30 hours; then after 3 hours circulating of contamination in the main eddy, the currents lead the SL.3 accident contamination to enter the Golden Horn. The oil spills proceed northwards inside the GH as of the end of simulation Figure D.15.

The interesting properties of this test run are that, the trapped tracing particles in the Golden Horn estuary circulates at surface until they get trapped by vertical circulation under the Galata Bridge and be flushed out northwards by interface layer, Figure D.14.

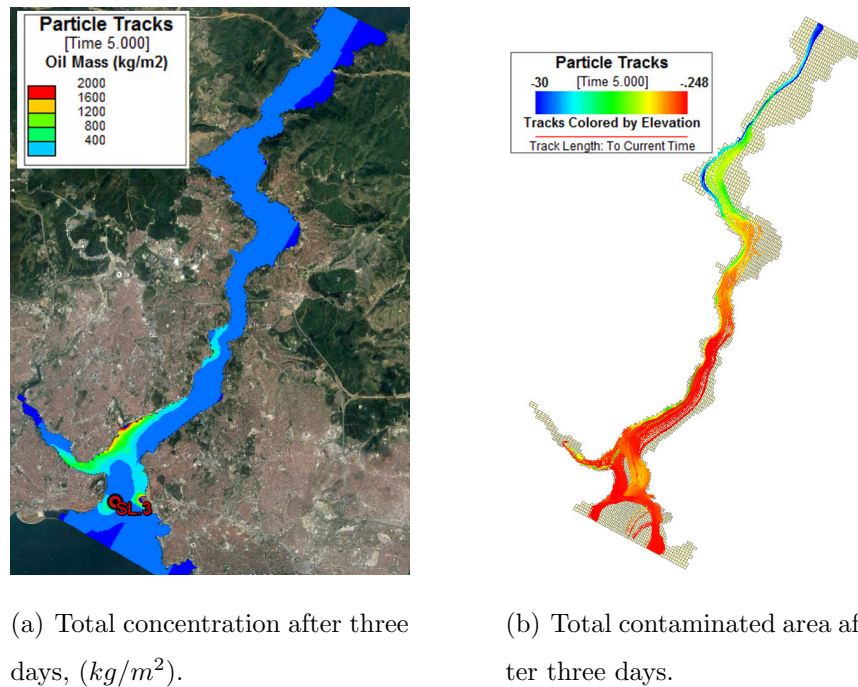


Figure 6.8. Fate of SL.3 accident on Scenario(IV), Test Run M.

the concentration of this oil spill scenario has the peak values of $25,000 \text{ kg/m}^2$ after 35 hours of accident near Galata Bridge and value of $11,000 \text{ kg/m}^2$ after 72 hours at the lower coasts of northern Golden Horn. The concentration at the main strait leaves the large eddy after 36 hours and in parallel the Golden Horn oil spill concentration starts to leave the estuary by the northward currents in front Beşiktaş

coast (Figure D.15).

Note. The further plots regarding concentration of oil spill and particle tracking are provided in Appendix D.3.

6.3.5. Oil Spill Scenario (V)

This scenarios represents oil spill of ULB flow and inflow towards the GH estuary conditions. Unlike the ULB test runs discussed in Oil Spill Scenario(IV) in some cases, a very thin layer of Black Sea fresh water can flow towards GH and southern boundary of SOI (Test Run H). In this case, this will act as a very weak two-layer flow body same as Scenario(I). Therefore, the accidents of SL.1 and SL.2 direct the contamination towards the Golden Horn estuary, Figure D.18.

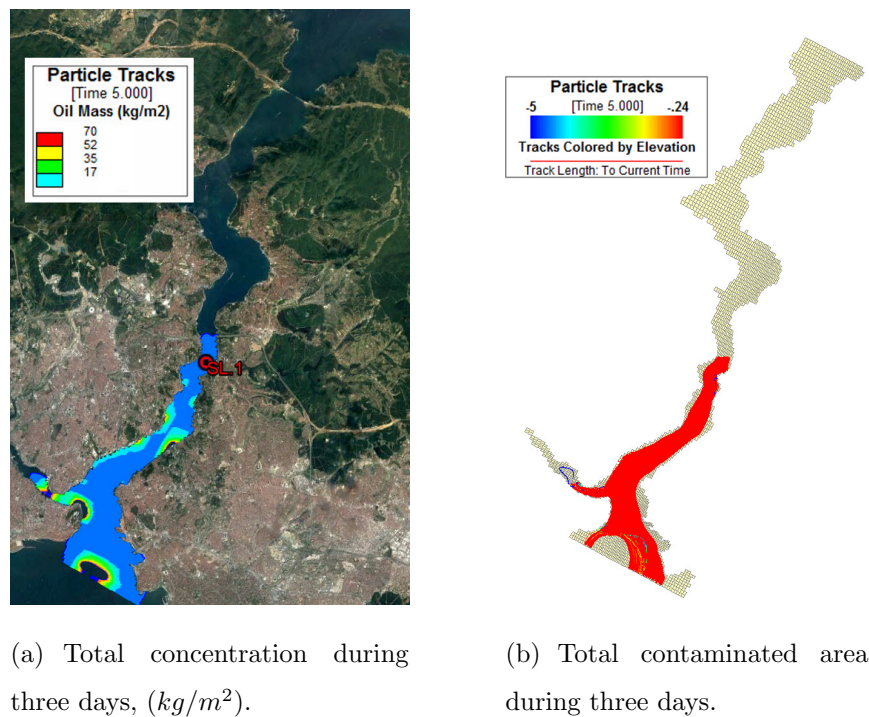


Figure 6.9. Fate of SL.1 accident on Scenario(V), Test Run H.

The calm southward upper flow transports the oil particles towards the southern boundary and Golden Horn in 9 and 12 hours, respectively. The main strait flushes out the particles 28 hours after the accident occurrence while the oil particles inside

the Golden Horn get stuck due to inflow currents. The maximum oil concentration of $25,000 \text{ kg/m}^3$ is recorded at lower coast after the Halic Bridge in 26^{th} hours. Although the contamination moves towards northern regions of Golden Horn, the concentration decreases after 72 hours (Figure D.19). The quite calm horizontal eddies circulate the particle in the estuary until they transport out towards South boundary of SOI by sticking to vertical eddies (figures on Appendix D.4).

7. CONCLUSION

The flow structure of the Strait of Istanbul (SOI) depends on the short-term and seasonal variations of sea level, dominant winds and barometric pressure in the adjacent seas. The sea level and the barometric pressure in the Black Sea control the fresh water inflow into the SOI at the North boundary. The water level in the North boundary is governed by wind setup and freshwater runoff into the Black Sea. The Danube River, which allocates majority of the inflow to the Black Sea, has the minimum flow rates between July and November and maximum between February and May. This fresh water flow affects the flow and sea level structure at the North boundary of the SOI with two months delay. Hence, due to the contribution of the predominant winds from the North and the freshwater inflow, the water level difference in SOI reaches its maximum value between July and August. On the other hand, in winter, the water level reaches its minimum value due to southerly winds [4, 12, 13, 34].

The predominantly two-layer flow structure in the SOI changes when strong winds from North or South cause Lower Layer Blockage (LLB) or Upper Layer Blockage (ULB), respectively. These special occurrences may last hours to a week. In response to an increase in velocity of the upper layer, the lower layers flow velocity increases which are valid for the small net flow values. As the net flow magnitude increases, the velocity of lower layer starts to decrease until the lower layer blockage event occurs. The lower layer blockage regularly is common during June and July in response to the corresponding increase in water level difference and freshwater discharge of Black Sea to the strait.

The test cases run with the present model predict that LLB occurs when water level difference (WLD) is larger than 32 cm and the net flow rate is larger than 13,000 m^3/s . On the other hand, ULB occurs when the WLD is smaller than +5 cm and the net flow rate is smaller than $-9,600 m^3/s$ (Northward). Meanwhile, temperature and salinity are high during blockage events due to limited mixing between fresher Black Sea and more saline Mediterranean waters. During two-layer flow, the Mediterranean

water inside the SOI is less saline than the outside. Hence, salinity and temperature are minimum in Feb-Mar and maximum in Jul-Sep. Overall, the SOI is sensitive to short-term variations induced by local parameters.

During two-layer flow conditions, the surface current enters the Golden Horn without surface eddies forming at the entrance. Occasionally when LLB occurs, the southerly upper layer velocity increases, the surface currents hit the Sarayburnu shore and induce large CW eddies. Thus, during the ship accidents in Two-layer flow case, the model predicted that the contamination flows into the Golden Horn. While for the LLB hydrodynamic scenarios, the CW eddies can stir the oil spills towards the estuary if the WLD value is smaller than 35 cm, For the larger WLD values, the CW eddies do not transport surface contamination to the estuary. According to the model results for ULB cases, as the Mediterranean water enters the strait from the deepest part of South boundary, which is located at left side, the intensity and direction of flow generate different size of CCW eddies by separating the flow further up the Beşiktaş coast. If oil spills occur at southern regions of the strait, oil particles get trapped by these eddies and the Golden Horn will be affected. In some cases, despite the ULB condition, a thin layer of fresh Black Sea freshwater will be generated southward. Which can act as the mild version of Two-layer flow case and lead the contamination to flow towards the estuary readily.

In addition to horizontal eddies, the vertical circulations in the SOI, especially at junction and inside of the Golden Horn, makes the hydrodynamics of area more complex. In accordance with the weathering, the denser contaminants may get trapped in the vertical circulation and transport in/out of the Golden Horn in the lower layers.

Considering all test scenarios, the model predicts that in the case of the oil spill, contamination may penetrate into the Golden Horn when WLD is between $\sim +2$ cm and $+35$ cm. For other values, the main stream in the SOI flushes the oil out through South or North boundaries. The present model predicts the fate and quantity of oil contamination in the Golden Horn by solving the hydrodynamics of the SOI. The summary of oil spill correlation to flow scenarios are presented in Table 7.1.

Table 7.1. C: Contamination has entered to GH; N/C: No contamination has entered to GH.

		Accident Location			
Oil Spill Scenario No.	Hydrodynamic Condition		<i>SL.1</i>	<i>SL.2</i>	<i>SL.3</i>
I	Two-layer	Inflow to GH	C	C	N/C
II	LLB	CW	C N/C	C N/C	N/C
III	LLB	Outflow from GH	N/C	N/C	N/C
IV	ULB	CCW	N/C	C N/C	C N/C
V	ULB	Inflow to GH	C	C	N/C

According to the test runs, results of SOI hydrodynamic and oil spill model by EFDC are in good agreement for the estimating turbulence hydrodynamic, multilayered opposite directional stratified flow to explore the interface layer properties and vertical mixing, more proper estimations for salinity, temperature and velocity in upper layers, oils pill and lagrangian particle tracking option, and water level difference estimation. On the contrary, for the predicting the vertical turbulence and mixing over the narrow and sharp changing bathymetry for the two layer flow of SOI, deviances in estimating the lower layer flow properties in the flow boundary, not modeling the interaction between water and oil's vertical buoyant motion, and depth averaged visualizing of the vertical concentration of contamination in vertical direction can be counted as disadvantages of model. Therefore as the future work, according to [31], by applying new version of code ,which uses Sigma-Z coordinate system in the vertical layers, best-matching vertical profiles for the salinity, temperature and velocity can be achieved.

REFERENCES

1. Tan, B. and E. Otay, “A stochastic model of vessel casualties resulting from oil tanker traffic through narrow waterways”, *Proceedings of the 12th European Simulation Multiconference on Simulation-Past, Present and Future*, pp. 881–885, 1999.
2. Alpar, B., H. Yüce and A. Türker, “Water exchange in the Golden Horn”, *Journal of Black Sea/Mediterranean Environment*, Vol. 9, No. 1, 2003.
3. Hamrick, J. M., “A three-dimensional environmental fluid dynamics computer code theoretical and computational aspects”, *Special Report, Virginia Institute of Marine Science*, p. 58, 1992.
4. Özsoy, E., M. Latif, S. Tugrul and U. Ünlüata, “Exchanges with the Mediterranean, fluxes and boundary mixing processes in the Black Sea”, *Mediterranean Tributary Seas, Bulletin de l’Institut Océanographique, Monaco, Special*, , No. 15, pp. 1–25, 1995.
5. Özsoy, E., M. A. Latif, H. Sur and Y. Goryachkin, “A review of the exchange flow regime and mixing in the Bosphorus strait”, *Bulletin-Institut Oceanographique Monaco-Numero Special*, pp. 187–204, 1996.
6. Altıok, H., A. Aslan, S. Övez, N. Demirel, A. Yüksek, N. Kıratlı, S. Taş, A. E. Müftüoğlu, H. I. Sur and E. Okuş, “Influence of the extreme conditions on the water quality and material exchange flux in the Strait of Istanbul”, *Journal of Marine Systems*, Vol. 139, pp. 204–216, 2014.
7. Oğuz, T., E. Özsoy, M. A. Latif, H. I. Sur and Ü. Ünlüata, “Modeling of hydraulically controlled exchange flow in the Bosphorus Strait”, *Journal of Physical Oceanography*, Vol. 20, No. 7, pp. 945–965, 1990.
8. Alpar, B., E. Doğan, H. Yüce, H. Altıok, A. Kurter and S. Kara, “Symptoms

- of a prominent Mediterranean layer blockage in the Strait of Istanbul (March 26-28, 1998) on the interactions of the Golden Horn Estuary”, *Journal of Black Sea/Mediterranean Environment*, Vol. 5, No. 2, 1999.
9. Ünlülata, Ü., T. Oğuz, M. Latif and E. Özsoy, “On the physical oceanography of the Turkish Straits”, *The physical oceanography of sea straits*, pp. 25–60, Springer, 1990.
 10. Doğan, E., H. Sarıkaya, . Öztürk, E. Gönenç, K. Güven, A. Kurter, H. Yüce, B. Alpar and E. Okuş, “Su kalitesi izleme çalışması sonuç raporu”, *Journal of Physical Oceanography*, 1998.
 11. Moller, L., “Alfred Merz hydrographische unter suchungen in Bosphorus and Dardanalten”, *Veroff. Insr. Meeresk, Berlin Uni., Neue Folge A*, Vol. 18, 1928.
 12. Andersen, S., F. Jakobsen, B. Alpar and D. Bilimleri, “The water level in the Bosphorus Strait and its dependence on atmospheric forcing”, *Deutsche Hydrografische Zeitschrift*, Vol. 49, No. 4, pp. 467–476, 1997.
 13. Maderich, V. and S. Konstantinov, “Seasonal dynamics of the system Sea-Strait: Black Sea–Bosphorus case study”, *Estuarine, Coastal and Shelf Science*, Vol. 55, No. 2, pp. 183–196, 2002.
 14. Otay, E., M. Aslani and U. Şensoy, “Emergency response plan of marine pollution for Galata Port - accident scenarios and computer modeling”, *Tech. Rep.(Turkish), Boğaziçi Uni.*, p. 73, 2014.
 15. Sözer, A., *Numerical modeling of the Bosphorus exchange flow dynamics*, Ph.D. thesis, Institute of Marine Sciences, Middle East Technical University, Erdemli, Mersin, Turkey, 2013.
 16. Sannino, G., A. Sözer and E. Özsoy, “A High-Resolution Modelling Study of the Turkish Straits System”, (*submitted for publication in Ocean Dynamics*), 2016.

17. Kornhauser, A. and W. Clark, "Quantitative forecast of vessel casualties resulting from additional oil tanker traffic through the Bosphorus", *Report, ALK Associates, Princeton, NJ*, 1995.
18. Otay, E. N. and S. Özkan, "Stochastic Prediction of Maritime Accidents in the strait of Istanbul", *Proceedings of the 3rd International Conference on Oil Spills in the Mediterranean and Black Sea regions*, pp. 92–104, 2003.
19. Doğan, E. and S. Burak, "Ship-originated pollution in the Istanbul Strait (Bosphorus) and Marmara Sea", *Journal of Coastal Research*, pp. 388–394, 2007.
20. Otay, E. and O. Yenigün, "An oil spill in the Bosphorus: The Gotia accident", *Proc. 3rd Intl. Conf. on Oil Spills in the Mediterranean and Black Sea Reg., Istanbul*, pp. 27–42, 2003.
21. Stewart, R. H., *Introduction to physical oceanography*, Citeseer, 2008.
22. Lewis, E. and R. Perkin, "The practical salinity scale 1978: conversion of existing data", *Deep Sea Research Part A. Oceanographic Research Papers*, Vol. 28, No. 4, pp. 307–328, 1981.
23. Farmer, D. and L. Armi, "Maximal two-layer exchange over a sill and through the combination of a sill and contraction with barotropic flow", *Journal of Fluid Mechanics*, Vol. 164, pp. 53–76, 1986.
24. Blumberg, A. F. and G. L. Mellor, "A description of a three-dimensional coastal ocean circulation model", *Three-dimensional coastal ocean models*, pp. 1–16, 1987.
25. Fofonoff, N. P., "Physical properties of seawater, in The Sea - edited by M. N. Hill", *Interscienc*, Vol. 1, pp. 3–30, 1962.
26. Smagorinsky, J., "General circulation experiments with the primitive equations: I. the basic experiment", *Monthly weather review*, Vol. 91, No. 3, pp. 99–164, 1963.

27. Mellor, G. L. and T. Yamada, “Development of a turbulence closure model for geophysical fluid problems”, *Reviews of Geophysics*, Vol. 20, No. 4, pp. 851–875, 1982.
28. Mellor, G. L., T. Ezer and L.-Y. Oey, “The pressure gradient conundrum of sigma coordinate ocean models”, *Journal of atmospheric and oceanic technology*, Vol. 11, No. 4, pp. 1126–1134, 1994.
29. Yüce, H., “On the variability of Mediterranean water flow into the Black Sea”, *Continental Shelf Research*, Vol. 16, No. 11, pp. 1399–1413, 1996.
30. Craig, O., “User’s manual for EFDC_Explorer v7.1: A pre/post processor for the environmental fluid dynamics code (Rev00)”, *Special Report, Dynamic Solutions International*, p. 58, 2013.
31. Craig, P., D. Chung, N. Lam, P. Son and N. Tinh, “Sigma-Zed: a computationally efficient approach to reduce the horizontal gradient error in the EFDC’s vertical Sigma grid”, *Proceedings of the 11th International Conference on Hydrodynamics (ICHHD 2014)*, 2014.
32. Chang, D. H. and P. Craig, “Implementation of a Lagrangian particle tracking sub-model for the environmental fluid dynamics Code”, *Dynamic Solution, LLC, Knoxville, TN and Hanoi Vietnam*, 2009.
33. Dunsbergen, D. and G. Stalling, “The combination of a random walk method and a hydrodynamic model for the simulation of dispersion of dissolved matter in water”, *WIT Transactions on Ecology and the Environment*, Vol. 2, 1970.
34. Gunnerson, C. G. and E. Ozturgut, “The Bosphorus”, *The Black Sea—geology, chemistry and biology. AAPG Bull*, Vol. 20, pp. 99–114, 1974.

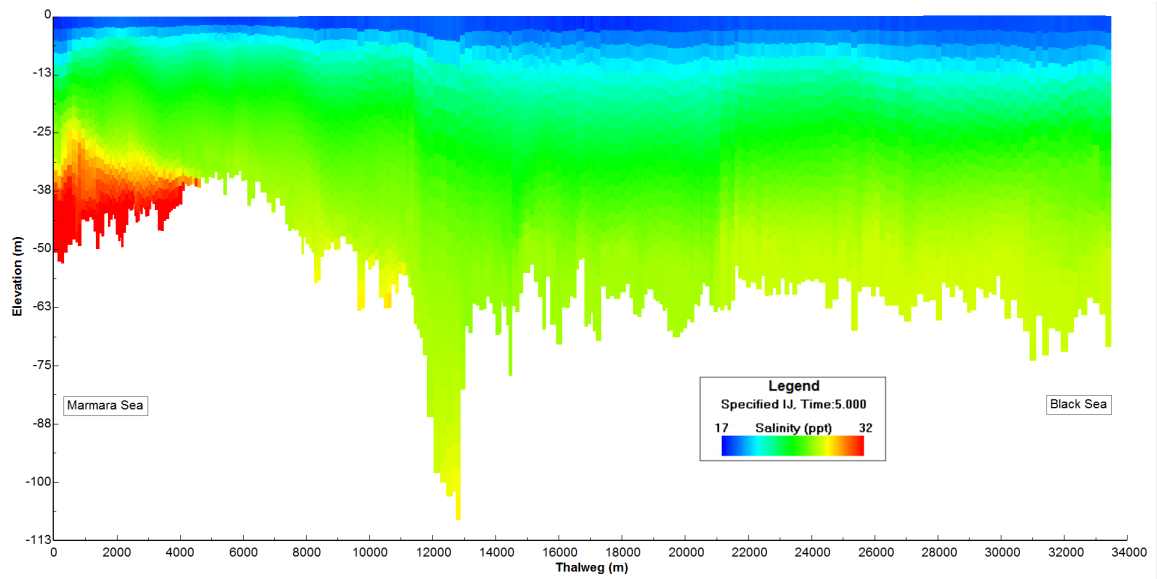
APPENDIX A: MODEL DESCRIPTION TABLE

The comprehensive table of Hydrodynamic (A.1) presents information about boundary condition parameters, hydrodynamic conditions and junction currents.

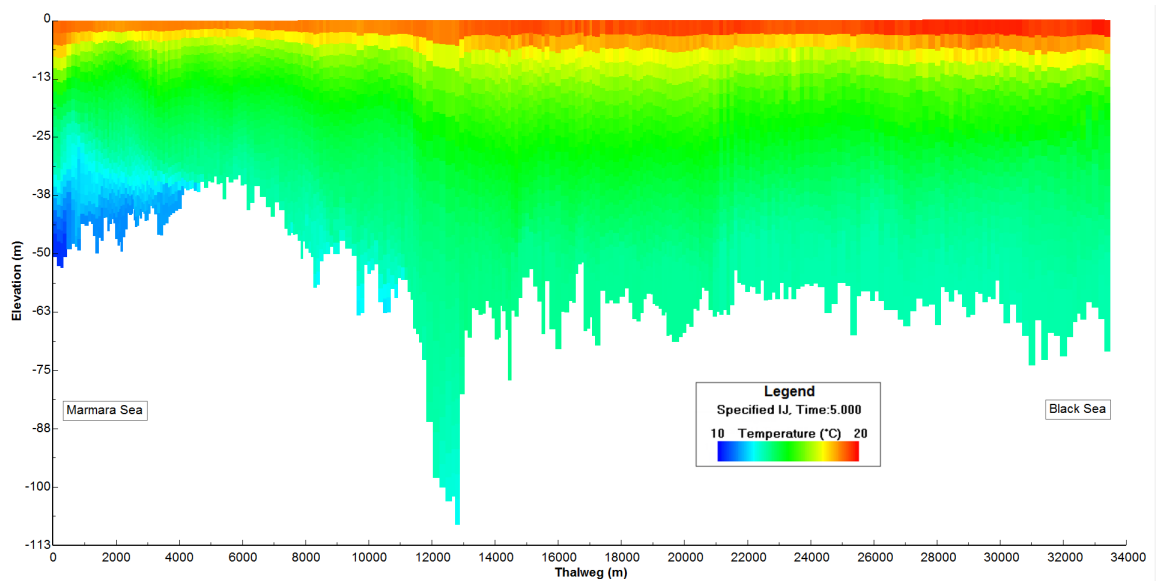
Table A.1. Hydrodynamic modeling description table for the SOI and GH.

Description for the Strait of Istanbul Hydrodynamic Modeling by EFDC_Explorer				Input Flow Boundary Condition for Model (Southward “+” Northward “-”)			Input Salinity Boundary Condition for Model (Upper-Lower)		Input Temperature Boundary Condition for Model (Upper-Lower)		Water Level Difference ($\Delta h =$ $h_{North} - h_{South}$)		Blockage Condition (Predicted by Model)	Surface Current Condition at Golden Horn Junction		
Test Case	Data Source	Type	Date	Q_U	Q_L	Q_{Net}	North Bound.	South Bound.	North Bound.	South Bound.	Pres. Model	Meas./ Comp.		Surf. Vel. at Cell (42,48)	Rey. No.	Dir.
				m^3/s	m^3/s	m^3/s	psu	psu	$^{\circ}C$	$^{\circ}C$	cm	cm		m/s	$\times 1e6$	
BU	Otay et al. (2015)	Meas.	23-Jun-15	21,000	-7,000	14,000	17.0-36.0	18.0-37.0	23-14	20-10	16	14	Two-L	-	-	-
A	IU-IMSM (2009)	Meas.	17-Feb-09	13,195	-7,360	5,835	17.2-36.8	20.6-38.6	7.1-14.9	8.2-15.2	26	35	Two-L	0.77	103.2	IN
B	Altıok et al. (2014)	Meas.	22-Oct-03	6,015	-23,846	-17,831	17.9-35.1	23.4-38.4	18.1-15.4	17.5-15.5	-9.5	-	ULB	-0.53	-71.0	CCW
C	Altıok et al. (2014)	Meas.	28-Feb-03	25,285	0	25,285	17.1-17.9	17.7-38.4	3.1-3.3	2.9-15.5	38	38.5	LLB	1.23	164.8	CW
D	Özsoy et al. (1996)	Meas.	N/A	13,435	-5,740	7,695	17.3-36.5	17.9-37.7	20.6-14.5	8.2-15.2	26.3	-	Two-L	0.84	112.5	IN
E	Özsoy et al. (1996)	Meas.	N/A	8,287	-8,287	0	17.7-36.3	19.3-38.0	13.7-15.2	13.8-15.3	20	-	Two-L	0.67	89.8	IN
H	Özsoy et al. (1996)	Meas.	N/A	4,256	-11,012	-6,756	17.9-35.1	23.4-38.4	18.1-15.4	17.5-15.5	6.4	-	ULB	0.21	28.1	IN
K	Özsoy et al. (1995)	Meas.	18-May-92	19,000	-4,000	15,000	17.7-36.3	17.9-37.9	13.7-15.2	13.8-15.3	34	-	LLB	1.16	155.4	CW
L	Özsoy et al. (1995)	Meas.	15-May-92	30,000	0	30,000	17.1-17.9	17.7-38.4	3.1-3.3	3.0-15.5	44	-	LLB	1.08	144.7	OUT
M	Özsoy et al. (1995)	Meas.	02-Sep-92	4,000	-15,000	-11,000	17.9-35.1	23.4-38.4	18.1-15.4	17.5-15.5	2.7	-	ULB	-0.15	-20.1	CCW
N	Özsoy et al. (1995)	Meas.	02-Oct-91	4,000	-9,500	-5,500	17.7-36.3	19.2-38.0	13.7-15.2	13.9-15.3	9.7	-	Two-L	0.35	46.9	IN
P	Özsoy et al. (1995)	Meas.	14-May-92	32,000	0	32,000	17.1-17.9	17.7-38.4	3.1-3.3	3.0-15.5	49	-	LLB	1.06	142.0	OUT
Q	Özsoy et al. (1996)	Meas.	N/A	10,030	-7,382	2,648	17.2-36.8	20.6-38.6	7.1-14.9	8.2-15.2	20.5	-	Two-L	0.69	92.4	IN
R	Özsoy et al. (1996)	Meas.	N/A	17,128	-4,256	12,872	17.7-36.3	17.9-38.0	13.7-15.2	13.9-15.3	32	-	LLB	1.1	147.4	CW
Z	Özsoy et al. (1996)	Meas.	N/A	6,923	-9,139	-2,216	17.7-36.3	19.2-37.9	13.7-15.2	13.9-15.3	16	-	Two-L	0.54	72.3	IN
O	Sannino et al. (2016) Sözer (2013)	Comp.	generic	9,950	-4,550	5,400	17.2-36.8	20.6-38.6	7.1-14.8	8.2-15.2	25	12.6 22	Two-L	-	-	-
U	Sannino et al. (2016) Sözer (2013)	Comp.	generic	19,200	1,200	18,000	17.7-36.3	17.9-38.0	13.7-15.2	13.8-15.3	36	24.6 34.6	LLB	-	-	-
V	Sannino et al. (2016)	Comp.	generic	50,000	0	50,000	17.5-17.9	17.5-38.4	23-7	23.5-15	88	91.1	LLB	-	-	-
W	Sannino et al. (2016) Sözer (2013)	Comp.	generic	6,950	-6,950	0	17.7-36.3	13.2-38.0	13.7-15.2	13.9-15.3	18.7	9 16.9	Two-L	-	-	-
X	Sannino et al. (2016) Sözer (2013)	Comp.	generic	13,000	-3,400	9,600	17.5-37	18-38.5	19-14.5	19-14.5	16.6	16.7 25.6	Two-L	-	-	-
Y	Sannino et al. (2016) Sözer (2013)	Comp.	generic	1,900	-11,500	-9,600	17.9-35.1	23.4-38.4	18.1-15.4	17.5-15.5	2.9	2.2 8.9	ULB	-	-	-

APPENDIX B: FIGURES OF TEST RUN BU

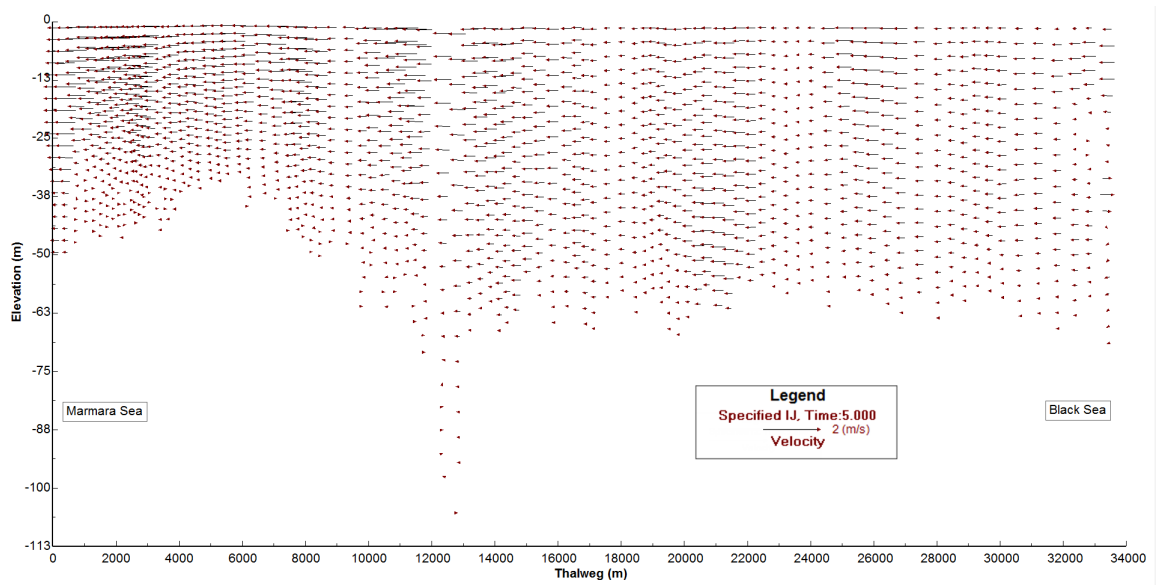


(a) Salinity profile.

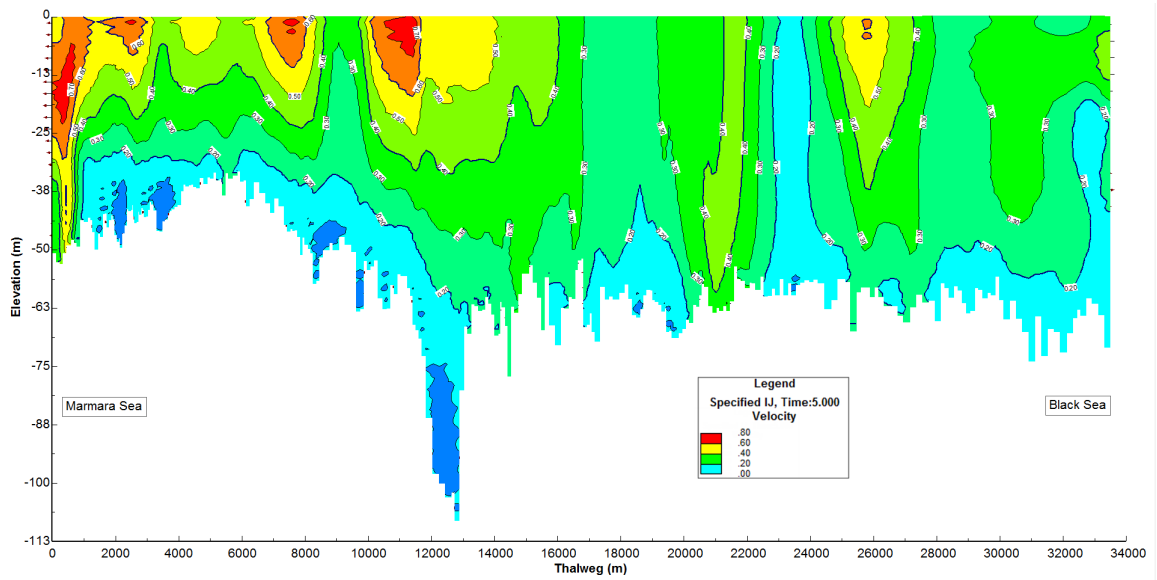


(b) Temperature profile.

Figure B.1. Thalweg line longitudinal-section profiles for Test Run BU.



(a) Velocity vectors.



(b) Velocity contour.

Figure B.2. Thalweg line longitudinal-section velocity profiles for Test Run BU.

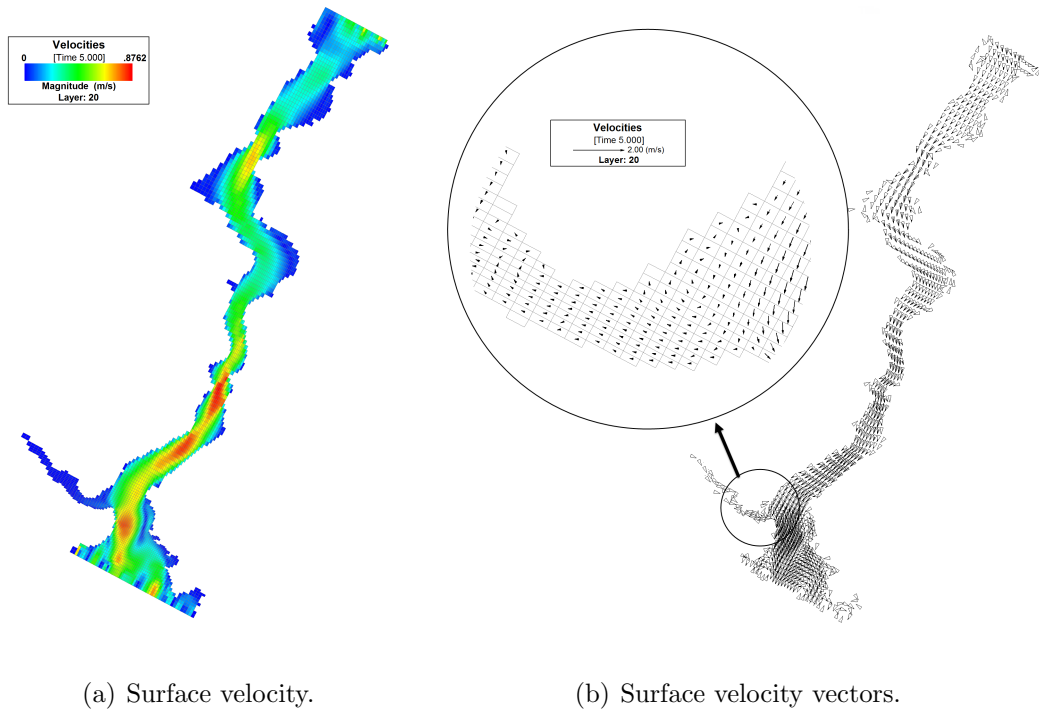


Figure B.3. Surface water velocity plots for Test Run BU.

APPENDIX C: FIGURES AND TABLES OF TEST RUN A,B,C

C.1. Stations

Table C.1. CTD stations coordinate for Test Run A.

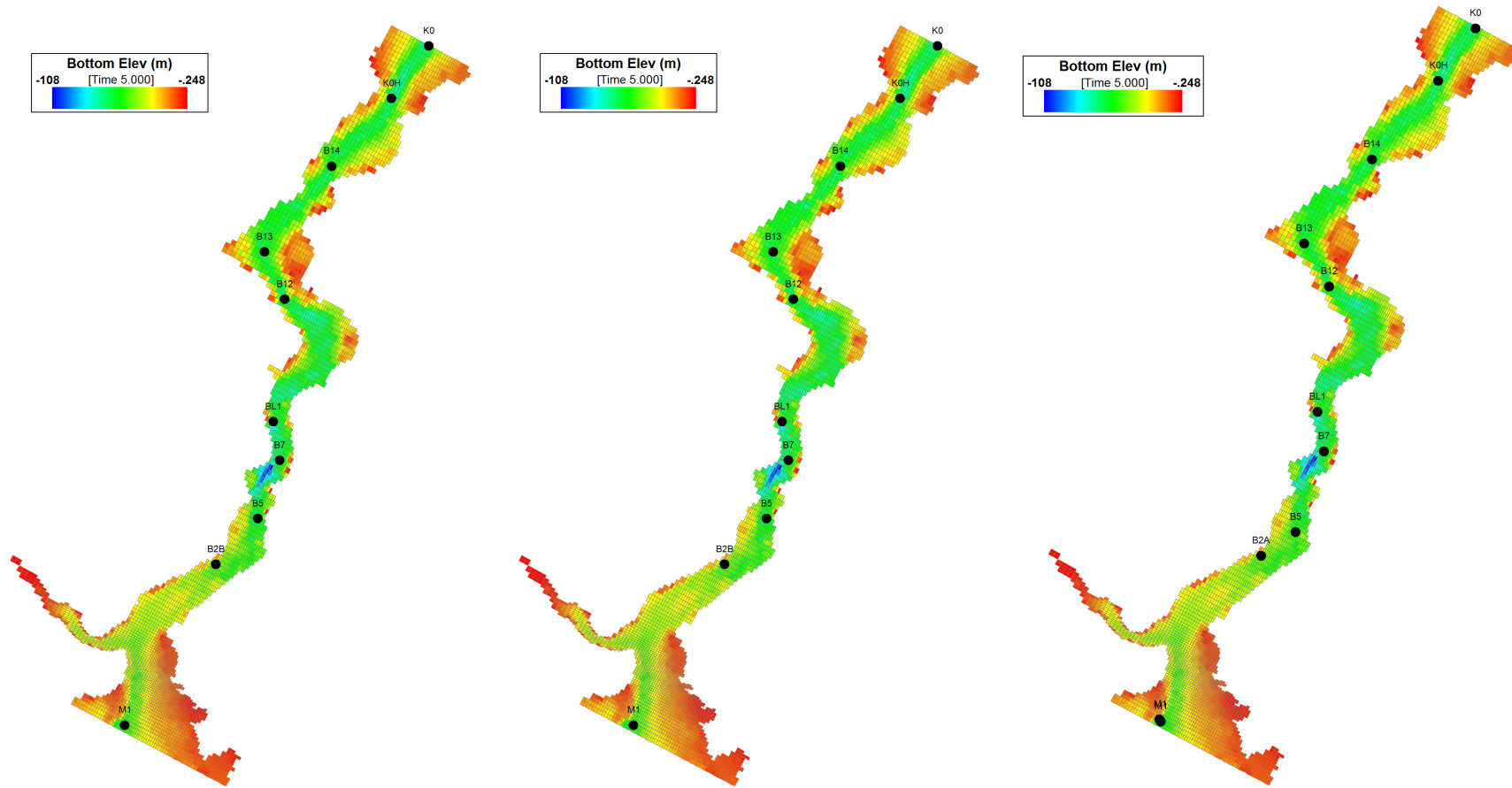
Station No	<i>x</i>	<i>y</i>
K0	678775.6	4565876.5
K0H	677371.1	4563892
B14	674960.8	4561096
B13	672413.9	4557920
B12	673239.8	4556122
B8	674460.1	4553208
BL1	672805.6	4551369.5
B7	673041.5	4549885
B6	672344.4	4548896.5
B5	672196	4547616.5
B2A	670680	4545931
B2B	670832	4545397
M1	666874.9	4539657

Table C.2. CTD stations UTM coordinate for Test Run B.

Station No	<i>x</i>	<i>y</i>
K0	678807.798	4565928.958
K0H	676819.365	4563536.437
B14	675199.186	4561131.158
B13	672454.639	4557944.288
B12	673318.631	4555854.136
BL1	672811.086	4551743.131
B7	673181.701	4549930.128
B5	672209.783	4547296.771
B2B	670633.937	4546004.693
M1	666826.472	4539630.111

Table C.3. CTD stations coordinate for Test Run C.

Station No	<i>x</i>	<i>y</i>
K0	678775.6	4565876.5
K0H	676530.194	4563351.687
B2A	670950.111	4545067.877
B5	670202.914	4545372.625
B7	671689.472	4546895.775
BL1	672811.527	4549232.667
B12	672566.708	4551059.757
B13	673468.135	4555924.335
B14	672291.529	4557740.486
M1	675031.703	4560416.182



(a) Two-layer flow scenario (Test Run A).

(b) ULB scenario (Test Run B).

(c) LLB scenario (Test Run C).

Figure C.1. Station locations for model validating test runs.

C.2. Comparison Plots

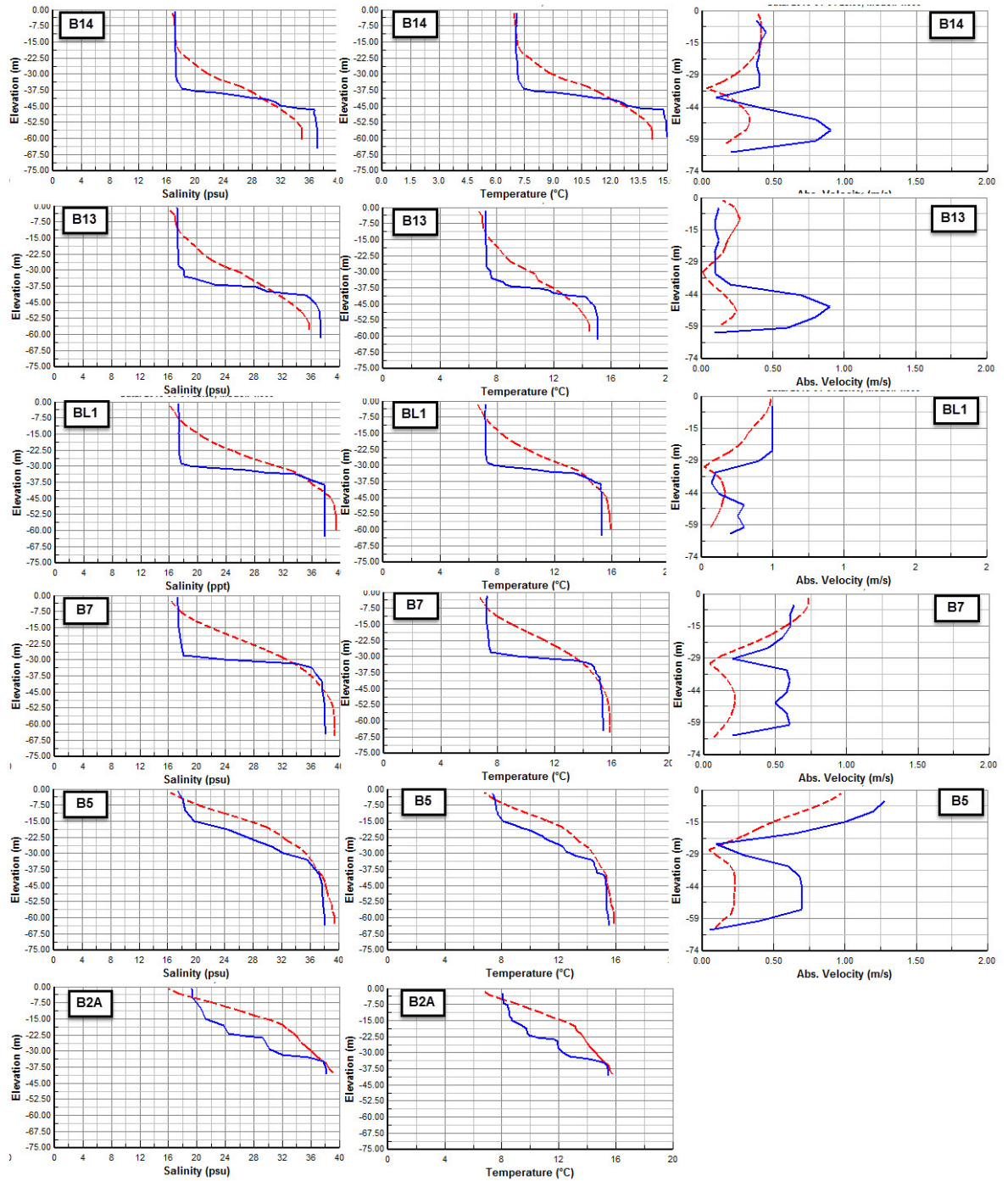


Figure C.2. Additional comparison plots for Test Run A.

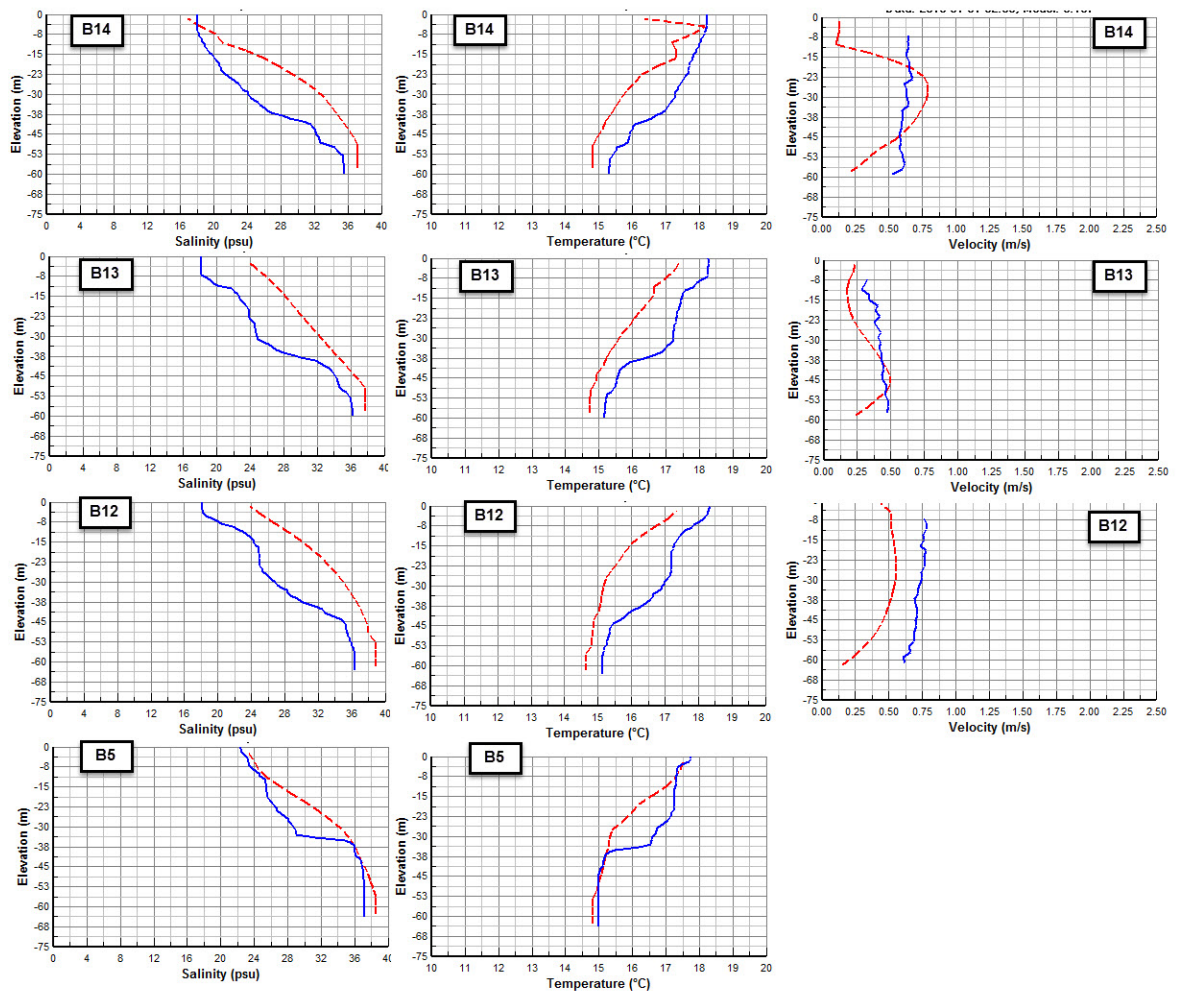


Figure C.3. Additional comparison plots for Test Run B.

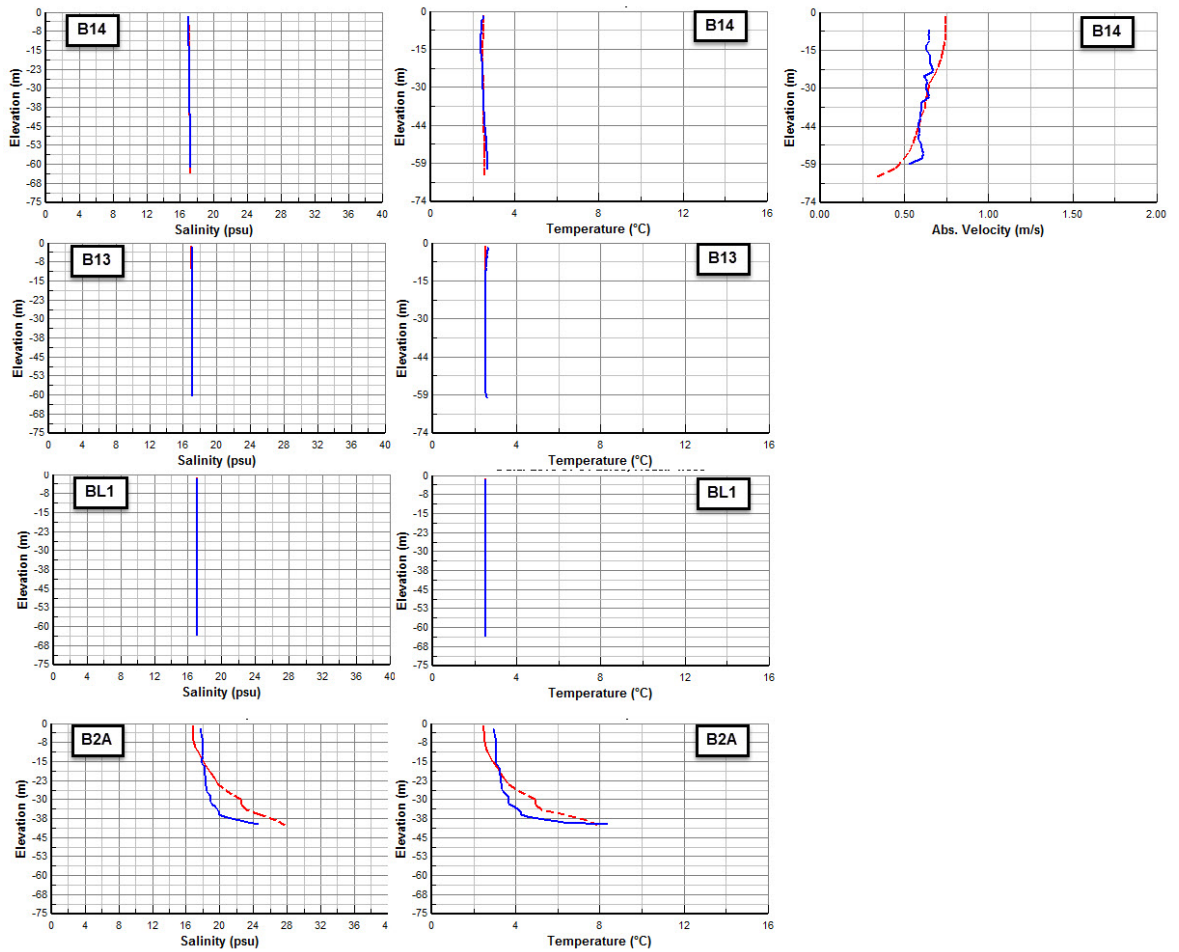
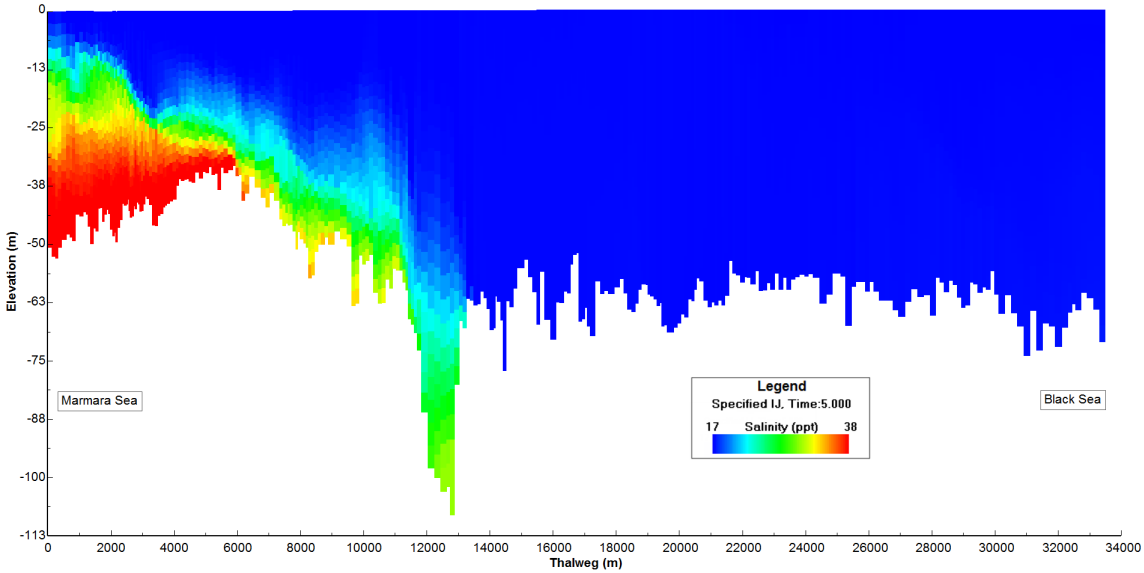
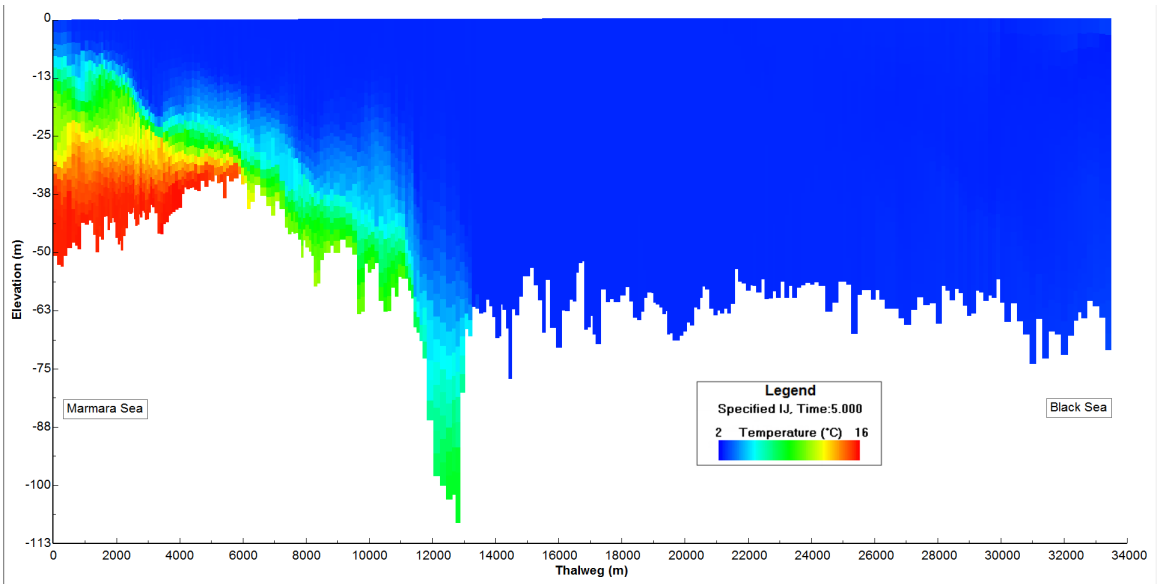


Figure C.4. Additional comparison plots for Test Run C.

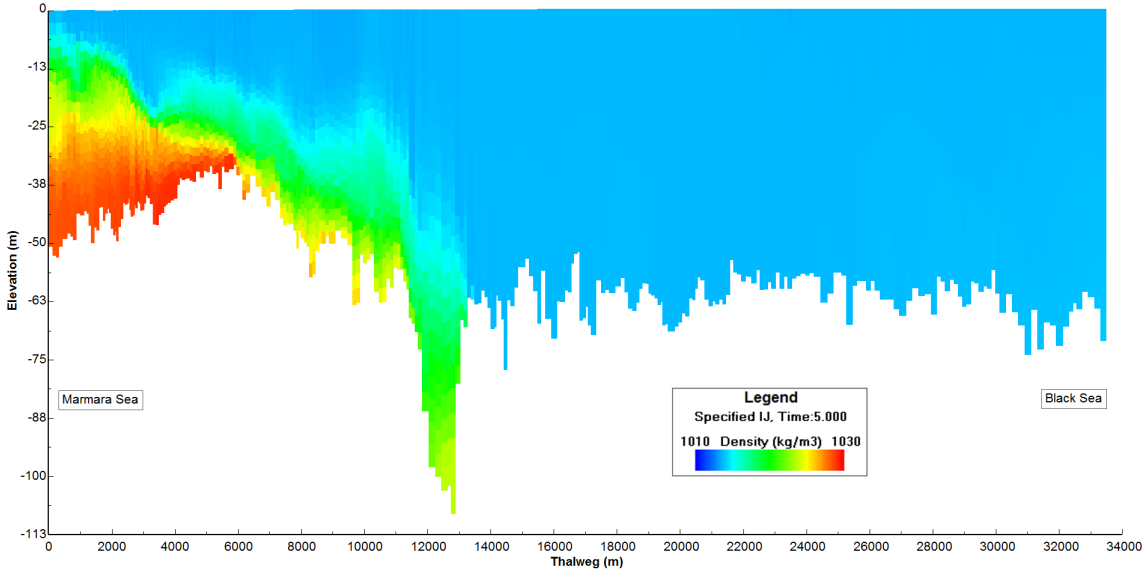
C.3. Salinity, Temperature and Density Plots



(a) Salinity profile.

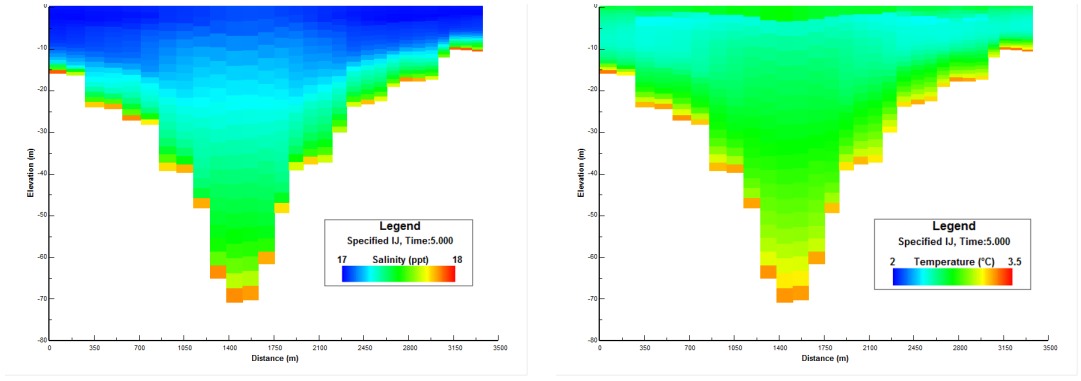


(b) Temperature profile.



(c) Density profile.

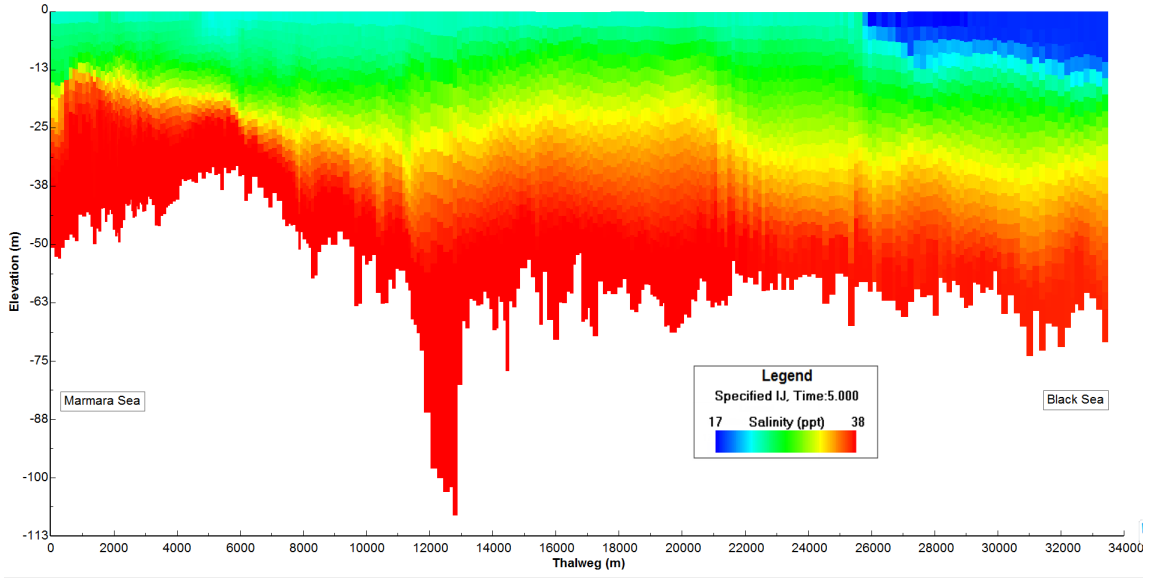
Figure C.5. Thalweg line longitudinal-section profiles for Test Run C.



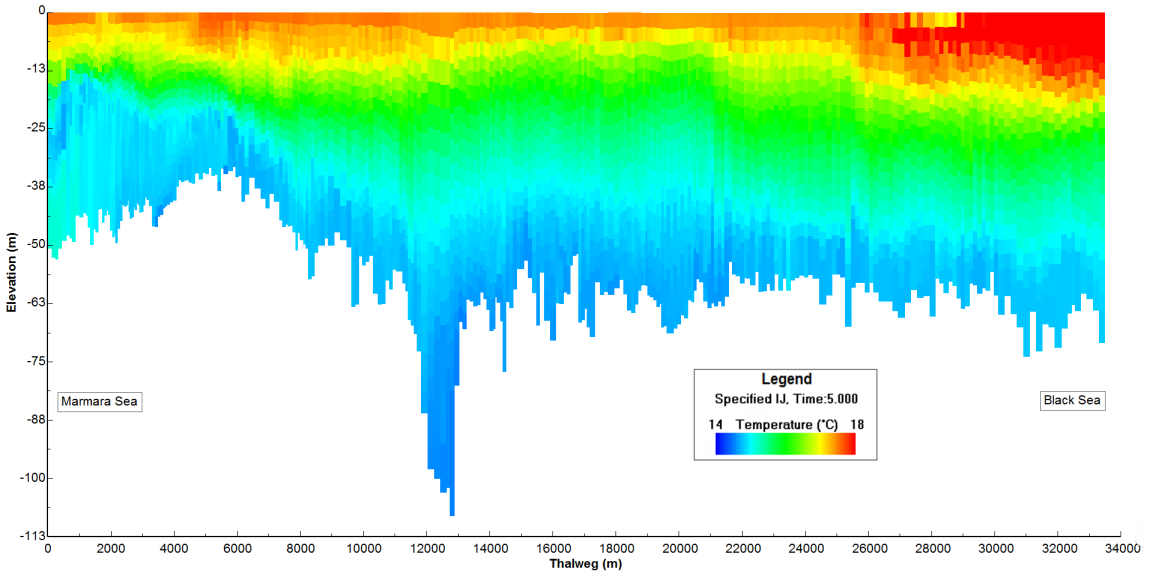
(a) Salinity profile.

(b) Temperature profile.

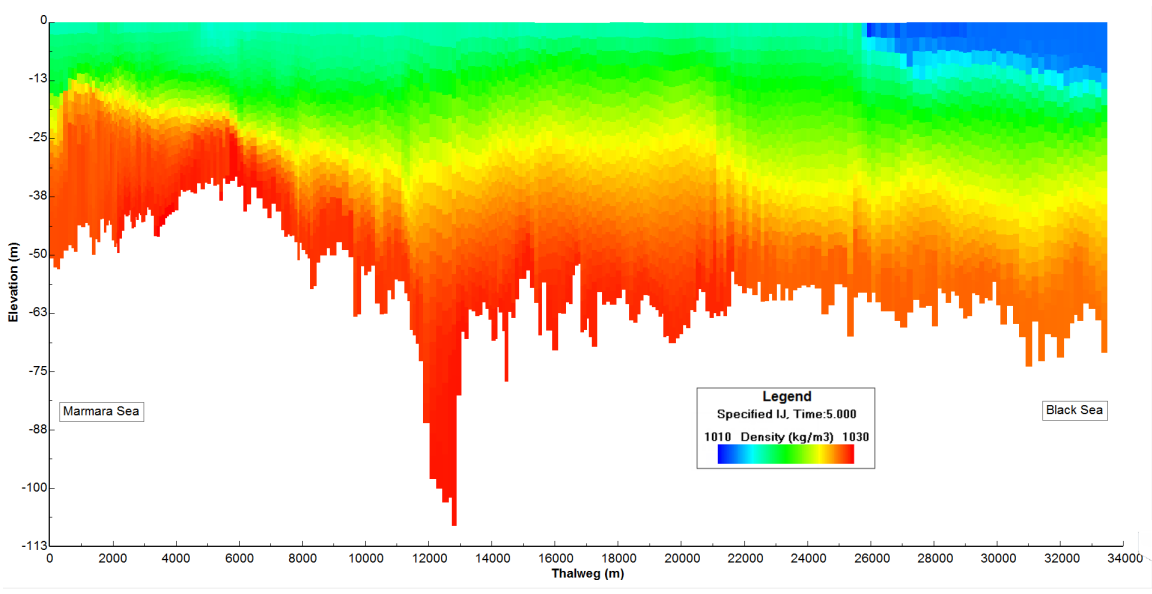
Figure C.6. Inside domain northern cross-sectional salinity and temperature profiles - Test Run C.



(a) Salinity profile.

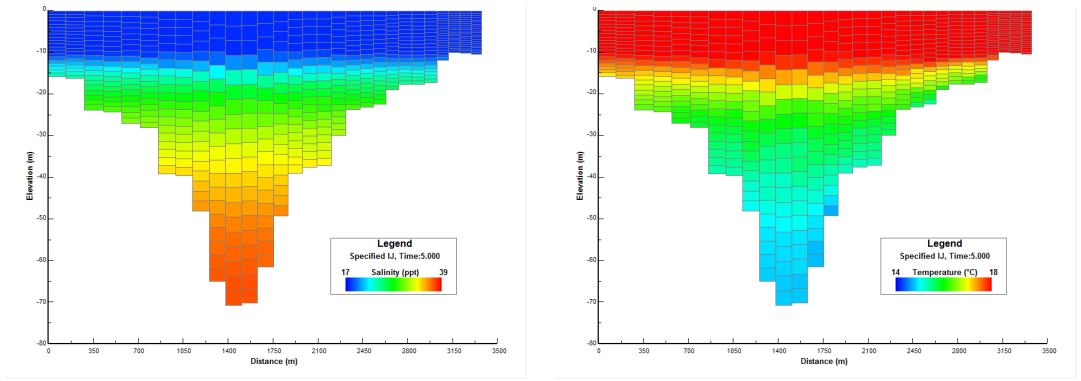


(b) Temperature profile.



(c) Density profile.

Figure C.7. Thalweg line longitudinal-section profiles for Test Run B.

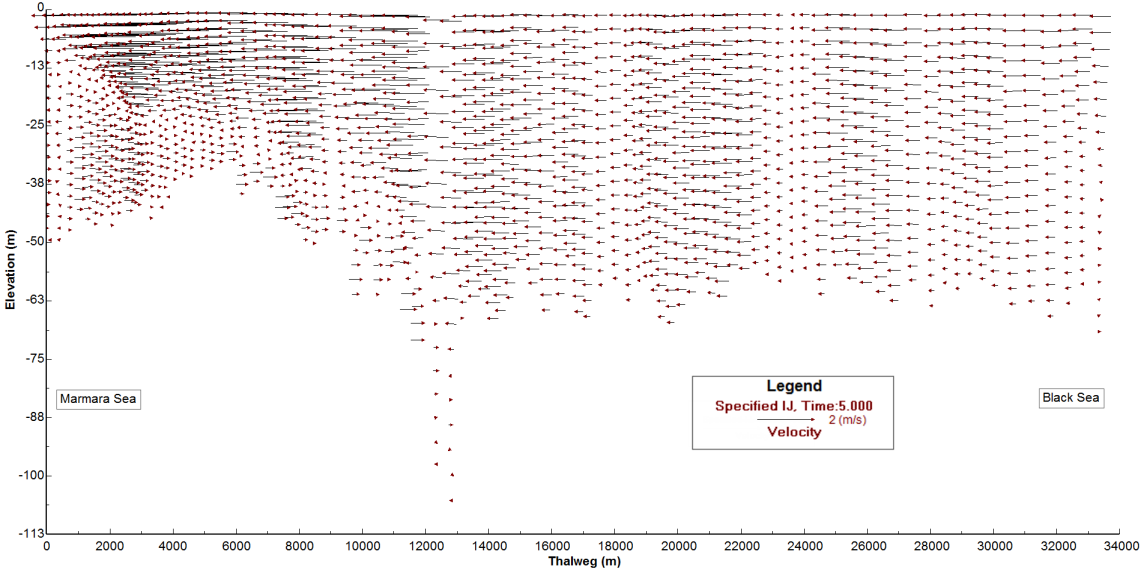


(a) Salinity cross-section.

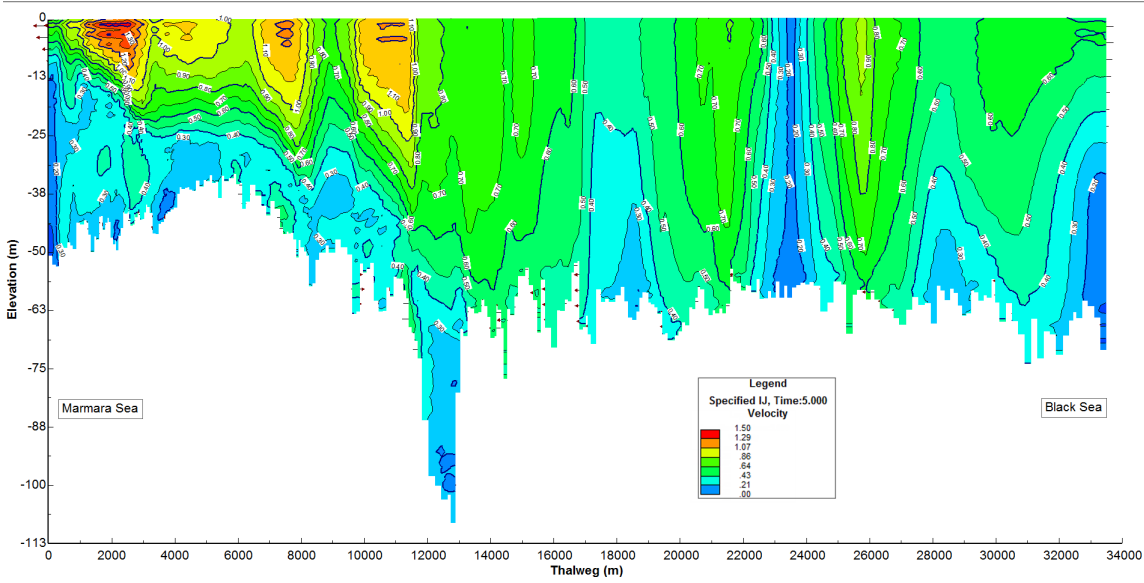
(b) Temperature cross-section.

Figure C.8. Inside domain northern cross-sectional salinity and temperature profiles - Test Run B.

C.4. Velocity Plots

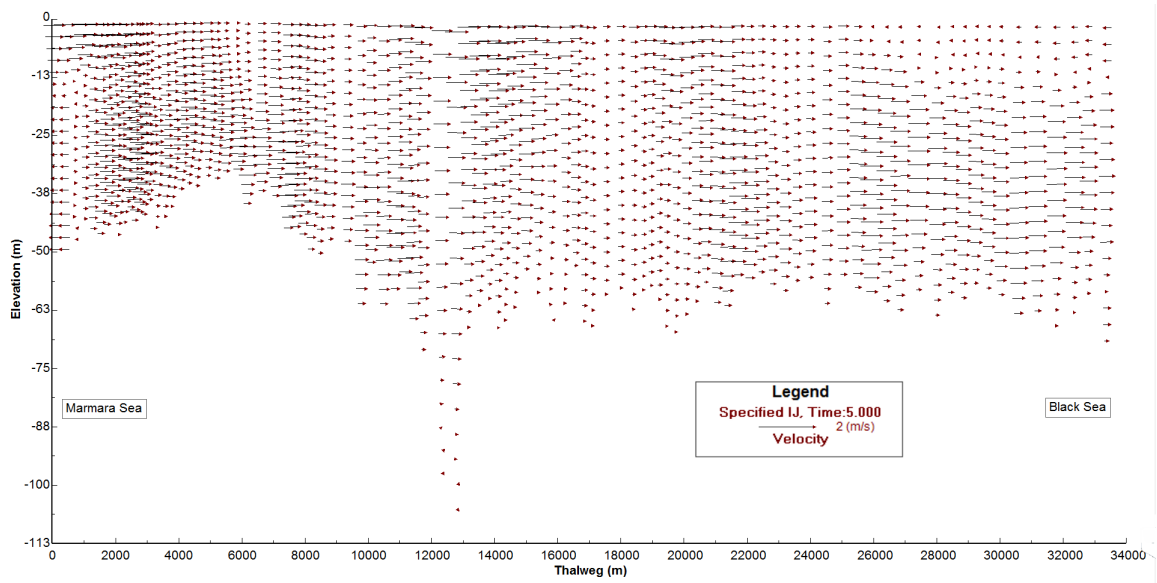


(a) Velocity vectors.

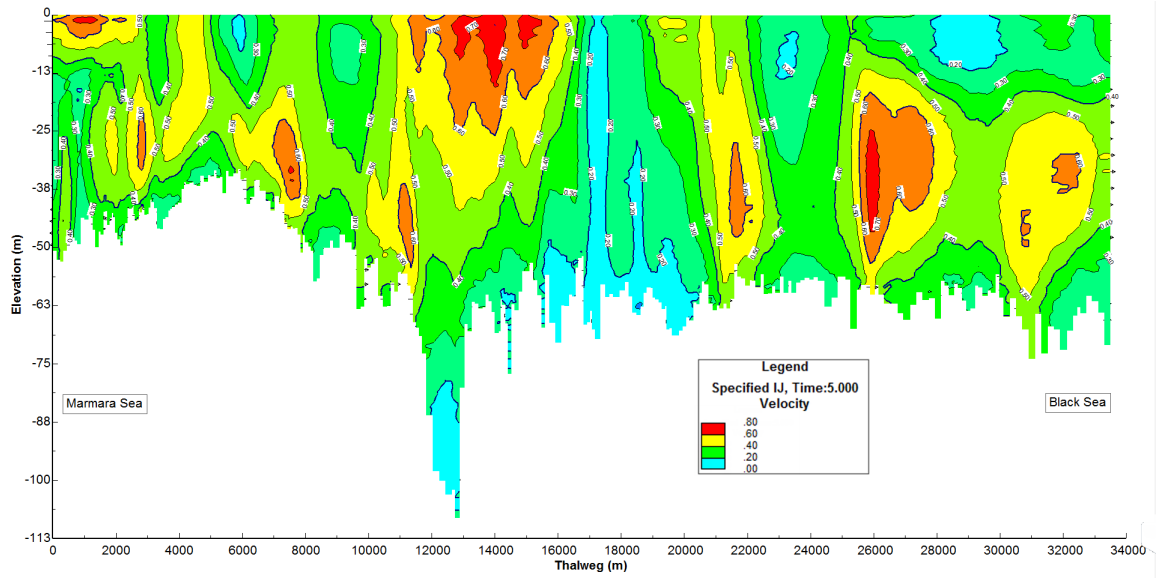


(b) Velocity contour.

Figure C.9. Thalweg line longitudinal-section velocity profiles for Test Run C.



(a) Velocity vectors.



(b) Velocity contour.

Figure C.10. Thalweg line longitudinal-section velocity profiles for Test Run B.

C.5. Bed Shear Stress Plots

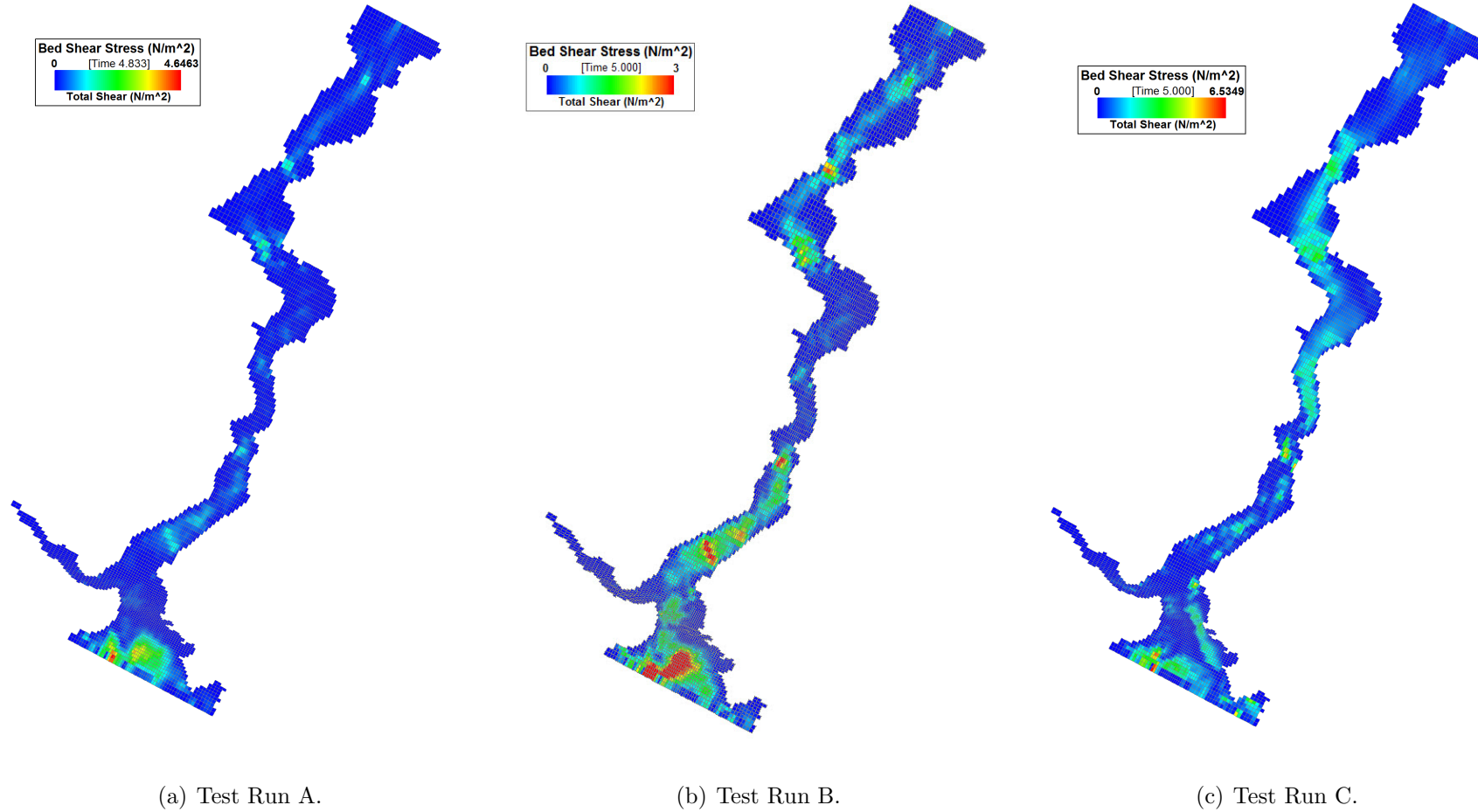


Figure C.11. Bed shear stress distribution over the domain.

C.6. Densimetric Froude Number

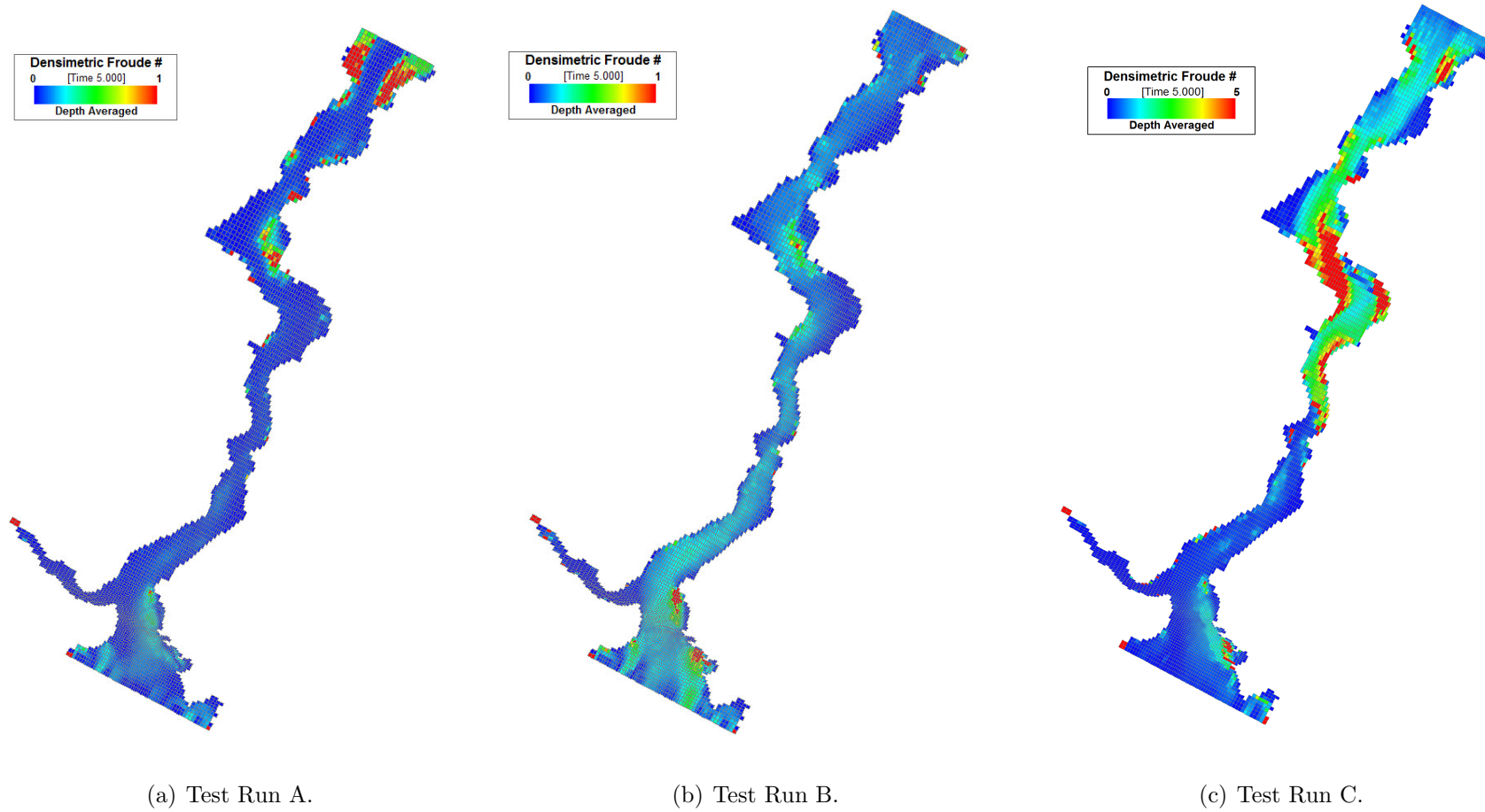
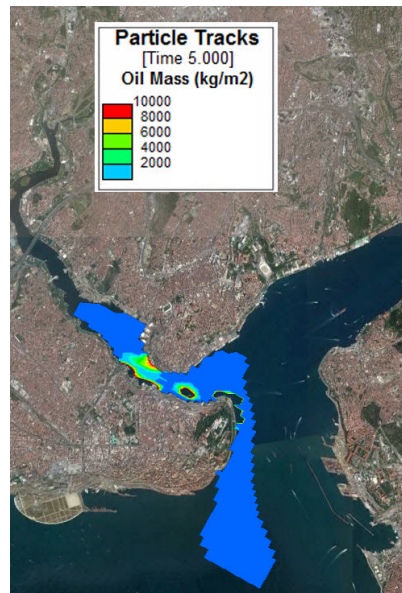


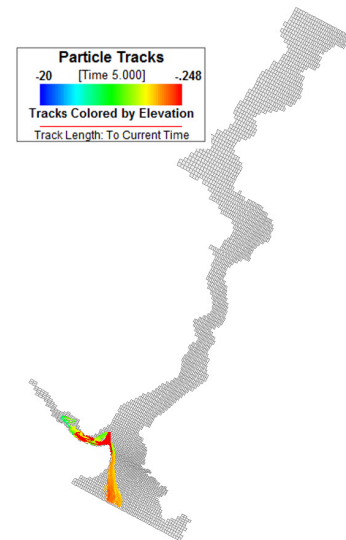
Figure C.12. Densimetric Froude number distribution over the domain.

APPENDIX D: OIL SPILL PLOTS

D.1. Plots of Scenario(I), Test Runs A,D,E,N,Q and Z

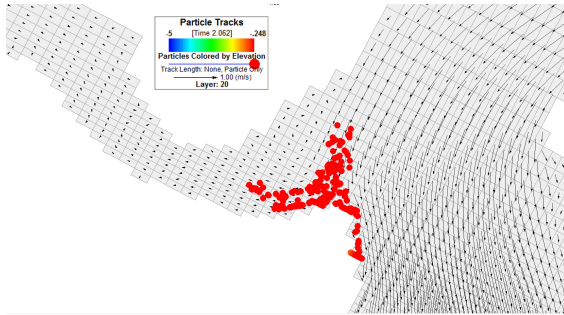


(a) Total concentration during three days, (kg/m^2).

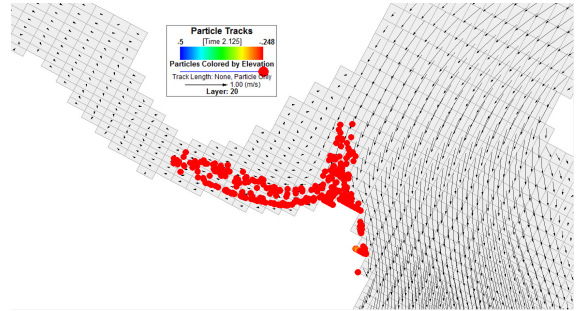


(b) Total contaminated area during three days.

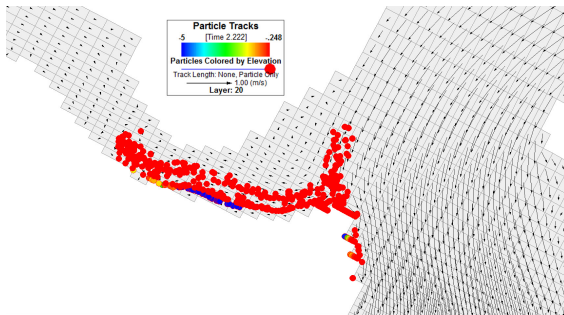
Figure D.1. Fate of SL.2 accident on Scenario(I), Test Run A.



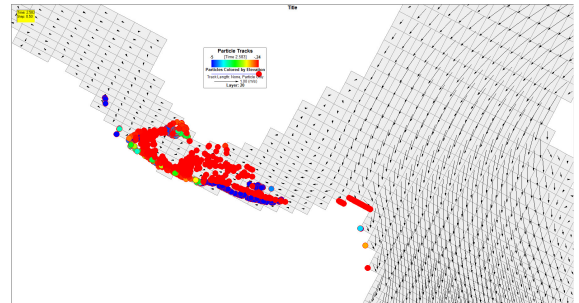
(a) After 1.5 hour.



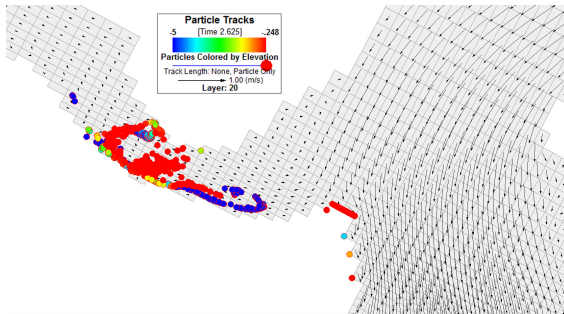
(b) After 3 hours.



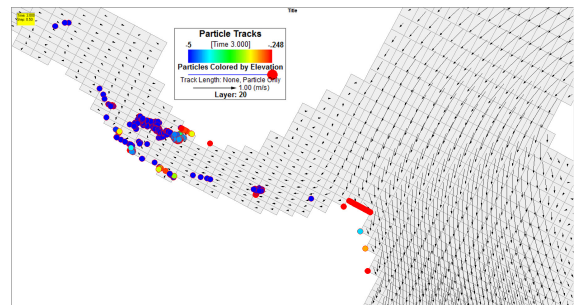
(c) After 5.5 hours.



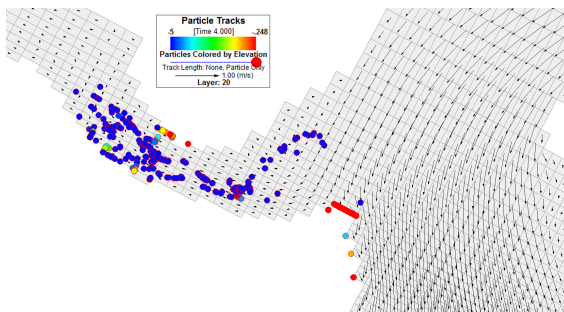
(d) After 14 hours.



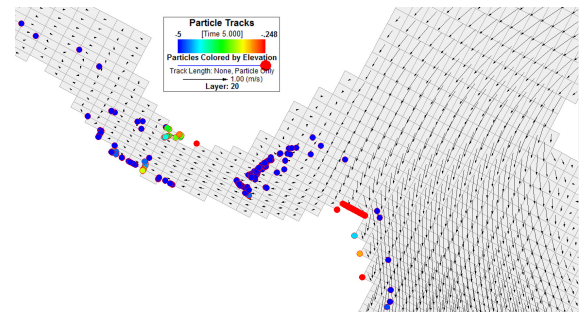
(e) After 15 hours.



(f) After 24 hours.



(g) After 48 hours.



(h) After 72 hours.

Figure D.2. Particles location of SL.2 accident on Scenario(I), Test Run A.



(a) After 1 hour.



(b) After 3 hours.



(c) After 5.5 hours



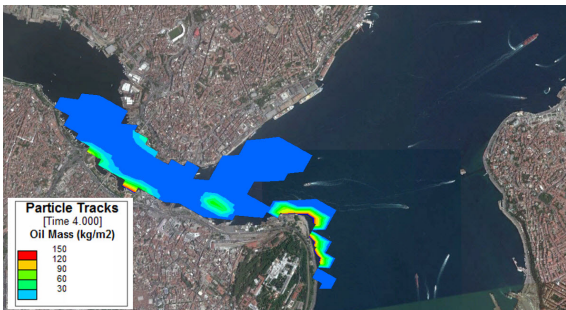
(d) After 14 hours.



(e) After 15 hours.



(f) After 24 hours



(g) After 48 hours.



(h) After 72 hours.

Figure D.3. Concentration(kg/m^2) of SL.2 accident on Scenario(I), Test Run A.

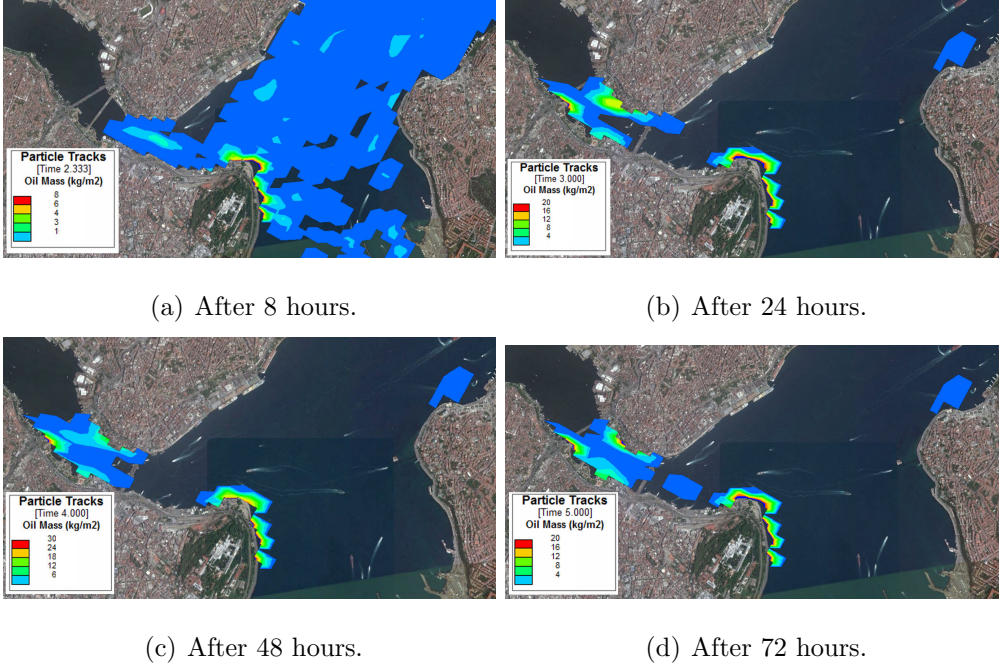


Figure D.4. Concentration(kg/m^2) of SL.1 accident on Scenario(I), Test Run D.

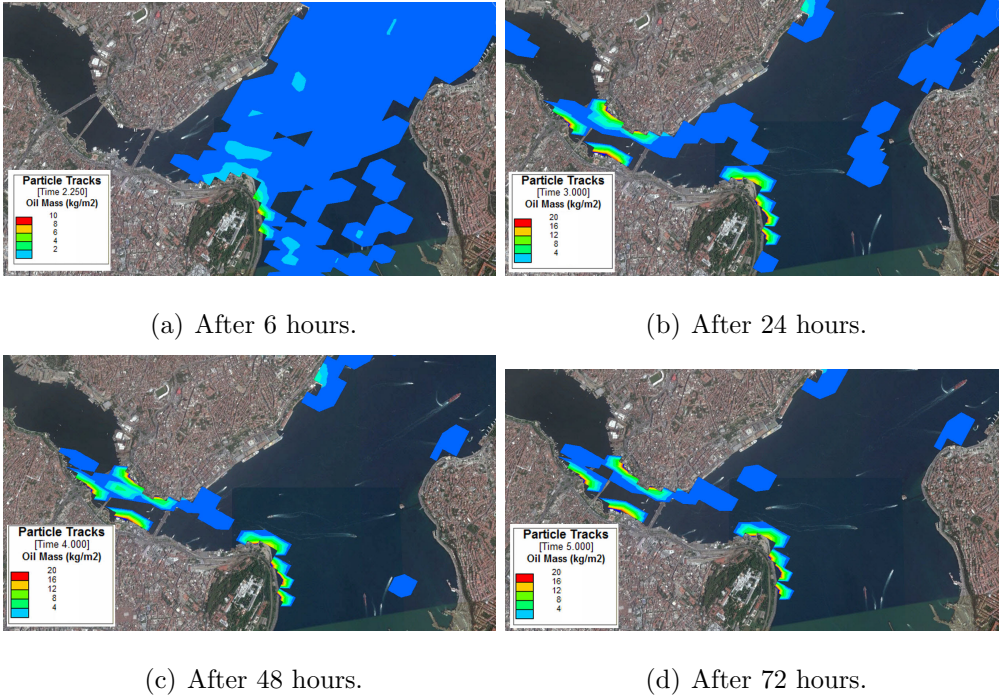


Figure D.5. Concentration(kg/m^2) of SL.1 accident on Scenario(I), Test Run E.

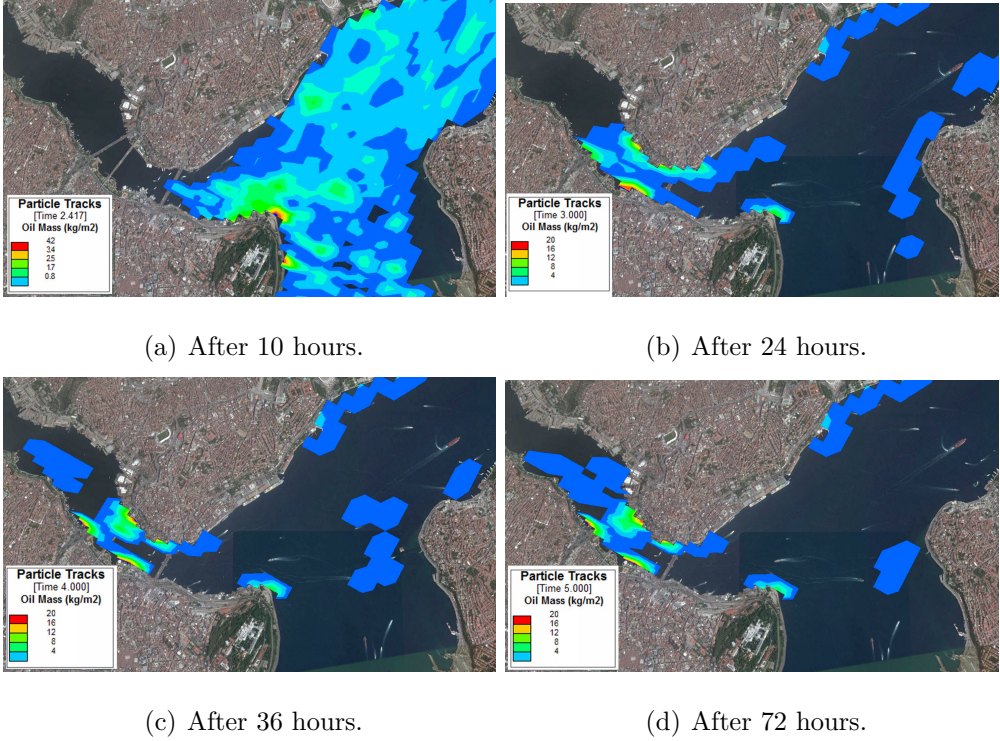


Figure D.6. Concentration(kg/m^2) of SL.1 accident on Scenario(I), Test Run N.

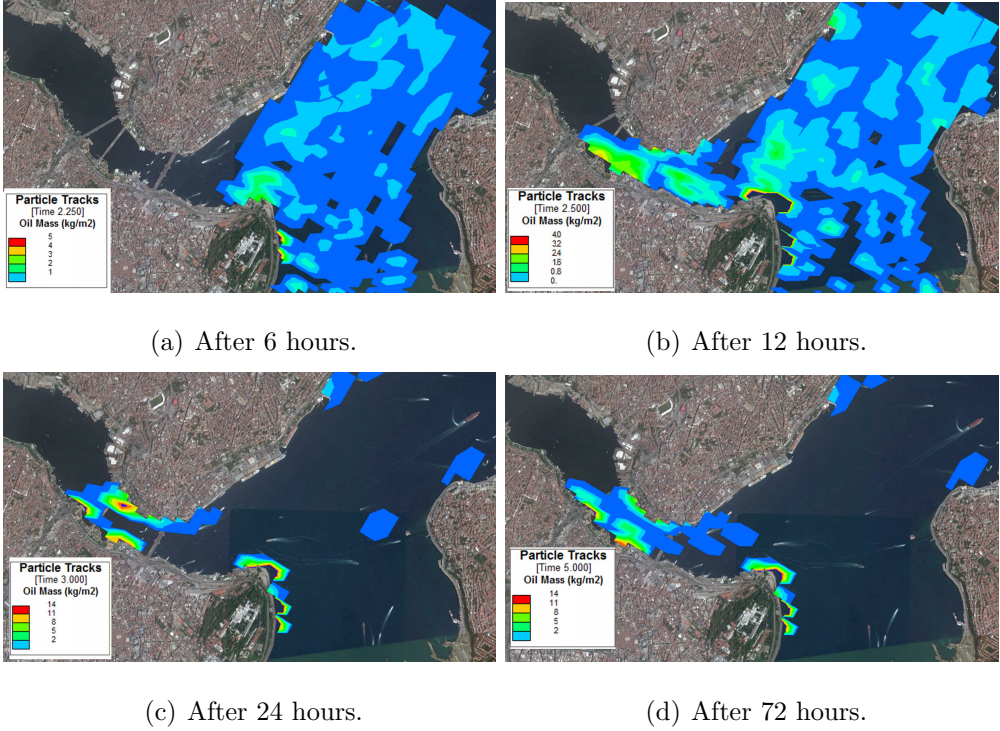


Figure D.7. Concentration(kg/m^2) of SL.1 accident on Scenario(I), Test Run Q.

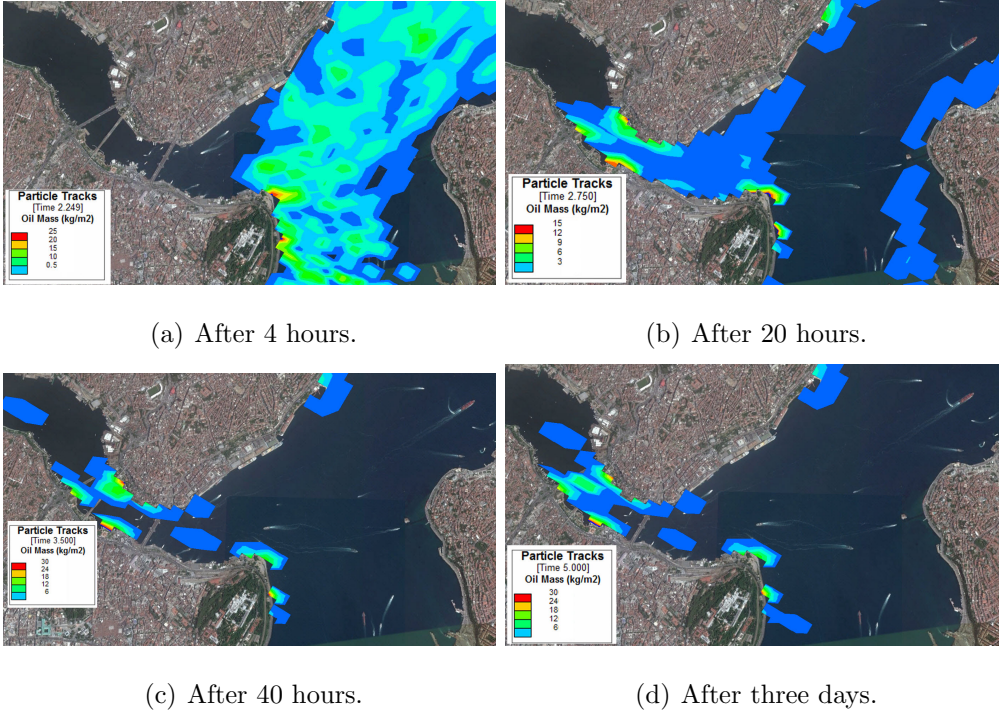


Figure D.8. Concentration(kg/m^2) of SL.1 accident on Scenario(I), Test Run Z.

D.2. Plots of Scenario(II), Test Runs C, R and K

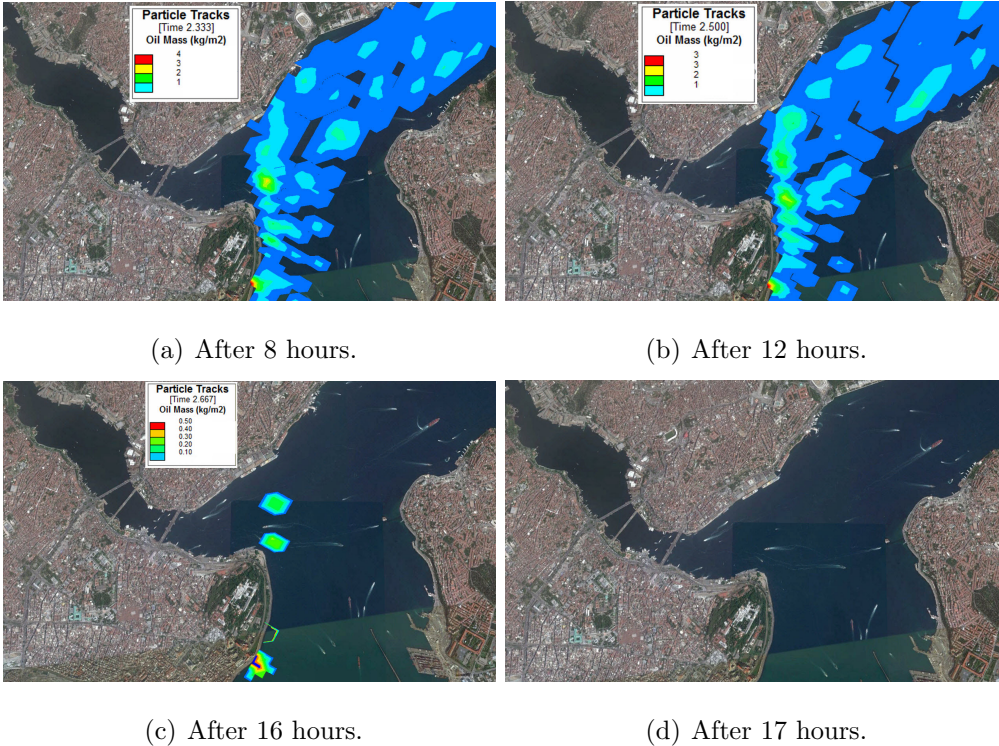


Figure D.9. Concentration(kg/m^2) of SL.1 accident on Scenario(II), Test Run C.

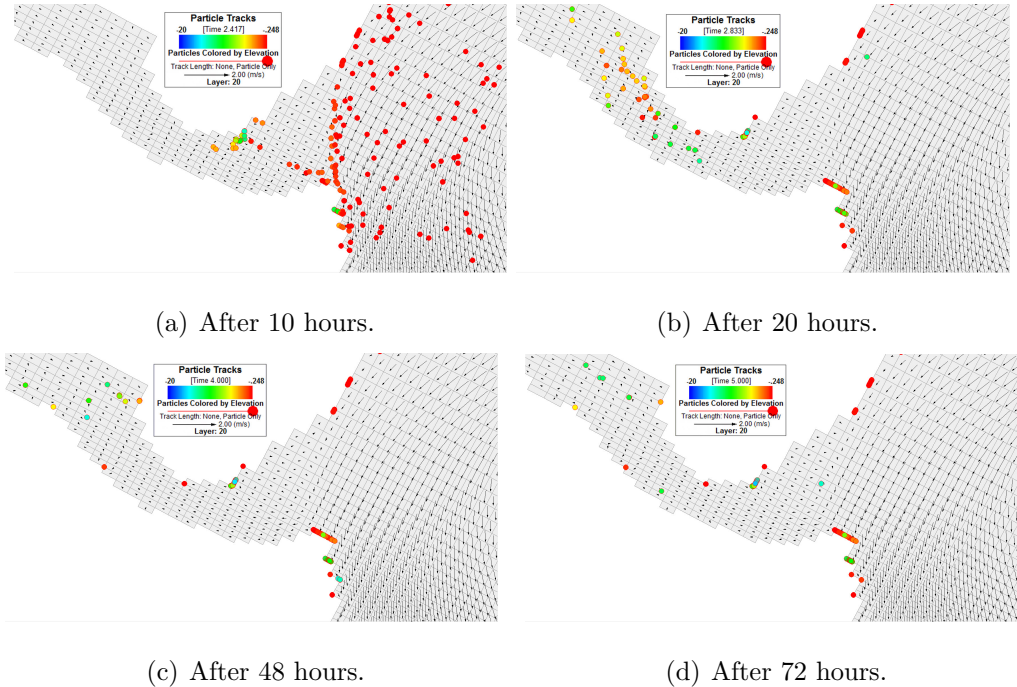


Figure D.10. Particles location of SL.1 accident on Scenario(II), Test Run K.

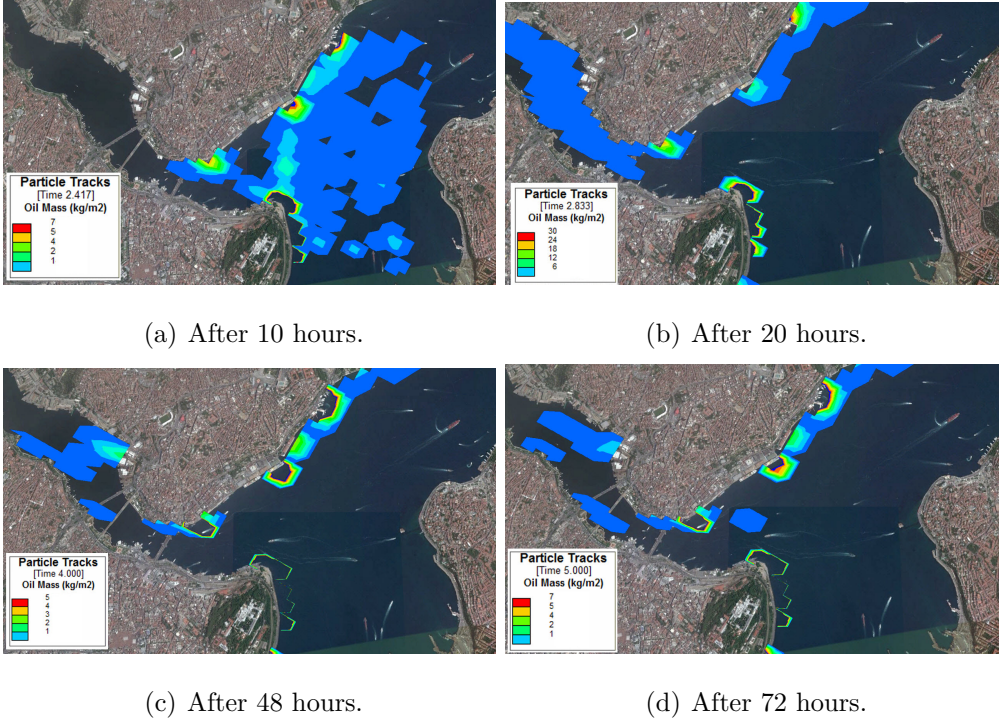


Figure D.11. Concentration(kg/m^2) of SL.1 accident on Scenario(II), Test Run K.

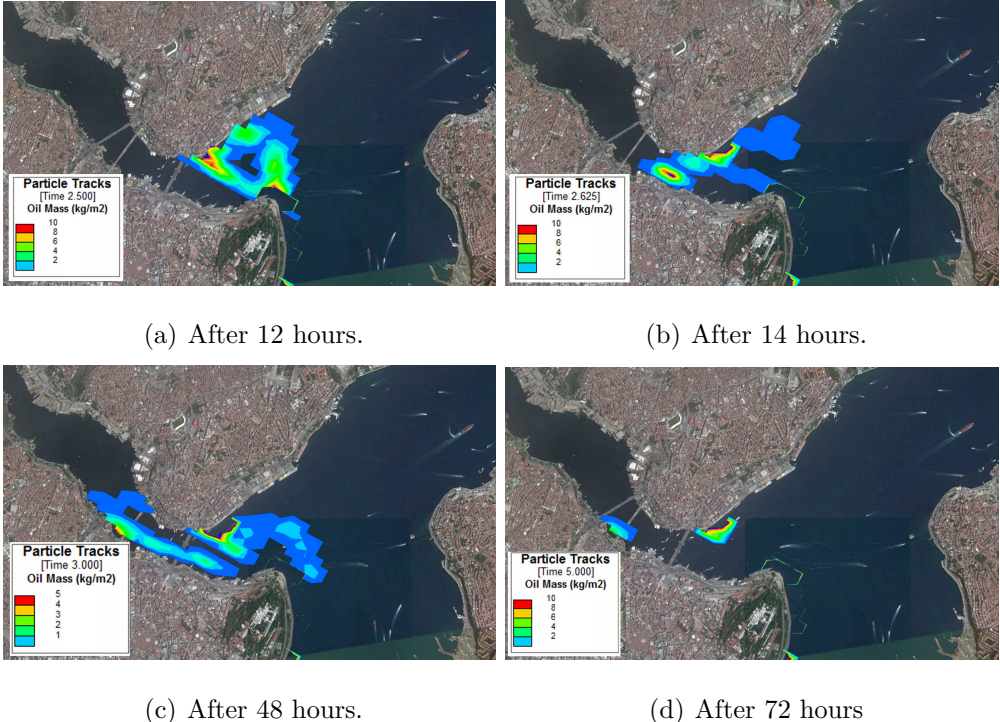


Figure D.12. Concentration(kg/m^2) of SL.2 accident on Scenario(II), Test Run K.

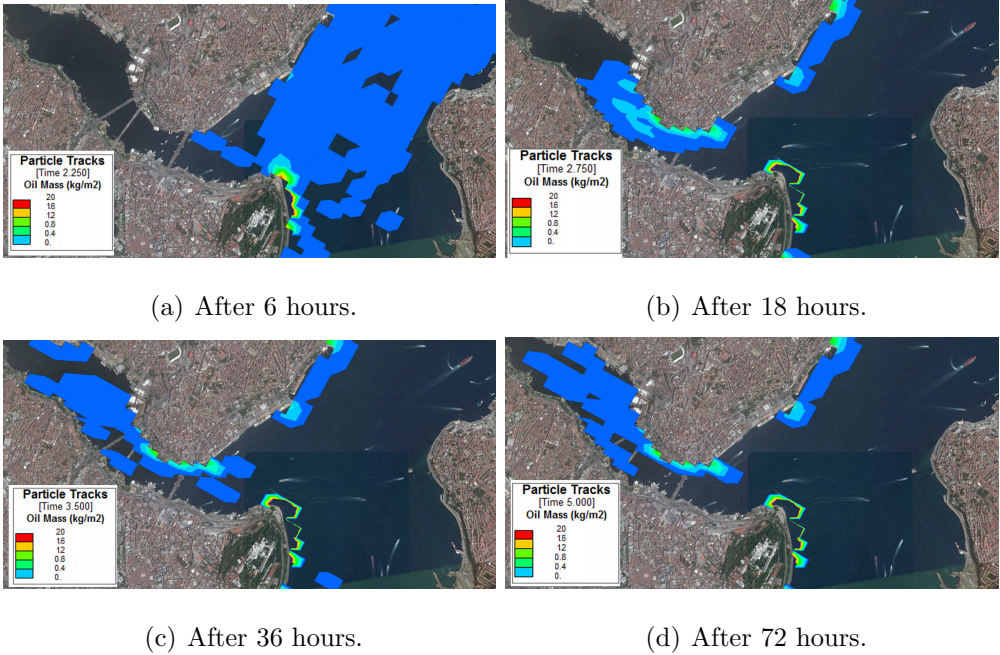


Figure D.13. Concentration(kg/m^2) of SL.1 accident on Scenario(II), Test Run R.

D.3. Plots of Scenario(IV), Test Runs B and M

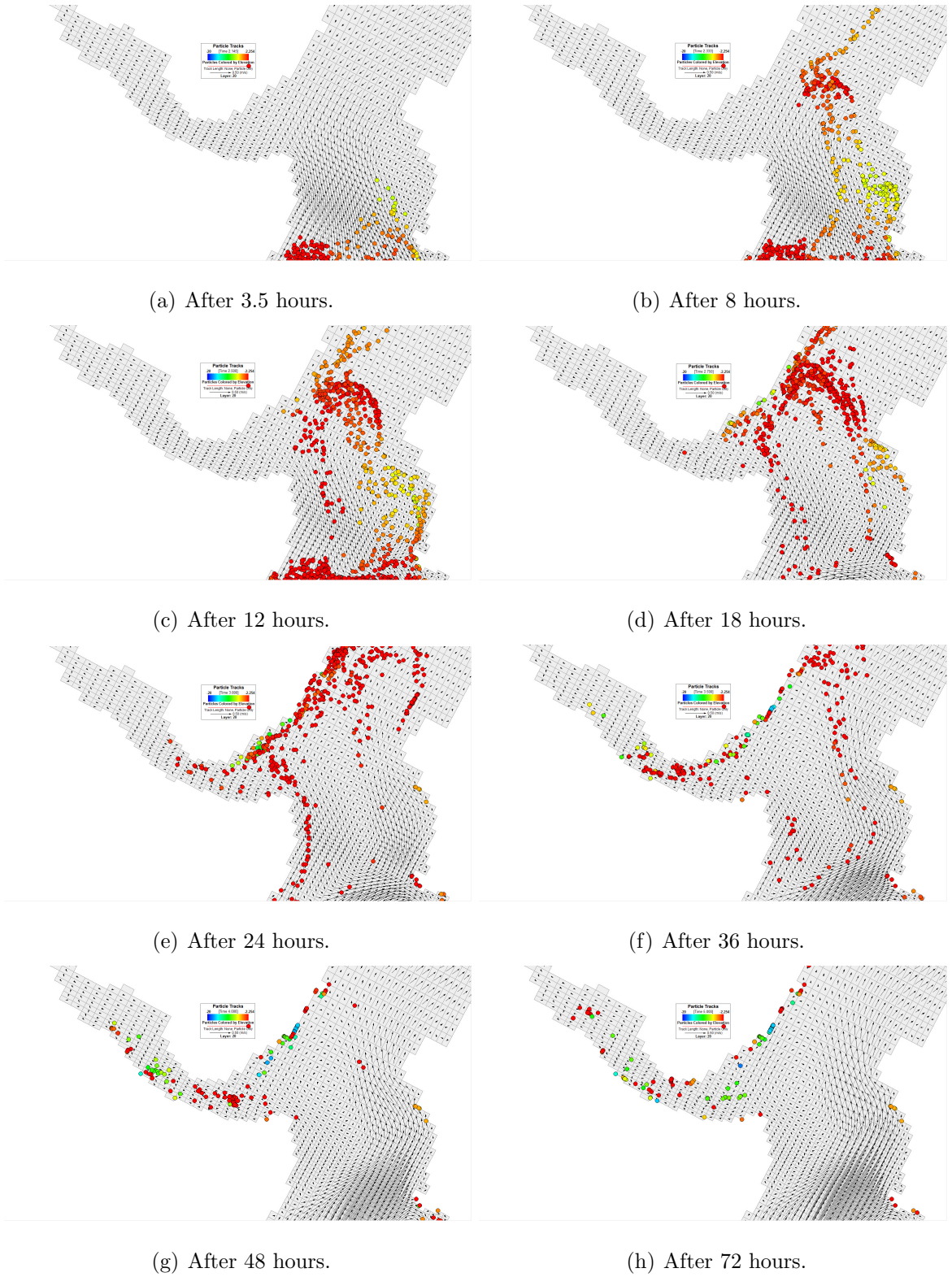


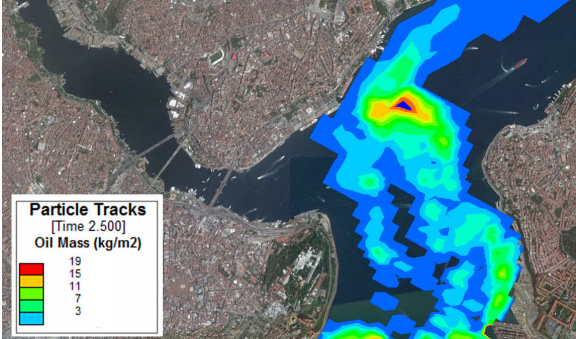
Figure D.14. Particles location of SL.3 accident on Scenario(V), Test Run M.



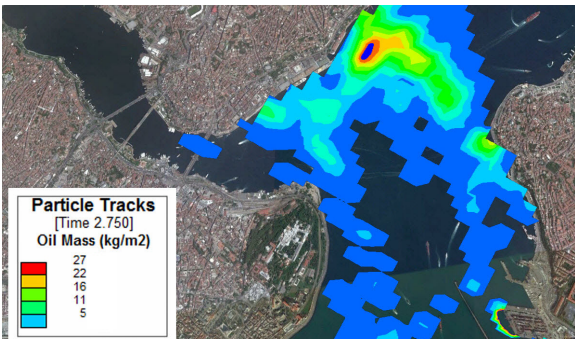
(a) After 3.5 hours.



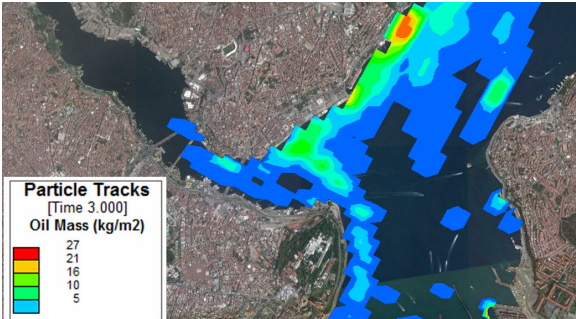
(b) After 8 hours.



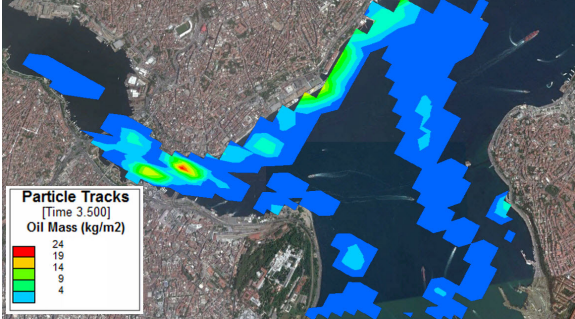
(c) After 12 hours.



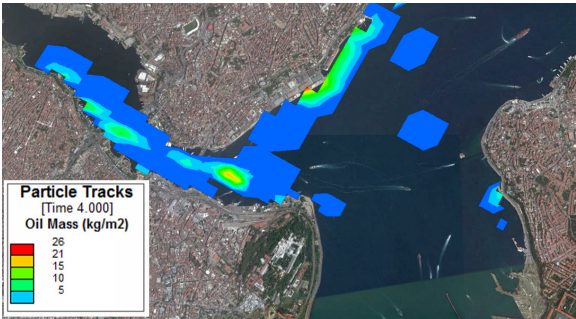
(d) After 18 hours.



(e) After 24 hours.



(f) After 36 hours.



(g) After 48 hours.



(h) After 72 hours.

Figure D.15. Concentration(kg/m^2) of SL.3 accident on Scenario(IV), Test Run M.

D.4. Plots of Scenario(V), Test Runs

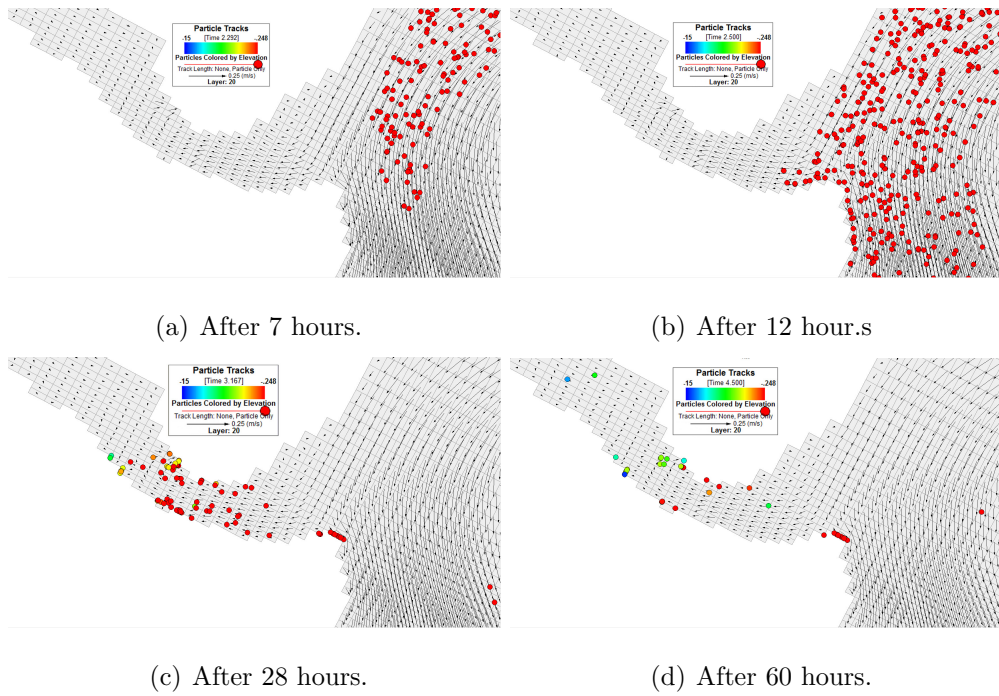


Figure D.16. Particles location of SL.1 accident on Scenario(V), Test Run H.

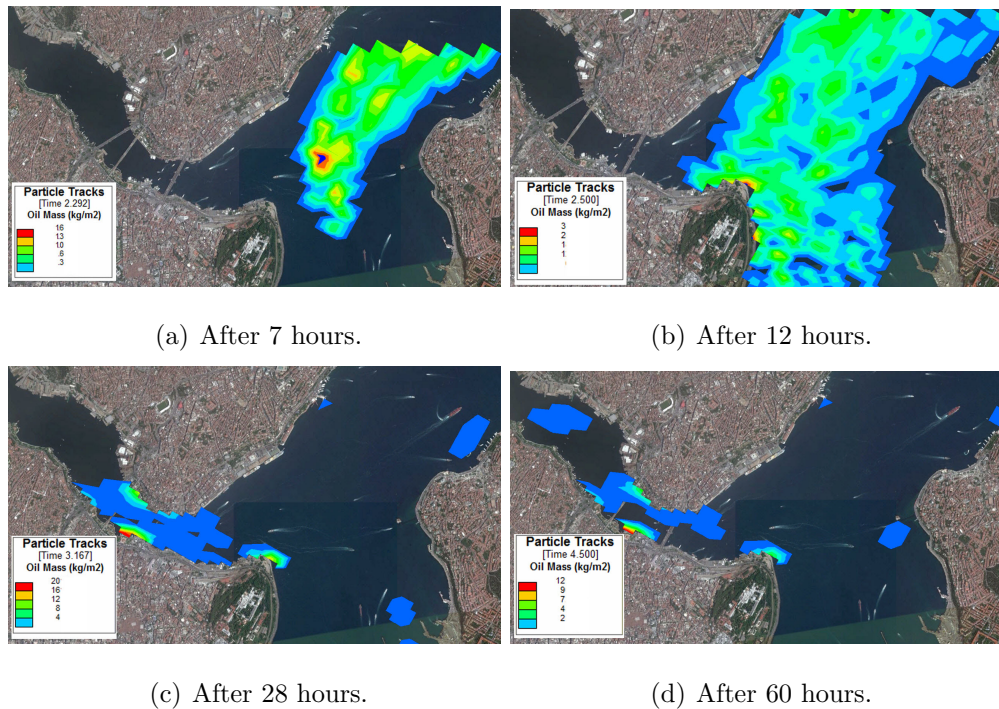
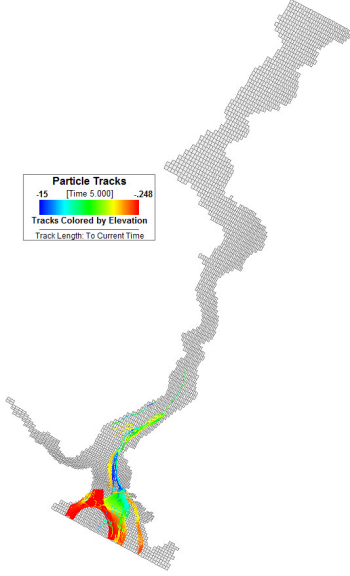


Figure D.17. Concentration(kg/m^2) of SL.1 accident on Scenario(V), Test Run H.

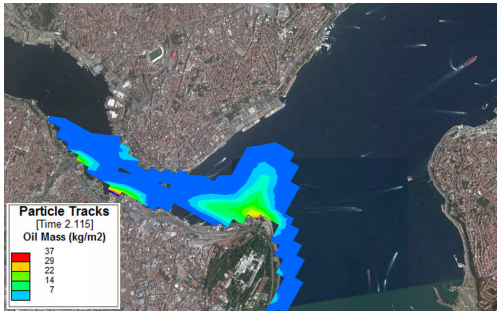


(a) Total concentration of SL.2 during three days, (kg/m^2).



(b) Total contaminated area of SL.3 during three days.

Figure D.18. Fate of SL.2 and SL.3 accident on Scenario(V), Test Run H.



(a) After 3 hours.



(b) After 24 hours.



(c) After 36 hours.



(d) After 72 hours.

Figure D.19. Concentration(kg/m^2) of SL.2 accident on Scenario(V), Test Run H.